Effective Interactions and Phase Behavior
of Colloidal Dispersions

Effective Interactions and Phase Behavior

of Colloidal Dispersions

A thesis submitted to
the University of Insubria
in partial fulfillment of the requirements
for the degree of Doctor of Philosophy

by

Jader Colombo

Supervisor: Alberto Parola
Full Professor of Physics
Department of Physics and Mathematics
University of Insubria

January 2011

I know this defies the Law of Gravity,
but, you see, I never studied law!

Bugs Bunny,
High Diving Hare (1949)

Contents

1

Introduction

I NTRODUCTIONS to books are often boring; introductions to scientific texts are invariably so, with a few notable exceptions – and the present case is *not* one of them. But, alas, they are still quite useful. So be warned and keep reading: at least, every effort has been made for it to be short.

This thesis deals with a number of selected questions concerning the equilibrium properties and the phase behavior of colloidal dispersions, using both theory – including analytical and numerical methods from the physics of the liquid state – and computer simulation. The point of view adopted is the one of a theoretical physicist, thereby several low-level details have been neglected in favor of general and (whenever possible) simple models. As a consequence, an emphasis is placed on the notion of effective interaction in a complex fluid, which permeates or underlies most of the work here reported.

Colloidal dispersions, or simply colloids, are a kind of "ultra divided matter" (quoting the Nobel prize winner Pierre-Gilles de Gennes [33]) which has gained a broad scientific and industrial interest in the last few decades. The birth of colloid science dates back to the second half of the nineteenth century and is generally associated with the name of the Scottish chemist Thomas Graham. Graham, performing some dirty-hand experiments like most great scientists of that time, noticed that some substances (e.g. sugar and simple salts) diffused quite quickly through parchments or animal membranes, and formed crystals when dried; other substances (e.g. gum arabic, albumen), on the contrary, diffused rather slowly and did not form crystals when dried. He termed the former class of substances *crystalloids*, the latter *colloids* (which, after the Greek word for glue – κόλλα – means "sticky stuff") [53]. In the attempt to separate the two classes, he also laid the foundations of the process of dialysis.

Later on Graham's classification based on the formation of crystals turned out to be inconsistent and was dropped; the term colloid, nevertheless, managed to survive and, contrary to its etymology, ended up to include substances that are not sticky at all according to common experience. In the modern vocabulary, colloid designates a system in which finely divided particles, which are approximately 1 to 1000 nanometers in size, are dispersed within a continuous medium in a manner that prevents their coagulation or rapid settling. The aforementioned range of dimensions, which serves merely as a crude indication, makes the dispersed particles quite big if compared to the size of the atoms or molecules making up the dispersing medium but, at the same time, assures that they are small enough to undergo Brownian motion [93] as a consequence of the thermal agitation of the medium itself.* Both the dispersed particles

---

*If this were not the case, colloids would rather look like a bunch of stones thrown in a bowl of water – not so interesting to be studied.

and the dispersing medium may be solid, liquid or gas; this thesis will mainly deal with dispersions of solid particles in a liquid medium, which are properly termed *sols*.

Why all this fuzz about colloids? One sometimes encounters in the literature or in textbooks the claim that colloids permeate almost every aspect of life; although it might be the case, like most hyperboles it should be taken with care: after all, we do not live in a colloidal world – solids, fluids and gases are still the most abundant forms of matter on the planet. Nevertheless, it is indubitable that many substances of daily use fall in the category. If you ever drinked a glass of milk, then you had the chance to appreciate the taste of a colloidal dispersion (more precisely, an *emulsion*) of butterfat globules within a water-based liquid. You certainly recall with pleasure (or maybe not, depending on your attitude in taking a bath) having played as a child with a dispersion of air bubbles in water – a *foam*.[†] And if you happened to live in Cape Race, Newfoundland (Canada), one of the foggiest places in the world with an average of over one hundred and fifty foggy days per year [73], you surely would know much about dispersions of water droplets and ice crystals suspended in the air. These were just but a few prototypes; shaving cream, mayonnaise, jelly, smoke, ink and paint are other familiar examples of colloidal dispersions [64].

If you still cannot decide whether colloid science is worth studying (and funding), the following excerpt from a 1921 book [8] should dissipate any residual doubt:

> *At first sight colloid chemistry may not seem to be an important branch of chemistry, either theoretically or technically; but this opinion changes when we consider that a knowledge of colloid chemistry is essential to anybody who really wishes to understand about: cement, bricks, pottery, porcelain, glass, enamels; oils, greases, soaps, candles; glue, starch and adhesives; paint, varnishes, lacquers; rubber, celluloid and other plastics; leather, paper, textiles; filaments, casts, pencils and crayons; inks; roads, foundry cores, coke, asphalt; graphites, patines; zinc, phosphorus, sodium and aluminium; contact sulphuric acid, hardened oils, etc; beer, ale and wine; cream, butter, cheese and casein products; cooking, washing, dyeing, printing; ore flotation, water purification, sewage disposal; smoke prevention; photography; wireless telegraphy, illuminants; comets; pharmacy; physiology. In other words, colloid chemistry is the chemistry of every-day life.*

Feel free to substitute colloid science for colloid chemistry (the author was of course a chemist); although it might appear somewhat extreme, the previous statement surely leaves an impression. Almost a century has passed since that book was first published and it is indisputable that colloid science still plays a major role in the paint, food, cosmetic, pharmaceutical and agricultural industry [129].

Another field where colloid science finds a fertile ground is biology, especially in a number of sub-fields ranging from biochemistry to biophysics and biotechnology [15, 42]. It would be impossible to give here a comprehensive list of applications; suffice it to say that concepts such as the colloid osmotic pressure of blood exist [19, 76] and that many scientists around the world struggle daily to understand how to make crystals suitable for X-ray diffraction out of colloidal protein solutions [40, 116].

[†]If you prefer a tastier example, take the cream out of the aforementioned glass of milk and whip it in a mixer.

COLLOIDS AND PHYSICS

Despite the wide range of applications just highlighted, this would not be the thesis of a physicist if colloids did not have some intrinsic interest for the physical sciences themselves, and indeed they do: colloidal dispersions have frequently proved a valuable playground for testing ideas in thermodynamics, condensed matter and statistical physics. After all, they provided one of the greatest insights ever in the modern theory of matter, whose atomic nature gained widespread consensus only after the works of Einstein and Perrin on Brownian motion were published [58]. Nowadays, colloids are exploited both as magnified models of traditional atomic and molecular systems and as building blocks for genuinely novel materials.

In the former context, they respond to a very frustrating feeling anyone with an interest in condensed matter sooner or later experiences: we know a lot about atoms and their properties, we might even be capable of extraordinarily precise predictions about their behavior – but we cannot *see* them.[‡] On the contrary, most colloids have dimensions that easily fall in the range of operation of a common optical microscope; by exploiting the confocal setup one can even track single particles in three-dimensional space with high precision over large time scales [109]. Luckily colloids can be made to interact just as atoms or molecules do – of course you have to neglect any quantum effect, since their size firmly roots them in the classical world, and allow for much slower dynamics. Thus, a colloidal system can be found in all the traditional phases of atomic matter, or better still, their blown-up, slowed-down, easily observable counterparts [55]. A remarkable difference separates colloids from atomic or molecular substances: the yield stress of the former (when they have one) is appreciably smaller. Consequently, they are easily deformed by applied forces or external fields: not surprisingly, they belong to the broad class of systems known collectively as *soft matter*.[§]

Atoms and molecules, after a while, can become rather dull objects to play with: their interaction was fixed by mother nature a long time ago and we have but to live with it. Colloidal dispersions, on the contrary, offer an unprecedented freedom: a plethora of techniques for tuning the interaction amongst their constituents is at our disposal so that it can vary, just to name a few, from hard-sphere-like to long-range repulsive to short-range attractive [18, 81]. As the interaction departs from the one typical of atomic and molecular systems, novel features appear in the properties of the material; what is more, one might even think about engineering a suitable interaction so that a wished for property arises. Owing to this freedom, the equilibrium phase diagram of a colloidal material can be very different and far richer if compared with the one of a simple atomic system. For example, a short-range attraction destabilizes the liquid phase and instead promotes an isostructural solid-solid transition [79, 56, 22]; competition between attraction and repulsion may result in the formation of cluster fluids and microphases [3, 124, 85]; anisotropic and likely complex interactions can promote – among others – lamellar, columnar, smectic and nematic phases [1, 134, 67].

Non-equilibrium and flow properties of colloidal dispersions (a lengthy discussion of which would enter us into the perilous realms of viscoelasticity and rheology) can be singular and of great practical interest as well, as you might happen to know if you ever

---

[‡]Some experienced reader may object that modern microscopy techniques such as atomic force microscopy and scanning tunneling microscopy do possess sub-nanometer resolution capable of imaging single atoms; that is true, but here seeing designates the natural process involving light impinging on your eye.

[§]Other substances belonging to to the same class include polymers, surfactants, liquid crystals and granular materials.

poured corn starch in a bowl full of water [43] or played with Silly Putty™.¶ Last but not least, since colloidal particles have dimensions comparable to the wavelength of visible light, they serve as building blocks for materials with unique optical properties such as photonic crystals [141, 135].

INTERACTIONS: HOW DO THEY COME ABOUT?

The fundamental interest in colloidal dispersions partly stems from the tunable nature of the interaction amongst their constituents. To understand how this freedom comes about and which kind of tunability we are referring to, it is advisable to stress two major points: (i) colloidal dispersions are nearly always multicomponent systems, the various components often spanning a wide range of mass, length and characteristic time scales; (ii) one usually focuses on a subset of them – more often the heaviest, biggest and slowest – and seeks for a description of the system in terms of those alone. Indeed as long as average, equilibrium properties are concerned the selected components do behave as if they were alone in the system and interacted via an effective potential energy which maintains memory of the collective, average effect of the neglected species.

This is not an uncommon operation in physics, reflecting a natural search for simplicity. For example, when considering a single molecule in which both electrons and nuclei wiggle around, the masses of the two species are so different that on the typical time scale of the nuclear motion the electrons will very rapidly relax to the instantaneous ground state configuration. Thus, it becomes possible to decouple the two dynamics: the nuclei move according to an effective potential energy function determined by solving the electronic ground state problem for each possible nuclear configuration.‖ The same line of reasoning applies to a colloidal dispersion; solely, since the number of particles involved is way higher (it is indeed in the order of Avogadro's number, $N_A \sim 10^{23}$), we must speak the language of thermodynamics. If we consider the bulkiest particles of the dispersion we may assume that on the typical time scale of their motion the other species relax very rapidly to the state of thermodynamic equilibrium, the big particles appearing to them as fixed external objects. Thus as long as the properties of the bulky component are concerned the other species may be neglected, provided an effective interaction between the big particles is introduced reflecting the instantaneous equilibrium free energy of the remainder of the system. This effective interaction, being sensible to the full details of the composition of the dispersion, is open for a high degree of customization. We stress that the approach just outlined is necessarily approximated if one is interested in dynamical quantities and transport coefficients, but it is in principle exact with regard to the equilibrium properties.

The former hand-waving arguments can be given a sound basis in the framework of statistical mechanics [60]. In this context, a colloidal dispersion is described as a complex fluid made up of a given number n_c of components. Each component k, with $1 \leq k \leq n_c$, comprises a number of particles whose instantaneous configuration is specified by a set Γ_k of suitably chosen coordinates – which may include the number of particles itself – incorporating any kind of degree of freedom (e.g. translational, rotational, vibrational) we consider pertinent for the complete description of the system. A function $U(\Theta)$, the argument denoting the union of the sets Γ_k, associates an energy to each permissible configuration. Upon the choice of the appropriate statistical

---

¶Technically, the latter is a silicone polymer – the Dow Corning® Dilatant Compound 3179 – and not a colloid, but it serves nicely to illustrate viscoelasticity.

‖This is called the adiabatic, or Born-Oppenheimer, approximation.

ensemble bound to a set Λ of independent thermodynamic variables, the equilibrium properties of the system are encoded in the partition function

$$Z(\Lambda) = \mathrm{Tr}_\Theta \, \mathcal{F}(U(\Theta), \Lambda) \,, \qquad\qquad (1.1)$$

the trace operator $\mathrm{Tr}\cdot$ and the function $\mathcal{F}(\cdot, \cdot)$ depending on the ensemble adopted. If we focus on a particular component, say $k = 1$ without loss of generality, and assume that the trace operator can be factored we may write

$$Z(\Lambda) = \mathrm{Tr}'_{\Gamma_1} \left[\mathrm{Tr}''_{\Theta \setminus \Gamma_1} \mathcal{F}(U(\Theta), \Lambda) \right] = \mathrm{Tr}'_{\Gamma_1} \mathcal{G}(\Gamma_1, \Lambda) \,, \qquad (1.2)$$

where the primes have been introduced to stress that the corresponding operators differ from the initial one. The function $\mathcal{G}(\Gamma_1, \Lambda)$ implicitly defines an effective interaction among the particles of the selected species, which in general will depend both on the instantaneous configuration of the particles and on the thermodynamic state of the system.** Note that the previous definition holds even if we focus on more than one component at a time (retaining, say, the degrees of freedom contained in Γ_1 and Γ_2) and regardless of their nature: they need not be the bulkiest or biggest ones, as the qualitative argument introduced earlier in the text seemed to suggest. In practice, however, the concept of effective interaction proves a handy tool mostly if applied to systems characterized by particles spanning a wide range of size and mass scales and when focusing on the high end of that range: otherwise, the result might turn out to be so complex to be completely useless. Thankfully, colloidal dispersions show all the necessary features for this abstraction to be fruitfully applied [18].

PARTICLE DEPLETION, CHARGE SCREENING AND CRITICAL CASIMIR EFFECT

We conclude this survey by introducing a number of notable phenomena taking place in colloidal dispersions and leading to effective interactions which will play a major role in the remainder of the thesis.

Consider a room overcrowded with people wandering around erratically in all directions (and, of course, they do not mind bumping into other people or objects – packed-up dancers in a disco club could serve as a nice example): if you wait long enough, you will find that most of the objects contained in the room lie lumped together or rest near the walls, since in this way the space available for the people to move in is maximized. Similarly, consider a colloidal dispersion made up of small particles wiggling around ceaselessly as a consequence of their thermal agitation: if a number of big particles are added to it, they will experience a short-range, attractive force striving to push them together. This is termed *depletion interaction*, since it originates from the fact that the volume of the container inaccessible to the small particles, i.e. the volume from which they are depleted, becomes smaller if the big particles stick together or to the walls, just as the restless dancers in the previous example gain free space by pushing together the objects found in their way. The first historical record of a depletion interaction, later to become paradigmatic, is linked to the names of Sho Asakura and Fumio Oosawa as they considered in 1954 the effective attraction arising between two bodies in a solution of macromolecules [5]. By

---

**The exact definition of the effective interaction depends on the form of the operator Tr'_{Γ_1}; for example, if the number of particles N_1 of the selected species is not fluctuating (so that $N_1 \in \Lambda$) and $\mathrm{Tr}'_{\Gamma_1} \propto \int d\Gamma_1$, then $Z(\Lambda)$ coincides with the canonical partition function of a system of particles interacting through an effective potential $U_1^{\mathrm{eff}}(\Gamma_1, \Lambda)$ proportional to $\log \mathcal{G}(\Gamma_1, \Lambda)$, which is indeed some kind of equilibrium free energy of the neglected components.

approximating the macromolecules to non-interacting spheres having diameter d, in a remarkable two-column article they provided (amongst other results) a formula for the force acting between two big spheres of diameter D immersed in the solution:

$$
F(r) = \begin{cases} -(\pi/4)\, p_0 \left\{ (D+d)^2 - r^2 \right\} & D < r < D + d\,, \\ 0 & r > D + d\,, \end{cases}
\tag{1.3}
$$

r being the centre-to-centre distance between the spheres and p_0 the osmotic pressure of the macromolecules. The force is attractive, has a maximum when the spheres are touching and decreases towards zero as the surface-to-surface distance approaches the size of the macromolecules. In real systems the ratio d/D, which characterizes the range of the attraction, can be as low as a few percentage points: in these cases, one often speaks of a *sticky interaction*.[††] A distinct feature of systems presenting short-range attractive interactions is a metastable gas-liquid transition, often associated with arrested gel or glassy phases [27, 86]; depletion forces are also believed to play a role in a number of biological organization processes [89].

Other phenomena of primary relevance in colloidal science stem from the ubiquitous presence of electric charges. A colloidal particle, when placed in a solvent, usually develops an electric charge owing to ionization of dissociable groups on its surface or adsorption of ions already present in the solution. Were it not for the presence of mobile ions, the energy of interaction between charged spherical colloids would adhere to the familiar long-range Coulomb law, and statistical physicists would be spared many a headache. Unfortunately, the electrical state of a charged colloid and its interaction with other charged surfaces depend crucially on the distribution of mobile ions around it emerging from the competition of electrostatics and thermal motion [96]. The resulting charge distribution, at least in the simplest model conceivable, is made up of two layers, the first being the charge firmly bound to the surface of the particle, the other the charge distributed more or less diffusely within the solution in contact with the surface: this layer contains an excess of counterions (ions opposite in sign to the fixed charge) and has a deficit of co-ions (ions having the same sign as the fixed charge). Due to the screening effect of the diffuse layer, as one walks away from the particle, the electrostatic potential ϕ decays much faster than it would do in the presence of the fixed charge alone; sufficiently far from the surface, it is well represented by a Yukawa form [17]:

$$
\phi(r) \propto \frac{\exp\left[-\kappa(r-a) \right]}{r/a}\,,
\tag{1.4}
$$

r being the distance from the center of the particle and a its radius. The quantity κ^{-1} defines the characteristic length over which the electrostatic potential brought about by the particle decays: it is a property of the electrolytic solution alone – the larger the ionic strength, the more effective the screening. The energy of interaction of two charged, spherical colloids follows from the electrostatic potential; as long as a superposition approximation of the respective ionic clouds holds, it inherits the simple Yukawa form and decays over the same length scale. Thus, by controlling the amount of mobile ions floating around, for example by the addition of a salt to the dispersion, one can tune the range of the electrostatic interaction in a precise and reproducible manner. Screened Coulomb interactions, unless the regime of complete screening is enforced, are invariably at work in colloidal dispersions, even when other kinds of interactions prevail.

[††]To get a grasp of the length scales involved, think about a normal-sized billiard ball coated with a millimeter-thick layer of adhesive tape.

A third class of effective interactions, which ends this short review, is of a completely different origin, since it has roots in the realm of critical phenomena accompanying second-order phase transitions [131]. When fluctuating fields are confined between two surfaces, effective long-range forces arise: the most famous example is the quantum-electrodynamical Casimir force due to the vacuum fluctuations of the electromagnetic field being confined to the space separating two conducting, uncharged metal plates [29]. A thermodynamic analogue of the quantum-electrodynamical effect exists: it is called the *critical* Casimir force and has been first described by Michael E. Fisher and Pierre-Gilles de Gennes in 1978 [47]. The critical Casimir force acts between two surfaces immersed in a fluid when the latter is close to a critical point; it originates from the thermal fluctuations of the order parameter for the phase transition being confined in the thin liquid layer separating the two surfaces. Forces belonging to this class are generally weak (tens to hundreds of femto-Newton) and only recently a direct measurement of their intensity has become possible [59]. Nonetheless, the high degree of tunability both in strength and sign (attraction or repulsion) may be harnessed to serve dedicated purposes in colloidal dispersions and in micro-mechanical devices [130, 7, 74]. As a further bonus, critical Casimir forces are to a good extent universal, that is independent – at least in theory – of the specific nature of the underlying critical system.

SCOPE AND OVERVIEW OF THE THESIS

We conclude the introduction by summarizing the contents of the thesis. Its structure does not follow any particular plan, since the subjects discussed, although all related to the field of colloidal physics, are heterogeneous and not necessarily connected. The aim was to explore diverse areas in the field facing questions as they were raised by experimental evidence or simple curiosity.

Previously in the text it was stated that interesting phenomena arise in colloidal dispersions when short-range, attractive forces due to the depletion mechanism act. In Chapter 2 we seek an analytic, thermodynamically consistent method to obtain the equilibrium properties of a system of sticky hard spheres.

In Chapter 3 we proceed with our investigation of the depletion interaction. Prompted by experimental evidence, we ponder on the departure from the simple Asakura-Oosawa picture brought about by the presence of electric charges in the system.

Chapter 4 develops a general framework capable of describing both the depletion interaction and the critical Casimir force. Stimulated again by experimental results, we show that the two are not completely different phenomena but instead two ends of a continuum.

Finally, Chapter 5 is devoted to an analysis of the effect of polydispersity, that is a stochastic variation in size and charge, on the freezing transition of a collection of charged hard spheres. This is accomplished by means of Monte Carlo simulation techniques.

2

Self-Consistent Ornstein-Zernike Approximation for a System of Sticky Hard Spheres

ABSTRACT

We propose an approximate method to obtain the equilibrium properties of a system of hard spheres with surface adhesion, seeking an improvement upon the well known Percus-Yevick solution. Assuming the direct correlation function to vanish beyond the range of the potential, in the sticky limit the thermodynamics of the system are seen to depend on a single scalar parameter varying with the density and the effective temperature. In order for thermodynamic consistency to be ensured, this parameter must satisfy a certain nonlinear differential equation that we derive and attempt to solve numerically. A pronounced sensitivity to the boundary conditions suggests that the self-consistent approach is inadequate for the class of sticky interparticle potentials.

I N Chapter 1 we introduced the depletion mechanism as a means to induce an effective, short-range attraction among colloidal particles. The general idea can be put into action in a number of ways. For example, when a certain amount of a non-adsorbing polymer is added to a colloidal dispersion, the chains of the polymer fold into spherical coils acting as depletion agents [119]. Moreover, by playing with the temperature and composition of the solvent and with the molecular weight of the polymer, the size of the coils and, hence, the range of the depletion interaction can be readily adjusted; often as not, it is a small fraction of the size of the particles. A notable effect of the depletion-induced attraction is the appearance in the equilibrium phase diagram of the dispersion of a possibly metastable region in which two fluid phases with different density coexist [66], a phenomenon entirely similar to the liquid-vapor phase coexistence taking place in simple gases.

A short-range, attractive interaction is naturally defined by an energy scale ϵ, expressing the depth of the potential well in units of the thermal energy, and by a length scale δ, corresponding to the range of the attraction in units of the typical size of the colloids. As long as $\delta \ll 1$ the specific shape of the potential, when observed with a level of detail appropriate for the colloidal particles, gets somewhat blurred and thus plays a minor role: indeed, the thermodynamic state of the fluid is much more sensitive to quantities that measure the overall strength of the potential such as the second virial coefficient.* This is often expressed with the mantra "all short-range potentials are equivalent"; in fact they are not, nonetheless it is a common practice to compare two such potentials on the basis of their virial coefficients, partly in the spirit of the extended law of corresponding states conjectured by Noro and Frenkel [95].

In the real world the range of the depletion-induced attraction cannot be reduced at will: a lower bound exists connected with the unavoidable roughness affecting the surface of the particles.† In the ideal world of physical models, instead, nothing prevents the range to become infinitesimal; for the effect of the potential not to disappear altogether, its energy scale must at the same time become infinite. If this is done in such a way that the second virial coefficient attains a finite value, the *sticky hard sphere* model (or hard spheres with surface adhesion) is born. The model was introduced in 1968 [14] by the Australian physicist Rodney James Baxter – later to become most renown for his work on exactly solved models in statistical mechanics – and is defined as a system of identical spherical particles interacting through a pairwise additive potential energy function taking the following form:

$$\beta v_\tau(r) = \begin{cases} +\infty & 0 \leq r < 1 \\ -\log\left[(1 + \delta^{-1})/(12\tau)\right] & 1 \leq r \leq 1 + \delta \\ 0 & r > 1 + \delta \end{cases} ; \qquad (2.1)$$

in the previous definition, and also in the remainder of this chapter, the particle diameter is taken as the unit of length, r is the center-to-center distance between the pair of particles, $\beta = 1/k_\mathrm{B}T$, with k_B Boltzmann's constant and T the temperature, is the inverse thermal energy and the so called sticky limit, corresponding to $\delta \to 0^+$, is understood. The positive parameter τ, quantifying the stickiness of the potential, plays the role of a dimensionless effective temperature: when it is infinite a system of hard spheres is recovered; as it is lowered the adhesion between the particles first sets

---

*We recall that the second virial coefficient is an easily accessible quantity characterizing the departure of a fluid from the ideal gas model and is proportional to the volume integral of the Mayer function of the potential; see Ref. [60].

†For example, one cannot expect micrometer-sized silica or latex colloids to experience an effective attraction due to the depletion of water molecules, since the volume of the region from which the latter are depleted is nearly independent of the position of the colloids.

in and then becomes stronger. The corresponding second virial coefficient

$$B_2(\tau) = -\frac{1}{2} \int d\boldsymbol{r} \, (e^{-\beta v_\tau(r)} - 1) = B_2^{\mathrm{HS}} \left(1 - \frac{1}{4\tau}\right) \qquad (2.2)$$

reflects the same behavior, attaining the hard sphere value B_2^{HS} at infinite effective temperature and becoming more and more negative as τ is reduced. Following the conjecture of universality introduced earlier in the text, expression (2.2) is commonly used to map an attractive potential with a short but nonvanishing range onto the sticky hard sphere model [114]. The puzzling numerical factor multiplying the effective temperature in the definition (2.1) is by no means essential nor it simplifies the expressions later to be reported: although it could easily be dropped, it is retained for the sake of consistency with the original definition.

The sticky limit was devised by Baxter as a matter of mathematical convenience: he was looking for a simple model showing a liquid-vapor phase transition which was amenable to an analytic, although approximate, solution in the contest of the theory of correlation functions in simple liquids. Even if the model, as we will summarize later, has a perfectly regular solution in the Percus-Yevick approximation and has also been the subject of extensive simulation studies [126, 72, 91], the singularity embedded in its very definition should instigate a mild feeling of suspicion. In fact, twenty-three years after the appearance of the model George Stell and G. O. Williams discovered that the latter from a rigorous statistical mechanical point of view is thermodynamically unstable whenever the number of particles is greater than eleven [133]. However, the state of affairs is less serious than it might seem: the instability arises from a number of rather fancy particle configurations that are readily destroyed by the slightest amount of polydispersity in the system. Therefore, the sticky hard sphere model and its approximate analytical solution still remain a valuable tool for the interpretation of the phase diagram of colloidal dispersions subject to short-range, depletion-induced interparticle interactions.

2.1 THE PERCUS-YEVICK SOLUTION

As we mentioned earlier, Baxter was able to solve his newly introduced model making use of the Percus-Yevick integral equation, a popular approximation from the theory of simple liquids [57] which was known to yield fairly good results when applied to a system of hard spheres without adhesion.

For a uniform fluid consisting of particles interacting via central forces, the total correlation function $h(r)$ may be defined in terms of the pair radial distribution function as

$$h(r) = g(r) - 1 \,. \qquad (2.3)$$

In addition, the direct correlation function $c(r)$ may be defined by the Ornstein-Zernike relation [99]

$$h(r) = c(r) + \rho \int d\boldsymbol{r}' \, h(r') \, c(|\boldsymbol{r} - \boldsymbol{r}'|) \,, \qquad (2.4)$$

where ρ is the particle number density. In terms of these functions the Percus-Yevick approximation can be expressed as

$$c(r) = \{1 - \exp[\beta v(r)]\} \, g(r) \,, \qquad (2.5)$$

$v(r)$ being the interparticle potential. Note that $c(r)$ vanishes whenever $v(r)$ does, that is the direct correlation function has the same range as the interparticle potential.
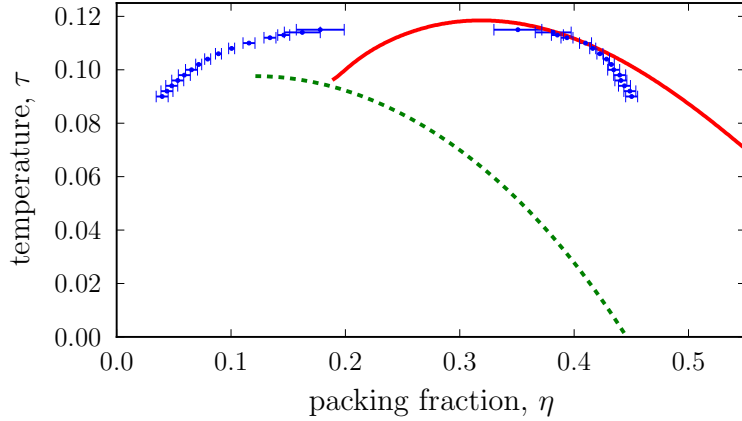
Figure 2.1: Phase diagram of the sticky hard sphere model in the Percus-Yevick approxima-
tion. Full line: spinodal from the energy route; dashed line: spinodal from the compressibility
route (note that it exists only to the right of the critical point). For the sake of comparison,
the symbols show the phase boundary of the liquid-vapor phase transition according to the
Monte Carlo simulation data reported in Ref. [91].

When the definition (2.1) is inserted in the previous equations and after taking the
sticky limit it can be shown [14, 9] that the correlation functions depend on a single
real parameter λ_{PY} given by the following expression:

$$\lambda_{\mathrm{PY}} = (6 - \tau + \tau\eta^{-1}) - \left[(6 - \tau + \tau\eta^{-1})^2 - 6(1 + 2\eta^{-1})\right]^{1/2} , \qquad (2.6)$$

where $\eta = (\pi/6)\rho$ represents the packing fraction of the system and the result is phys-
ically admissible only when $\lambda_{\mathrm{PY}} < 2 + \eta^{-1}$. From this single parameter the complete
thermodynamics of the system follows; for example, the inverse isothermal compress-
ibility as determined by the sum rule involving the direct correlation function [57]
equals

$$\chi_{\mathrm{PY}}^{-1} = \frac{\partial\beta P_{\mathrm{PY}}}{\partial\rho} = a_{\mathrm{PY}}^2 , \qquad a_{\mathrm{PY}} = \frac{1 + 2\eta}{(1 - \eta)^2} - \frac{\lambda_{\mathrm{PY}}\eta}{1 - \eta} , \qquad (2.7)$$

whereas the Helmholtz free energy per particle departs from the hard-sphere value
according to the relation

$$\frac{\beta A_{\mathrm{PY}}}{N} = \frac{\beta A_{\mathrm{HS}}}{N} - \eta \int_{\tau}^{+\infty} d\tau' \, \lambda_{\mathrm{PY}}/\tau' . \qquad (2.8)$$

Starting from either Equation (2.7) or Equation (2.8) one can obtain the phase di-
agram of the sticky hard sphere model in the Percus-Yevick approximation:[‡] in the
former case one speaks about the *compressibility route*, whereas in the latter case
the *energy route* is pursued. Of particular interest is the spinodal line, i.e. the locus
of vanishing inverse isothermal compressibility which bounds the region where the
system becomes unstable with respect to local density fluctuations that eventually

---

[‡]Of course we are not referring to the complete phase diagram, since the Percus-Yevick approxi-
mation, similarly to all the approaches based on the Ornstein-Zernike relation (2.4), is entirely blind
to any phase transition – such as freezing – that breaks the translational and rotational symmetry
of the system.

lead to the liquid-vapor phase separation. Along the compressibility route it follows readily from

$$\chi_{\mathrm{PY}}^{-1} = 0 \,, \tag{2.9}$$

while along the energy route it is defined by the requirement

$$\frac{\partial^2}{\partial \eta^2} \left[\eta \, \frac{\beta A_{\mathrm{PY}}}{N} \right] = 0 \,. \tag{2.10}$$

If the Percus-Yevick relation (2.5) were exact, the two routes would yield identical results; instead, they prove thermodynamically inconsistent, as Figure 2.1 attests. In the same figure, the boundary of the domain of liquid-vapor phase coexistence as determined by Monte Carlo simulations is shown: at the very least, the three curves ought to meet at the critical point, but manifestly they do not. This state of affairs seriously hinders the adoption of the Percus-Yevick approximation for the quantitative interpretation of experimental data and thus limits its usefulness. It is our purpose here to find out if enforcing the consistency between the compressibility route and the energy route would eventually lead to a better approximation.

2.2   ENFORCING THERMODYNAMIC CONSISTENCY

First of all, we drop the Percus-Yevick relation (2.5) in favor of the more general assumption that the direct correlation function $c(r)$ vanishes beyond the range of the interparticle potential:

$$c(r) = 0 \quad \text{for } r > 1 + \delta \,. \tag{2.11}$$

The latter hypothesis does not define a unique approximation, but instead identifies an entire class of closures of the Ornstein-Zernike equation (2.4) among which the Percus-Yevick is but a particular case. This class has already been investigated in the literature; see for example Gazzillo and Giacometti [51]. Remarkably, in the sticky limit the differences among the various closures are drastically reduced, all being included in a common parameter λ, and the direct correlation function acquires a fixed form:

$$c(r) = \left\{ -\frac{\eta \lambda}{r} - a^2 + \eta \left[6(a+b)^2 - a\lambda \right] r - \frac{\eta a^2}{2} r^3 \right\} \theta(1-r) + \frac{\lambda}{12} \delta_{\mathrm{D}}(r-1) \,; \tag{2.12}$$

in the previous expression $\theta(\cdot)$ designates the step function, $\delta_{\mathrm{D}}(\cdot)$ is Dirac's delta function and the quantities a and b are so defined:

$$a = \frac{1+2\eta}{(1-\eta)^2} - \frac{\lambda \eta}{1-\eta} \,, \tag{2.13a}$$

$$b = -\frac{3\eta}{2(1-\eta)^2} + \frac{\lambda \eta}{2(1-\eta)} \,. \tag{2.13b}$$

The thermodynamic state of the fluid is entirely determined by the value of the parameter λ, which is a function of the packing fraction η and the effective temperature τ; moreover, it bears a simple relation to the contact value of cavity function $y(r) = g(r) \, e^{\beta v_\tau(r)}$, which is known to be regular and continuous even at the hard-core diameter $r = 1$ or where the interparticle potential has other discontinuities:

$$\lambda = \tau^{-1} y(1) \,. \tag{2.14}$$

The compressibility sum rule applied to Equation (2.12) gives for the inverse isothermal compressibility

$$\chi^{-1} \;=\; 1 - \rho \int d\boldsymbol{r}\, c(r) \;=\; a^2\,, \tag{2.15}$$

whereas following Baxter et al. [143] the Helmholtz free energy per particle departs from the hard-sphere value according to

$$\frac{\beta A}{N} = \frac{\beta A_{\mathrm{HS}}}{N} - \eta \int_{\tau}^{+\infty} d\tau'\, \lambda/\tau'\,. \tag{2.16}$$

Note that the Percus-Yevick results (2.7) and (2.8) are particular cases of Equations (2.15) and (2.16) respectively.

In order for the thermodynamic properties of the fluid deduced from the isothermal compressibility χ and from the Helmholtz free energy A to coincide for all state points (η, τ), the following thermodynamic identity ought to be satisfied (which is *not* in the Percus-Yevick approximation):

$$\chi^{-1} = \eta \frac{\partial^2}{\partial \eta^2} \left[\eta \frac{\beta A}{N} \right]\,. \tag{2.17}$$

The previous expression, once Equations (2.15) and (2.16) are taken into account, is an integro-differential equation constraining the as yet unknown parameter λ. Defining an inverse dimensionless temperature

$$t = \tau^{-1}\,, \tag{2.18}$$

upon differentiating both sides of the identity with respect to t and rearranging terms, an equivalent partial differential equation is found:

$$\frac{2a}{1-\eta}\, t\, \dot{\lambda} = (\eta^2 \lambda)''\,, \tag{2.19}$$

where the dot means differentiation with respect to t, whereas the prime denotes differentiation with respect to η.

Before attempting a solution of the equation, a remark is appropriate. The strategy we pursued, which entails fixing the form of a correlation function of the fluid so that it contains a free state-dependent parameter to be determined by imposing the consistency between two different routes to thermodynamics, falls in the class of the so called self-consistent Ornstein-Zernike approximations (SCOZAs). Therefore the idea is not original (it has indeed been applied in the past to a broad range of systems [78, 63, 115, 123]), nonetheless this is to our knowledge the first documented attempt to apply the SCOZA technique to the sticky hard sphere model.

2.3   AN ATTEMPTED NUMERICAL SOLUTION

Equation (2.19) lacks an analytic solution, hence we resort to a numerical method. For this purpose, it is convenient to define the auxiliary quantity

$$\Lambda = \eta^2 \lambda \tag{2.20}$$

by means of which the consistency equation becomes

$$D^{-1}\dot{\Lambda} = \Lambda''\,; \qquad D^{-1} = 2t \left[\frac{1+2\eta}{\eta^2(1-\eta)^3} - \frac{\Lambda}{\eta^3(1-\eta)^2} \right]\,. \tag{2.21}$$

This is a quasilinear diffusion equation with a state-dependent diffusion coefficient D in which t and η play the role of a timelike variable and a spacelike variable, respectively. An efficient, implicit predictor-corrector scheme for the resolution of equations of the latter kind exists; a detailed description can be found in the appendix of Ref. [107].

For the problem to be completely specified, Equation (2.21) must be complemented with suitable boundary conditions. The high temperature behavior, that is t approaching zero, is needed as an initial condition to start the integration. Although in this limit the system reverts to a hard sphere model and is perfectly regular, the numerical scheme cannot be initiated from $t = 0$ since corresponding to this value the equation is singular due to the diffusion coefficient becoming infinite. Instead we start from a small but not null $t_0 > 0$ using as an initial condition the first-order approximation

$$\Lambda(t_0, \eta) \approx t_0 \psi(\eta), \tag{2.22}$$

where the η-dependent term must satisfy the corresponding asymptotic form of Equation (2.21):

$$2\left[\frac{1 + 2\eta}{\eta^2(1-\eta)^3}\right]\psi = \psi''. \tag{2.23}$$

The latter is a Fuchsian differential equation [4] whose indicial equation has two integer roots, $r = -1, 2$: therefore, a unique solution exists analytic in a neighborhood of $\eta = 0$ that can be expressed in the form $\psi(\eta) = \sum_{n=2}^{\infty} a_n \eta^n$. The coefficients of the series expansion are completely determined by Frobenius method and the requirement $a_2 = 1$, which follows through Equation (2.14) from the property [51]

$$\lim_{\eta \to 0} y(1) = 1. \tag{2.24}$$

We verified *a posteriori* that the numerically computed solution of Equation (2.21) is virtually independent of the particular choice of the initial inverse temperature t_0 as long as the latter is sufficiently small and the initial solution is set according to Equation (2.23).

As the inverse temperature is increased from the initial value t_0, the numerical integration scheme proceeds by computing the solution on a grid of η-points belonging to an interval $[\eta_L, \eta_H]$; boundary conditions at both ends must be provided. The low density boundary poses no problem: setting $\eta_L = 0$, the property (2.24), together with the relations (2.14) and (2.20), imply

$$\Lambda(t, \eta_L) = 0 \quad \text{for all } t. \tag{2.25}$$

The high density behavior is more problematic: as it is not known beforehand, a certain amount of arbitrariness exists both in the value of the function Λ at the boundary and in the position η_H of the boundary itself. This is a problem common to all the approximations belonging to the SCOZA class: the usual way out consists in using another type of approximation to set the boundary. Since there is not any obvious recipe for singling out a specific high density boundary condition, a natural requirement is that the results at low and intermediate densities should not depend on the detailed form of such a condition, or on the packing fraction η_H at which it is imposed. Previous studies of fluids with short-range interparticle potentials within the SCOZA framework [115, 123] showed that for this to happen the boundary might
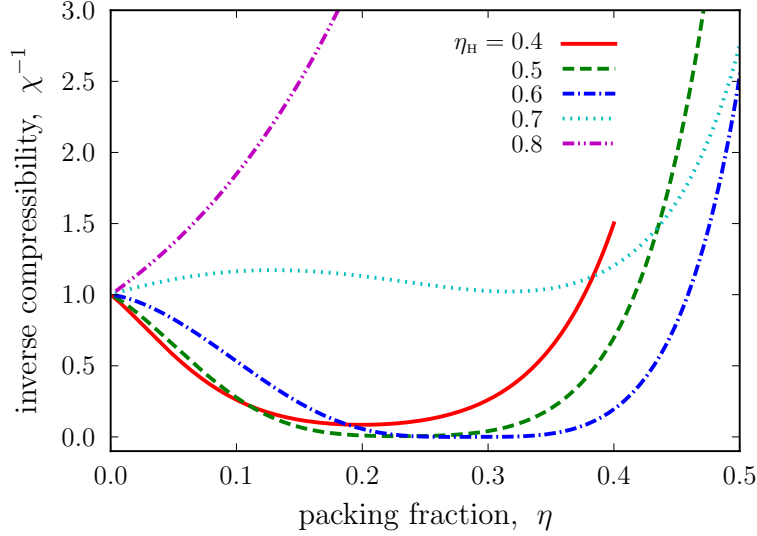
Figure 2.2: The inverse isothermal compressibility of the sticky hard sphere fluid plotted against the packing fraction as found within the SCOZA approach with a high density boundary condition computed in the Percus-Yevick approximation. The different lines show the effect of changing the position η_{H} of the boundary. The effective temperature is set according to Monte Carlo simulations [91] at the almost critical value $\tau = 0.11$.

have to be set close to or even beyond close-packing ($\eta_{\mathrm{CP}} = \pi\sqrt{2}/6$), which is in fact unphysical but perfectly legal as long as the equations are concerned.

In the present case an obvious choice for the high density boundary condition is the Percus-Yevick approximation (2.6):

$$\Lambda(t, \eta_{\mathrm{H}}) = \eta_{\mathrm{H}}^2 \lambda_{\mathrm{PY}} \quad \text{for all } t \, ; \tag{2.26}$$

another popular alternative, namely the high-temperature perturbative expansion [98, 57] using as a reference system the hard sphere model, is not feasible here since it yields a null perturbation to first order. The outcome of integrating Equation (2.21) with a Percus-Yevick high density boundary is shown in Figure 2.2, where the inverse isothermal compressibility of the fluid χ^{-1} is plotted against the packing fraction η corresponding to different choices of the position η_{H} of the boundary; all curves refer to the same effective temperature $\tau = 0.11$, which is close to the critical one according to Monte Carlo simulations [91]. The end result is quite disappointing: the compressibility is seen to depend noticeably on the position of the boundary. For the solution to be deemed reliable the various curves, at least for η_{H} greater than a certain threshold, ought to lie near one another – a requirement that is manifestly *not* satisfied. We also notice that some of the lines are not even consistent with $\tau = 0.11$ being close to the expected critical temperature of the model. Since we do not see at the moment any other reasonable choice to estimate the high density boundary apart from the Percus-Yevick approximation, we are in a kind of dead end.

One may object that this situation does not represent by itself a failure of the SCOZA equation (2.21), but merely attests our ignorance of the real boundary condition: if the latter were known, the equation might as well give consistent results. To elaborate further on this point, we seek a method to solve the equation that does not
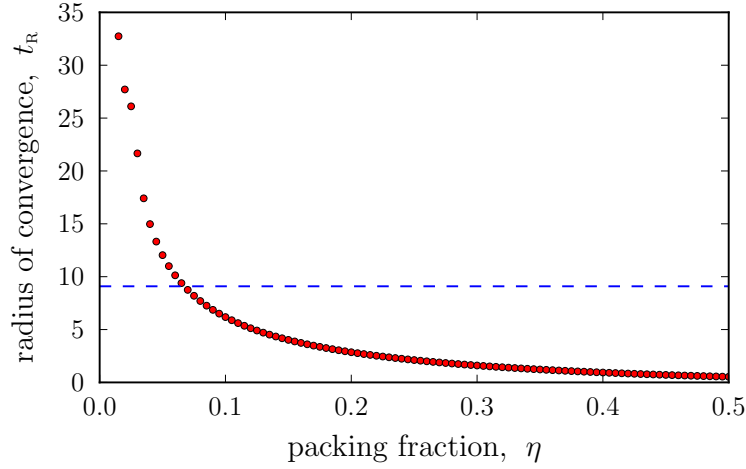
Figure 2.3: The radius of convergence of the formal series (2.27), estimated by means of the ratio convergence test, plotted as a function of the packing fraction of the fluid. The horizontal dotted line marks the value of the inverse temperature corresponding to the critical point according to Monte Carlo simulations [91].

require the high density boundary to be specified. Let us suppose that the unknown function Λ can be expressed as a power series of the inverse temperature t

$$\Lambda(t, \eta) = \sum_{n=1}^{\infty} t^n \varphi_n(\eta) \,, \tag{2.27}$$

where the constant term has been omitted since the function must vanish in the limit of infinite temperature. Owing to the previous definition the SCOZA equation is seen to be equivalent to an infinite set of ordinary differential equations:

$$\varphi_n'' = 2n \left[\frac{1 + 2\eta}{\eta^2 (1 - \eta)^3} \right] \varphi_n - \left[\frac{2}{\eta^3 (1 - \eta)^2} \right] \sum_{j=1}^{n-1} j \, \varphi_j \, \varphi_{n-j} \,, \qquad n = 1, 2, \ldots \,; \tag{2.28}$$

note that corresponding to $n = 1$ Equation (2.23) is recovered. Although the set is infinite, it merely contains backward references: for this reason, the equations can be solved in a sequential fashion up to any desired order $\bar{n}$. Moreover, to compute the solution of any one equation in the set, say number k, only the low density behavior of the function φ_k, that is the value of the function and its first two derivatives at $\eta = 0$, needs to be specified as an initial condition. Luckily, results of exact diagrammatic expansions [51] show that only a small subset (specifically $k < 6$) of the initial conditions are not vanishing and also provide an estimate for the nonzero values.

If one proceeds along this route a formal, approximated solution of the consistency equation (2.21) can be obtained up to any desired accuracy (compatibly with numerical truncation errors due to a finite machine precision) in the form of a sequence of coefficients $\varphi_1, \ldots, \varphi_{\bar{n}}$. Unfortunately, as Figure 2.3 attests, once the coefficients are plugged back into the power series (2.27) the radius of convergence $t_{\rm R}$ corresponding to most values of the packing fraction η comes out way too small for the series to have any practical use in this form. Although the situation is disappointing, it is not uncommon: a power series obtained as a formal solution of a differential equation may
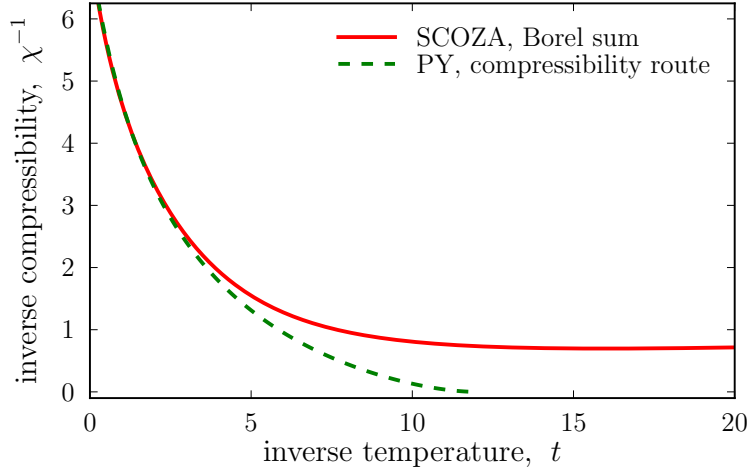
Figure 2.4: The inverse isothermal compressibility of the sticky hard sphere fluid plotted as a function of the inverse temperature along the $\eta = 0.25$ isochore. The compressibility route of the Percus-Yevick approximation (dashed line) predicts the compressibility to become infinite at $t \approx 12$ (that is $\tau \approx 0.08$, see also Figure 2.1). According to the solution of the SCOZA equation evaluated by means of the Borel summation method (full line), the isochore does not cross the spinodal line at all.

easily turn out to be divergent. In those cases, one can try a resummation technique in the attempt to provide an analytic meaning to such a divergent series. Accordingly, as a last resort we now apply the *Borel summation formula* [70] to the power series (2.27).

For this purpose, we define the regularized power series

$$\tilde{\Lambda}(s, \eta) = \sum_{n=1}^{\infty} \frac{s^n}{n!} \, \varphi_n(\eta) \tag{2.29}$$

that has an improved radius of convergence due to the factorial term in the denominator, then we correct for this term by means of the Laplace integral

$$\Lambda_{\mathrm{B}}(t, \eta) = t^{-1} \int_0^{+\infty} ds \; e^{-s/t} \, \tilde{\Lambda}(s, \eta) \,. \tag{2.30}$$

Where the original series is convergent, the two functions Λ and Λ_{B} are in fact identical; the latter, however, yields a finite value in a much larger domain. If one is willing to trust the Borel sum Λ_{B} in this enlarged region, then a puzzling result is found: the liquid-vapor phase transition disappears from the phase diagram, at least corresponding to reasonable values of the packing fraction and the temperature. In Figure 2.4, for example, the inverse isothermal compressibility of the fluid is plotted against the inverse temperature along the $\eta = 0.25$ isochore: while the compressibility route of the Percus-Yevick approximation predicts the compressibility to become infinite around $\tau \approx 0.08$, according to the solution of the SCOZA equation evaluated by means of the Borel summation method the compressibility stays finite even if the temperature is lowered further. This is clearly at odds with both routes of the Percus-Yevick approximation and with the results of Monte Carlo simulations (recall Figure 2.1).

2.4 CONCLUSIONS

Our investigation was prompted by the lack of a theory that would account quantitatively for the liquid-vapor phase transition in a system of sticky hard spheres: the various routes to the thermodynamics of the fluid starting from the well known and highly cited Percus-Yevick approximation are inconsistent with each other and agree only qualitatively with the results of computer simulation. Following the documented success of the self-consistent Ornstein-Zernike approximation in a number of systems, we wondered whether enforcing thermodynamic consistency within a class of generalized Percus-Yevick approximations for the sticky hard sphere fluid would eventually lead to an improvement upon the standard Percus-Yevick solution. After struggling with the ensuing partial differential equation, we conclude that the answer is negative: the self-consistent Ornstein-Zernike approach proves inadequate for a system with a sticky interparticle potential. Indeed, if the equation is solved directly a pronounced sensitivity to the high density boundary condition renders the solution unreliable; if, on the contrary, the equation is turned into a set of ordinary differential equations and the low density behavior alone is imposed, the liquid-vapor phase transition disappears altogether.

Stating that the SCOZA approach is inadequate is merely an observation and does not shed any light on the reason behind the fact. In the light of the results of Stell and Williams [133] briefly mentioned in the introduction of the chapter, one may wonder if the failure must be attributed to the approximation or to the model itself that, we recall, is strictly speaking ill-defined if a class of problematic configurations of particles is not ruled out. Can it be that the (possibly more accurate) self-consistent Ornstein-Zernike approach exposes the malicious effect of the divergent clusters, which are simply neglected in the Percus-Yevick approximation? This is improbable, since the two approximations are quite similar in their handling of the correlation functions of the fluid. What we deem most probable, instead, is that the failure is a combined effect of the approximate closure (2.11) and the consistency requirement (2.17). Indeed, the closure is likely to miss a number of singular features that show up in the real correlation functions [87]: the isothermal compressibility, being dependent on the volume integral of the direct correlation function, inherits this flaw. On the contrary, the Helmholtz free energy of the fluid only depends on the contact value of the cavity function: when the requirement of thermodynamic consistency is imposed, it has to compensate for the contributions missing in the compressibility, unnaturally pushing away the liquid-vapor phase boundary. We stress that this is at the moment a mere, untested hypothesis.

3

Coulomb Enhancement of the Depletion Interaction

ABSTRACT

We study how the effective depletion force induced on spherical colloids by a fluid of smaller particles departs from the paradigmatic Asakura-Oosawa model when electric charges are present both on the colloids and the depletant particles. Upon modeling the system as a binary mixture with screened-Coulomb repulsive interparticle interactions, we apply the hypernetted-chain integral equation to derive the effective pair potential characterizing an equivalent one-component system containing the colloids alone. The Coulomb repulsion triggers two distinct effects, namely an increase in the osmotic pressure of the depletant and a condensation of the depletant particles near the surface of the colloids, which contribute in contrasting ways to the effective potential. By postulating a high structural charge on the colloids, an enhancement of the depletion force is predicted. A consistent semi-quantitative interpretation of experimental data corroborates the analysis.

Q UERYING a bibliographic database for the number of citations to the mid-fifties article by Sho Asakura and Fumio Oosawa [5], a remarkable quantity is found.* This testifies that their simple and clever analysis of the interaction between two bodies immersed in a solution of macromolecules is almost universally invoked when some kind of depletion effect is at work, at least as a first approximation used to develop a qualitative feeling about the phase behavior of the physical system. However, quite often the assumption of ideality of the depletant underlying the Asakura-Oosawa result may be poorly met, resulting in too crude an approximation to be satisfied with. What is more, the two distinctive features of the Asakura-Oosawa picture, namely (i) that the range of the effective interaction is precisely equal to the size of the macromolecules, and (ii) that the interaction is always attractive, with a strength linear in the macromolecules concentration, might require a substantial revision if the assumption of ideality is dropped. This is the main reason behind the need for a theory of the depletion effect in correlated depletants.

A first and much studied generalization of the Asakura-Oosawa result addresses depletants whose particles possess a core, so that the dispersion can be assimilated to a binary mixture comprising "big" (the colloids) and "small" (the particles making up the depletant) hard spheres. In such a model the effective colloid-colloid pair potential, despite retaining its distinctive attractive character at short surface-to-surface separation, develops an oscillating tail that extends well beyond the range set by the small particle diameter, so that domains of attraction and repulsion alternate as the colloids are moved apart. This oscillatory behavior is a distinguishing feature of the effective interaction brought about by correlations in the depletant and becomes more and more pronounced the higher the packing fraction of the small spheres is. This scenario has been independently and consistently confirmed by computer simulation [21, 36], approximate theories [88], density functional theory [52, 117], and experiments [31, 119, 16]. If one were to ask if the presence of the cores enhances or hinders the depletion mechanism compared to the ideal Asakura-Oosawa model, the answer would not be definite. Indeed, while at low density a hard-sphere depletant may be regarded as an almost ideal fluid with an improved osmotic pressure, hence pushing the colloids towards each other in a more effective way, beyond a certain density packing effects become dominant, and the repulsive shoulders in the potential eventually take over.

As a further step towards a comprehensive theory that could be applied to a broad range of colloidal dispersions, a soft tail beyond the hard core may be considered both in the depletant self-interaction and in the colloid-depletant interaction. Unfortunately, in this context the understanding of the physical processes at work and the predictive power of the theory are not as well established as in the previous case, nor the investigations as numerous. Experiments by Tohver and coworkers [138, 137] indicate that a colloidal dispersion can actually be stabilized against flocculation by the addition of a sufficient amount of highly-charged nanoparticles, a phenomenon completely opposite to what one would expect for neutral nanoparticles through the usual depletion mechanism. The effect has been confirmed by independent groups by means of computer simulation [82] and integral equations [69], which showed that a strong repulsion between the "depletant" particles causes the latter to accumulate near the surface of the neutral (or less charged) colloids, thus leading to an effective colloid-colloid *repulsion*. A broader spectrum of possibilities was found by Louis and coworkers [84], who investigated how the effective force between two big colloidal spheres in a sea of smaller spheres depends on the basic big-small and small-small

---

*1266 citing articles in the period 1985-2010, according to the Web of Science® database.

interactions. The latter were taken of the hard-core Yukawa type and several combinations of attraction and repulsion were studied by means of computer simulation and theory. From their work and a closely-related investigation by Egorov [41], the following trends emerge. Adding a colloid-depletant repulsion enhances the depletion attraction among the colloids, since the density of the depletant in the vicinity of the colloids is reduced; the effect is further enhanced by an additional depletant-depletant attraction. Conversely, the presence of a colloid-depletant attraction causes the accumulation of the depletant around the colloids, which in turn makes the colloid-colloid effective force more repulsive; the phenomenon is strongly enhanced by the addition of a depletant-depletant repulsion but, quite surprisingly, also by the addition of a depletant-depletant attraction, which combines with the colloid-depletant attraction to trigger again an increase of the density of the depletant close to the colloids (a phenomenon termed by the authors "repulsion through attraction"). The previous description surely makes clear that the situation is quite involved: the effective force experienced by the colloids depends noticeably on the relative sign and magnitude of the basic interactions.

The investigation presented in this chapter deals with a phenomenon that could instead be described as "attraction through repulsion". In particular, we show that in a binary mixture of hard spheres interacting through repulsive hard-core Yukawa potentials – a model for a colloidal dispersion where both the colloids and the particles of the depletant bear a surface charge of like sign – a substantial enhancement of the depletion attraction over the ideal Asakura-Oosawa picture may result. The main goal is to explain a set of experimental results obtained by Piazza and Buzzaccaro, who actually prompted this work. We start by reviewing the essential features of the experiment, referring the reader interested in the details to the published article [26].

3.1 EXPERIMENTAL EVIDENCE

The measurements were performed on aqueous suspensions of spherical particles made of the Hyflon® MFA fluoropolymer, with an average radius of 90 nm and a polydispersity of about 4%, as ascertained by dynamic light scattering. The surface of MFA latex particles bears a negative charge, mostly due to the to the presence of trapped fluorinated surfactant used in the emulsion polymerization [105] and, possibly, to added ionic stabilizers. Although no detailed proprietary information is released by the producing company, so that a reliable estimate of the amount of charge is not available, the latter is expected to be significant, as is directly witnessed by the high intrinsic stability of the dispersions in the presence of a substantial amount of added salt. Apart from the high intrinsic surface charge, MFA polymer colloids were chosen for their unique material and optical properties, including: (i) a very low average refractive index, which minimizes multiple scattering effects in optical measurements; (ii) a partially crystalline structure, that enables the local particle concentration to be probed accurately through depolarized light scattering; (iii) a high material density, that allows a precise measurement of the particle volume fraction in the suspensions and also makes equilibrium sedimentation experiments much less time-consuming than for other common colloidal latices.

Most of the experiments were performed using as a depletion agent sodium dodecyl sulfate (SDS), a simple anionic surfactant whose physical properties are well known [30]. Beyond a critical micellar concentration that depends on the ionic strength of the solution, SDS forms negatively-charged globular micelles with a pretty constant hydrodynamic radius $a \simeq 2.5$ nm. Their aggregation number, that also corresponds to the structural charge in units of the elementary charge, is around 80-110, vary-
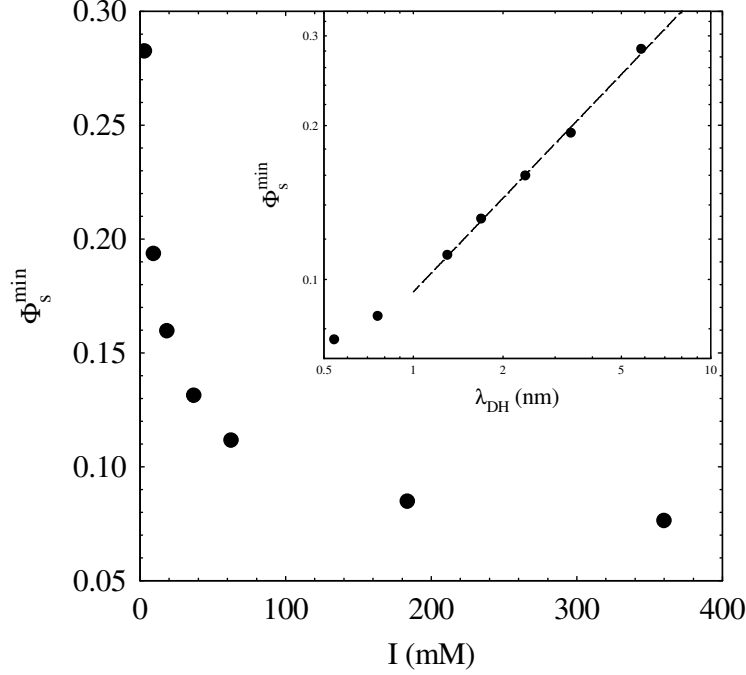
Figure 3.1: Minimum amount of Triton X-100, expressed in terms of the micelle volume fraction Φ_s, required to phase-separate a MFA suspension at a particle volume fraction $\Phi = 0.01$, as a function of the ionic strength I. The same data are plotted as a function of the Debye-Hückel screening length in the double-log inset, with a power law fit. Reproduced from Ref. [26].

ing by no more than 10% in the whole range of experimental conditions sampled. In order to make a connection with the Asakura-Oosawa regime, a limited number of measurements was also performed with sodium dodecyl sulfate replaced by Triton X-100, a widely used *non*-ionic surfactant representing, to a fair approximation, an almost-ideal uncharged depletion agent.

Two classes of measurements, involving different physical processes, were carried out at room temperature: (i) depletion-induced colloid phase separation, and (ii) colloid sedimentation.

In the first series of experiments, upon fixing the colloid volume fraction and the ionic strength of the solution – which sets the amplitude and range of the electrostatic interactions – the concentration of the surfactant was gradually increased until fast aggregation and settling of the colloids took place in the dispersion. The latter was interpreted as a spinodal decomposition triggered by an effective, depletion-induced attraction pushing the colloids together: accordingly, the minimum amount of surfactant necessary for the process to be initiated provides an indirect measure of the efficiency of the attraction. The experiment was repeated varying the ionic strength, so that the dependence of the effective force on the amount of electrostatic coupling in the system could be mapped out. The results obtained using as a depletion agent Triton X-100 and SDS are presented in Figure 3.1 and 3.2, respectively. In order to make a comparison between the two systems, note that the variables labeling the axes of the two figures, although being different, are closely related: the amount of salt appearing on the horizontal axis of Figure 3.2 may be converted to the ionic
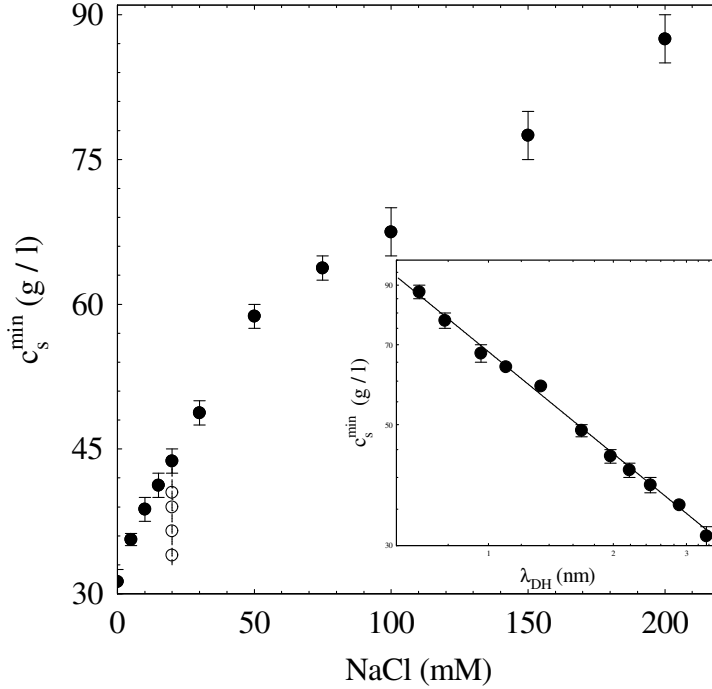
Figure 3.2: Minimum amount of SDS, expressed in terms of the surfactant mass per unit volume c_s, required to phase-separate a MFA suspension at a particle volume fraction $\Phi = 0.02$, as a function of the amount of added NaCl salt. State points where sedimentation profiles have been measured are shown as open dots. The data are plotted in the double-log inset as a function of the Debye-Hückel screening length, with a power-law fit. Reproduced from Ref. [26].

strength, as in Figure 3.1, by simply adding a constant (which is in fact the critical micellar concentration of SDS) accounting for charged surfactant molecules not bound to micelles; likewise, the concentration of SDS expressed in terms of mass per unit volume may be easily converted to micelle volume fraction – the equivalent quantity used for Triton X-100 – by multiplication by a constant (the volume per unit mass of SDS micelles).

In the case of the uncharged depletant (Triton X-100), an increase in the electrostatic coupling, that is a lowering of the ionic strength, merely renders the direct colloid-colloid repulsion longer ranged, while the colloid-surfactant and surfactant-surfactant interactions are unaffected: accordingly, the depletion attraction weakens and a greater amount of surfactant is needed to trigger phase separation. This is just plain common sense. On the contrary, when using as a depletion agent the charged surfactant (SDS), the outcome is precisely reversed: in this case the electrostatic repulsion between each pair of particles in the system enhances the effective attraction experienced by the colloids. This is *not* readily justified with a "back of the envelop" calculation: remember that in the experiments cited earlier in the introduction highly-charged nanoparticles would instead stabilize the suspension against aggregation. This suggests that the end result stems from a delicate balance of the basic interactions in the mixture.

Before turning to the theoretical modelling, we briefly summarize in Figure 3.3
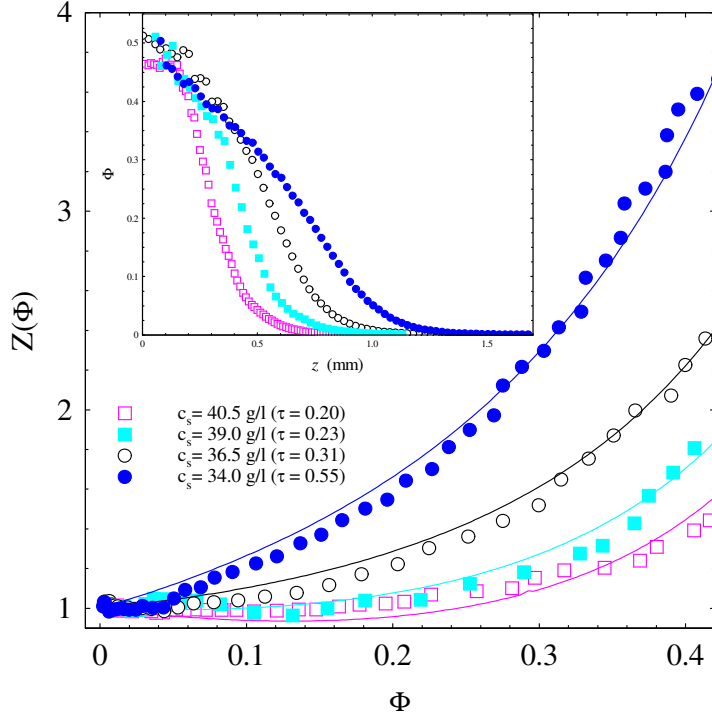
Figure 3.3: Main body: compressibility factor $Z = \beta\Pi/n$ of the colloidal suspension, where Π is the (osmotic) pressure, β the inverse thermal energy and n the number density of the colloids, plotted as a function of the colloid packing fraction Φ. The ionic strength is fixed at 20 mM and several values of the surfactant concentration c_s, corresponding to the four state points along the vertical line in Figure 3.2, are considered. Each curve is fitted by the EOS of the Baxter model [14], and the best fit values of the stickiness parameter τ are given in the legend. The corresponding sedimentation profiles are shown in the inset. Reproduced from Ref. [26].

the second class of experiments performed by Piazza and Buzzaccaro: by measuring with optical techniques the equilibrium sedimentation profile of the dispersion, the full equation of state of the colloidal particles, which provides a more quantitative characterization of the effective interaction, could be computed for a number of selected state points. The data have been fitted with the analytical expression of the equation of state of a system of adhesive hard spheres, derived from the Baxter solution of the Percus-Yevick integral equation by use of the compressibility route ([14], see also Chapter 2). Each curve is labeled by the stickiness parameter τ: we see that this simple model is able to reproduce moderately well the experimental equations of state within the uncertainties of the data. The agreement is however less satisfactory than the one obtained in Ref. [27] in conditions of high salt concentration, probably indicating that in the present case the features of the interparticle interaction potential are only partly captured by the simplified adhesive hard sphere model. The fitted values for τ should then be considered just as indicative; nonetheless, they will be valuable for an assessment of the model that we are about to develop.

3.2 THEORETICAL ANALYSIS

We now attempt an interpretation of the experimental results in the framework of classical statistical mechanics and liquid state theory, starting from a microscopic description of the colloidal suspension. The system is modeled as a binary mixture of charged particles – colloids and micelles – dispersed in an electrolyte. The mixture is then mapped onto a one-component fluid model by defining an effective colloid-colloid interaction mediated by the micelles. This step is accomplished by use of the hypernetted-chain equation from the theory of simple liquids. Finally, the equation of state and phase portrait of the effective one-component fluid are determined and compared with the experimental data.

3.2.1   Electrostatic interactions and model system

We consider a homogeneous dispersion of colloids and micelles in an electrolyte at room temperature. Here and in the following the subscripts b and s will denote quantities related to the colloids (the "big" species) and the micelles (the "small" species) respectively, whereas the Greek indices μ and ν will be used to refer either species. Both the colloids and the micelles are represented as charged hard spherical particles with diameter σ_μ, radius $a_\mu = \sigma_\mu/2$ and number density n_μ carrying a net negative charge $-Z_\mu e$, e being the elementary charge. Considering the colloids as charged hard spheres is a standard procedure, while, within the DLVO picture, the intermicellar interaction should also include dispersion forces. However, according to previous studies [30] induced dipole-dipole forces become relevant only at relatively high ionic strengths: in most of the experimentally investigated range of salt concentration, Coulomb repulsion dominates. Therefore, to minimize the number of parameters in the model, micelles are considered as charged spheres, neglecting dispersion forces.

Electrostatic interactions in colloidal dispersions are deeply affected by screening from mobile charges in the solution, which include: (i) positive and negative ions resulting from the dissolution of a salt of bulk molar concentration c_{salt}; (ii) the critical micellar concentration (cmc) contribution due to free SDS surfactant molecules; (iii) positive counterions released by the colloids and the micelles. In the following we will neglect the colloid counterions because their contribution is always negligible at the concentrations we investigated. The relevant parameter governing the amount of mobile charges is the ionic strength I which, for monovalent ions, is given by (in moles per unit volume)

$$I = c_{\text{salt}} + \text{cmc} + \frac{Z_{\text{s}}^{\text{eff}} n_{\text{s}}}{2 N_{\text{A}}} \,, \tag{3.1}$$

where N_{A} is the Avogadro number and $Z_{\text{s}}^{\text{eff}}$ is the number of *mobile* counterions released by each micelle. The structure of the counterion cloud around a charged particle and the resulting screened Coulomb interaction between two charged spheres in solution is a classical problem of statistical physics [17] which has been studied by several approaches over the years, ranging from numerical simulations, to Poisson-Boltzmann equation or phenomenological approaches. A key quantity characterizing the screening cloud at a surface is the inverse Debye length κ, defined as

$$\kappa = \sqrt{8\pi\, l_{\text{B}} N_{\text{A}} I} \tag{3.2}$$

where is l_{B} the Bjerrum length

$$l_{\text{B}} = \frac{\beta e^2}{\epsilon} \,, \tag{3.3}$$

β is the inverse thermal energy and ϵ is the relative permittivity of the solvent.[†] The extent of screening of a charged sphere of radius a embedded in an electrolyte is then expressed by the dimensionless ratio κa between the sphere radius and the Debye length. In the parameter range of the experiments, this dimensionless quantity is always comparable or larger than unity for both micelles and colloids, showing that the Debye length is the smallest length-scale in our problem.

The electrostatic potential of a single charged particle embedded in an electrolyte is usually expressed in a dimensionless form $\phi(r)$, by use of the thermal potential $1/\beta e$. The geometry of the screening cloud is governed by the Poisson-Boltzmann equation with a boundary condition at the sphere surface defined by the structural charge Z^{str}, quantifying the amount of charge attached to the surface:

$$\left.\frac{d\phi(r)}{dr}\right|_{r=a} = -Z^{\mathrm{str}}\, l_{\mathrm{B}}/a^2 \,. \tag{3.4}$$

For $Z^{\mathrm{str}} \gg 1$ and $\kappa a \gtrsim 1$, the screening cloud is dominated by non-linear effects close to the surface of the sphere: the phenomenon of ion condensation takes place in this region and the running charge quickly drops from the bare value (Z^{str}) to a much smaller limit (Z^{eff}) which depends only on the sphere radius [17]:

$$Z^{\mathrm{eff}} \sim 4\left(\frac{a}{l_B}\right) \,. \tag{3.5}$$

This effective charge therefore represents an estimate of the amount of mobile ions in the screening cloud around the sphere of radius a. Beyond this non-linear region, the solution of the Poisson-Boltzmann equation is well represented by a simple Yukawa form

$$\phi^{\mathrm{DH}}(r) = y\,\frac{\exp[-\kappa(r-a)]}{r/a} \tag{3.6}$$

with an amplitude y weakly depending on the parameter $\kappa a \gtrsim 1$ and approaching $y = 4$ for sufficiently large structural charge: the amplitude y provides the effective surface potential which, in a Debye-Hückel approach, reproduces the asymptotic behavior of the solution to the full Poisson-Boltzmann equation. In Figure 3.4 this distinctive behavior of the counterion cloud is illustrated for a representative choice of the parameters.

The previous discussion on the behavior of the screening cloud suggests that, for high structural charge and $\kappa a \gtrsim 1$, the electrostatic interactions between two spheres at center-to-center distance r can be represented in a simple Debye-Hückel form

$$\beta v^{\mathrm{DH}}(r) = \frac{a}{2l_{\mathrm{B}}}\, y^2\,\frac{\exp[-\kappa(r-\sigma)]}{r/\sigma} \,. \tag{3.7}$$

provided the surface-to-surface distance $r - \sigma$ is larger than the size of the condensed counterionic shell, where non-linear effects prevail. We will therefore model the micelle through a purely repulsive interaction $v_{\mathrm{ss}}(r)$ comprising hard sphere exclusion and Coulomb repulsion, represented in the Yukawa form (3.7). To corroborate this choice, we directly evaluated the electrostatic interaction between two spheres with a uniform charge Z^{str} on their surface, by numerical integration of the Poisson-Boltzmann equation in cylindrical symmetry. The results are shown in the inset of Figure 3.4 for

---

[†]The dielectric permittivity is the only parameter which contains the properties of the solvent, considered as an incompressible continuum medium.
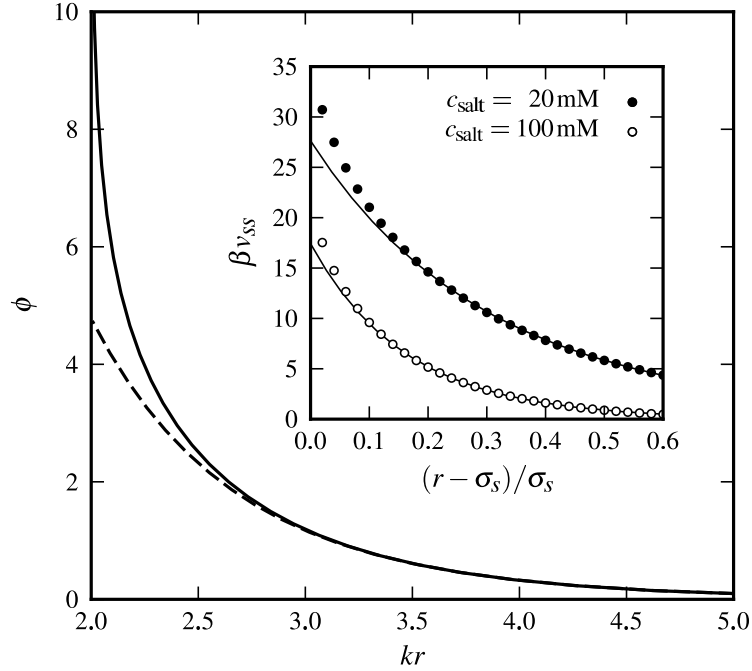
Figure 3.4: Main body: numerical solution of the Poisson Boltzmann equation in spherical symmetry for large structural charge $Z^{\mathrm{str}} \to \infty$ and $\kappa a = 2$ (full line). The Yukawa form (3.6) representing the asymptotic decay at large distances is also shown (dashed line), with an amplitude $y \approx 4.7$; the limiting value $y = 4$ would be approached for $\kappa a \gg 1$. Inset: comparison between the electrostatic interaction between two spheres with radius $a_s = 2.5$ nm and structural charge $Z^{\mathrm{str}} = 80$ obtained by numerical solution of the Poisson-Boltzmann equation (symbols) and the corresponding Yukawa potential (3.7) (full line).

a choice of the parameters appropriate to model SDS micelles in a solution with two different salt concentrations. The effective interaction is well represented by a simple Yukawa form with amplitude y determined by a simple matching condition on the decay of the electrostatic potential of a single sphere given by Equation (3.6).

In order to validate these theoretical expectations, we asked Piazza and Buzzaccaro to perform additional experiments on a solution of SDS micelles alone. Indeed, following the seminal work by Corti and Degiorgio [30], accurate light scattering measurements at low micelle concentration allow one to extract the dimensionless virial coefficient $\bar{B}_2^{\mathrm{s}}$, directly related to the screened intermicellar interaction by

$$\bar{B}_2^{\mathrm{s}} = 12\, \sigma_{\mathrm{s}}^{-3} \int_0^{+\infty} dr\, r^2 \left[1 - \exp\left(-\beta v_{\mathrm{ss}}(r) \right) \right] . \tag{3.8}$$

The experimental data are shown in Figure 3.5 together with previous results available in the literature [30, 136]. To convert the directly accessible SDS weight fraction into a micelle number density, and then to the micelle volume fraction $\Phi_{\mathrm{s}} = \frac{\pi}{6} n_{\mathrm{s}} \sigma_{\mathrm{s}}^3$, it is necessary to estimate the micelle specific volume $\bar{v}$. Neutron scattering data reported in Ref. [24] suggest $\bar{v} \sim 1.5 \pm 0.2$ cm^3/g, which we will consistently adopt
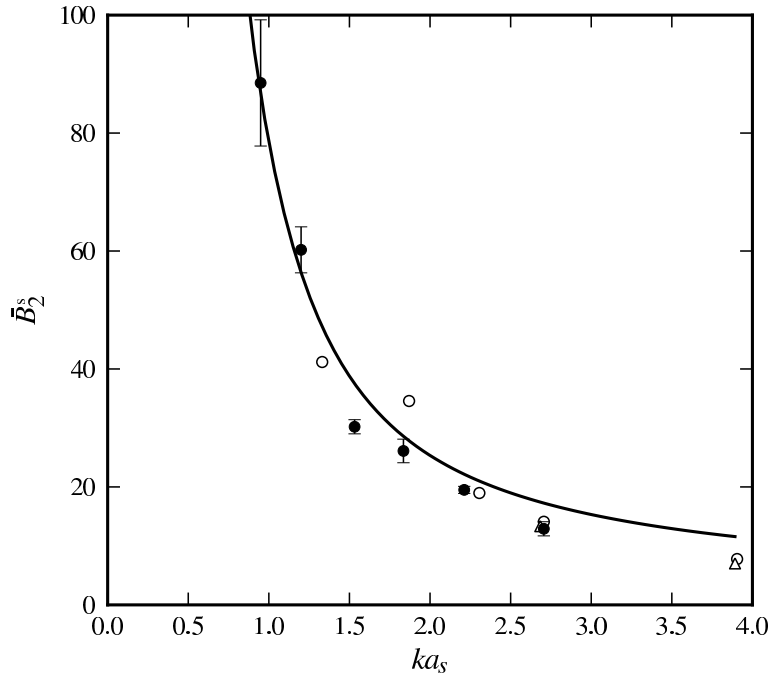
Figure 3.5: Experimentally determined dimensionless virial coefficients of SDS in water solution at different salt concentrations as a function of $\kappa a_{\rm s}$. Full dots: this work; open dots from Ref. [136]; open triangles form Ref. [30]. Theoretical results (full line) obtained via Equation (3.8) by modeling the system as a hard sphere Yukawa fluid. The choice of parameters is discussed in the text.

in the comparison between theoretical results and experiments. The micelle properties entering our model potential (3.7) are just radius and effective surface potential $y_{\rm s}$, which we derive from known properties of SDS micelles in the following way: (i) the aggregation number as a function of the ionic strength is deduced from neutron scattering data [24]; (ii) the structural charge $Z^{\rm str}$ follows directly attributing a single negative charge to each molecule; (iii) numerical integration of the Poisson-Boltzmann equation for each ionic strength provides the parameter $y_{\rm s}$ determining the amplitude of the Debye-Hückel potential (3.7); (iv) the particle radius is assumed to grow with the ionic strength as the cubic root of the aggregation number: this keeps the specific volume $\bar{v}$ constant. The agreement between our simplified theoretical model and different sets of experimental data of Figure 3.5 is rather good except at the highest ionic strengths, where dispersion forces are expected to play a relevant role.

The electrostatic energy of interaction of two colloidal particles, whose radii are much larger than the screening length, is usually modeled within Derjaguin approximation [64, 96] as

$$\beta v_{\rm bb}(r) = \frac{a_{\rm b}}{2l_{\rm B}} \, y_{\rm b}^2 \, \log\left[1 + \exp\left(-\kappa(r - \sigma_{\rm b})\right)\right] \tag{3.9}$$

in the physically accessible region $r > \sigma_{\rm b}$. On the basis of the previously discussed

arguments, we again expect that provided the colloidal charge is high enough, the parameter y_b will be close to its limiting value $y_b \approx 4$.

Finally, the colloid-micelle interaction, besides the exclusion due to the hard cores, is again determined by the geometry of the screening cloud. The resulting repulsive potential turns out to play an important role in the phase diagram of our model: on physical grounds, we expect a strong, almost hard-sphere, Coulomb repulsion at distances of the order of the Debye length, followed by a softer repulsion at larger distances, well represented by a Yukawa form:

$$\beta v_{bs}(h) = \frac{a_b a_s}{l_B} \, y_b y_s \, \frac{\exp(-\kappa h)}{a_b + a_s + h} \,, \qquad h \doteq r - a_b - a_s \,, \tag{3.10}$$

where h is the distance between the surfaces of the two particles. An analytical expression embodying both the strong short range repulsion at $h \lesssim \kappa^{-1}$ and the Yukawa tail is provided by the Hogg-Healy-Fuerstenau form [61] giving the electrostatic energy of interaction of two particles with different radii at constant surface charge:

$$\beta v_{bs}(h) = \frac{a_b \, a_s}{4 l_B (a_b + a_s + h)} \left[4 y_b y_s \, \mathrm{atanh}(e^{-\kappa h}) - (y_b^2 + y_s^2) \log \left(1 - e^{-2\kappa h} \right) \right] \,. \tag{3.11}$$

It should be stressed that the model we are considering is not intended as a fully quantitative description of the physical system, due to the crude representation of the colloid-micelle suspension as a mixture of charged hard spheres and to the adopted approximation in the description of the screening effects. Nevertheless, we expect that this theoretical framework is able to capture the essential nature of the interactions and to reproduce the key features seen in the experiments.

3.2.2 Generalities on effective interactions

When dealing with mixtures whose components are very asymmetric in size, it is customary to map the system onto an equivalent one-component fluid, which is often far easier to deal with, comprising particles of the larger species interacting via an effective potential accounting for the indirect contributions from the neglected components. The reduction of a binary mixture to a one-component system is performed by a partial trace in phase space over the degrees of freedom of the particles belonging to the smaller species. More precisely, let H be the configurational energy of the mixture:

$$H(\boldsymbol{R}, \boldsymbol{r}) = H_{bb}(\boldsymbol{R}) + H_{ss}(\boldsymbol{r}) + H_{bs}(\boldsymbol{R}, \boldsymbol{r}) \,, \tag{3.12}$$

where $\boldsymbol{R} = \{R_i\}_{i=1\ldots N_b}$ and $\boldsymbol{r} = \{r_i\}_{i=1\ldots N_s}$ are the set of coordinates of the big and the small particles respectively, and the interactions are assumed as pairwise additive:

$$H_{bb}(\boldsymbol{R}) = \sum_{i<j}^{N_b} v_{bb}(|R_i - R_j|) \,, \tag{3.13a}$$

$$H_{ss}(\boldsymbol{r}) = \sum_{i<j}^{N_s} v_{ss}(|r_i - r_j|) \,, \tag{3.13b}$$

$$H_{bs}(\boldsymbol{R}, \boldsymbol{r}) = \sum_{i=1}^{N_b} \sum_{j=1}^{N_s} v_{bs}(|R_i - r_j|) \,. \tag{3.13c}$$

In the semi-grand ensemble, where the number N_b of the big particles and the fugacity z_s of the small particles are fixed, the free energy is expressed as

$$\exp[-\beta F(N_b, z_s, V)] = \mathrm{Tr}_{\boldsymbol{R}, \boldsymbol{r}} \exp[-\beta H] \,, \tag{3.14}$$

where V is the volume of the system, the temperature dependence is implied and the trace denotes the statistical average appropriate for the ensemble. By partitioning the trace over the degrees of freedom of the two species the free energy can be written as:

$$\exp[-\beta F] = \mathrm{Tr}_{\boldsymbol{R}} \exp[-\beta H^{\mathrm{eff}}] \,, \tag{3.15}$$

where H^{eff} is an effective Hamiltonian depending on the coordinates of the big particles alone. It comprises the sum of two terms:

$$H^{\mathrm{eff}} = H_{\mathrm{bb}} + \Omega(N_{\mathrm{b}}, z_{\mathrm{s}}, V; \boldsymbol{R}) \,, \tag{3.16}$$

the first accounting for the direct interactions, the second being the thermodynamic potential of a fluid of small particles in the external field imposed by a fixed configuration of the big ones:

$$\exp[-\beta \Omega] = \mathrm{Tr}_{\boldsymbol{r}} \exp[-\beta(H_{\mathrm{ss}} + H_{\mathrm{bs}})] \,. \tag{3.17}$$

It has been shown [37, 38, 39] that the potential Ω can be decomposed in a series of n-body terms $w^{(i)}$, so that the effective Hamiltonian takes the following form:

$$
\begin{aligned}
H^{\mathrm{eff}} = {} & H^{(0)}(N_{\mathrm{b}}, z_{\mathrm{s}}, V) + \sum_{i<j}^{N_{\mathrm{b}}} \left[v_{\mathrm{bb}}(R_{ij}) + w^{(2)}(R_{ij}; z_{\mathrm{s}}) \right] \\
& + \sum_{i<j<k}^{N_{\mathrm{b}}} w^{(3)}(R_{ijk}; z_{\mathrm{s}}) + \dots
\end{aligned}
\tag{3.18}
$$

where R_{ij} and R_{ijk} denote sets of two and three coordinates respectively. $H^{(0)}$ is called the volume term and accounts for that part of the free energy of the small particles which does not depend on the position of the big ones. The pair term is the sum of the direct potential v_{bb} and the indirect contribution $w^{(2)}$ induced by the small spheres. Three-body and higher order terms are of indirect origin and entirely due to the species integrated out; in many cases, especially when the asymmetry between the two components is very large, they can be neglected to a good approximation [83]. The volume term is often neglected as well, since it has a simple form linear in the volume and in the number of big particles resulting in innocuous shifts in the pressure and chemical potential which do not affect phase behavior [39].

The one-component fluid with Hamiltonian H^{eff} and the original mixture share the same structure, as far as correlations between the big particles are concerned. For example, $S(k) = S_{\mathrm{bb}}(k)$, where the first is the structure factor of the one-component system, whereas the second is the analogous quantity in the mixture. Thermodynamic properties are preserved as well, so that any instability in the mixture shows up in the one-component picture too. These are the main points justifying the approach based on effective interactions.

3.2.3 Effective potential from HNC equations: method and validation

Determination of the effective potential by direct computation of the partition sum in Equation (3.17) is often not viable; a common alternative is to obtain the free energy of the small particles at fixed configuration of the big ones, possibly with a certain degree of approximation, using other tools such as density functional theory or perturbation theory. Here we employ an approach based on integral equations from the theory of simple liquids leading directly to the pair term of the effective potential.

It is known that in a homogeneous one-component fluid the zero density limit of the radial distribution function equals the Boltzmann factor of the two-body term in the interaction potential [57]; the same property holds in the mixture:

$$
\begin{aligned}
\lim_{n_{\mathrm{b}}\to 0} g_{\mathrm{bb}}(r; n_{\mathrm{b}}, z_{\mathrm{s}}) &= \exp\{-\beta[v_{\mathrm{bb}}(r) + w^{(2)}(r; z_{\mathrm{s}})]\} \\
&\doteq \exp[-\beta V^{\mathrm{eff}}(r; z_{\mathrm{s}})]\,,
\end{aligned}
\tag{3.19}
$$

where g_{bb} is the radial distribution function of the large particles and we defined V^{eff} as the two-body term of the effective potential. Thus, the latter is known once the correlations between the particles in the mixture are calculated at the pair level. To obtain the correlations, we consider the Ornstein-Zernike relations for the mixture [57] in the limit of vanishing density of the large particles:

$$
h_{\mathrm{ss}}(r) = c_{\mathrm{ss}}(r) + n_{\mathrm{s}}^r\,[c_{\mathrm{ss}} * h_{\mathrm{ss}}](r)\,,
\tag{3.20a}
$$

$$
h_{\mathrm{bs}}(r) = c_{\mathrm{bs}}(r) + n_{\mathrm{s}}^r\,[c_{\mathrm{bs}} * h_{\mathrm{ss}}](r)\,,
\tag{3.20b}
$$

$$
h_{\mathrm{bb}}(r) = c_{\mathrm{bb}}(r) + n_{\mathrm{s}}^r\,[c_{\mathrm{bs}} * h_{\mathrm{bs}}](r)\,;
\tag{3.20c}
$$

here, $h_{\mu\nu} = g_{\mu\nu} - 1$ and $c_{\mu\nu}$ are the sets of total and direct correlation functions, the symbol $*$ denotes the three-dimensional product of convolution and n_{s}^r is the so-called reservoir density of the small particles, defined as the density of particles in a system comprising the small species alone in osmotic equilibrium with the mixture at a given composition.

Let us briefly discuss the role of the reservoir. In real experiments, it is natural to fix the composition of the mixture, specifying both densities n_{b} and n_{s}. This means that, in the semi-grand ensemble (3.14), the fugacity z_{s} of the small species has to be chosen so that the mean number density of particles equals the experimental value. From standard thermodynamics, the connection between the two quantities is

$$
n_{\mathrm{s}}(z_{\mathrm{s}}, n_{\mathrm{b}}) = -\frac{z_{\mathrm{s}}}{V}\frac{\partial \beta F}{\partial z_{\mathrm{s}}}\,.
\tag{3.21}
$$

The limiting procedure in Equation (3.19) is carried out at fixed fugacity of the small particles; consequently, the density appearing in the Ornstein-Zernike relations (3.20) corresponds to the prescribed fugacity in the absence of large particles:

$$
n_{\mathrm{s}}^r(z_{\mathrm{s}}) = \lim_{n_{\mathrm{b}}\to 0} n_{\mathrm{s}}(z_{\mathrm{s}}, n_{\mathrm{b}})\,.
\tag{3.22}
$$

This is the definition of the reservoir density. The exact relation between n_{s} and n_{s}^r is nontrivial, as manifest from Equation (3.21); however, an asymptotic result can be derived:

$$
\frac{n_{\mathrm{s}}}{n_{\mathrm{s}}^r} = 1 + O(n_{\mathrm{b}}\sigma_{\mathrm{b}}^3)\,,
\tag{3.23}
$$

so that in the regime of low volume fraction of the large particles ($\Phi_{\mathrm{b}} = \frac{\pi}{6} n_{\mathrm{b}}\sigma_{\mathrm{b}}^3$) the two quantities are nearly equal. In all the experiments performed by Piazza and Buzzaccaro involving depletion-induced colloid aggregation – whose results are displayed in Figures 3.1 and 3.2 – the volume fraction of the colloids never exceeds 0.02: accordingly, in the following we will neglect the correction terms and directly compare the actual, experimentally-measured micelle density to the small-sphere reservoir density entering the Ornstein-Zernike equations.
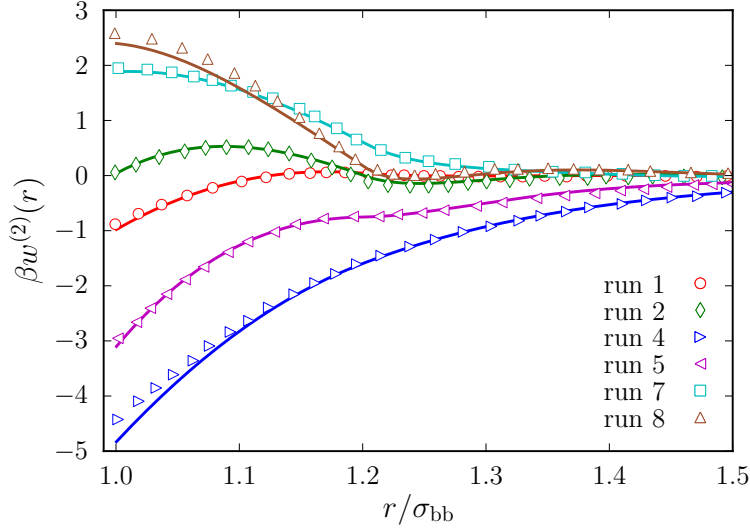
Figure 3.6: Comparison of the effective potential as computed from the HNC equations and simulation data from Ref. [84]. Big particles behave as hard spheres with diameter σ_{bb}, whereas b-s and s-s pair interactions have a hard-core Yukawa form with contact values $\epsilon_{\mu\nu}$, hard-core diameters $\sigma_{\mu\nu}$ and inverse decay lengths $\kappa_{\mu\nu}$. The strengths of the Yukawas are varied across the various runs (for details see the reference); the other parameters are fixed as follows: $\sigma_{ss} = \sigma_{bb}/5$, $\sigma_{bs} = (\sigma_{bb} + \sigma_{ss})/2$, $\kappa_{ss} = 15/\sigma_{bb}$ and $\kappa_{bs} = 6/\sigma_{bb}$; the packing fraction of the small particles is $\Phi_s = 0.1$. The symbols denote simulation data, whereas the lines are the results of HNC calculations.

We supplement the Ornstein-Zernike equations (3.20) with the hypernetted-chain (HNC) closure [57]:

$$\log g_{\mu\nu}(r) = -\beta v_{\mu\nu}(r) + h_{\mu\nu}(r) - c_{\mu\nu}(r). \tag{3.24}$$

The procedure to compute the pair term of the effective potential can be summarized as follows: (i) first, equation (3.20a) is solved, together with its closure, to obtain the correlation function h_{ss} of the small particles alone; (ii) the result is then inserted into Equation (3.20b) to get the mixed correlation functions h_{bs} and c_{bs}; (iii) finally, the sought-for quantity $w^{(2)}$ follows from Equations (3.20c), (3.19) and (3.24):

$$-\beta w^{(2)}(r; z_s) = n_s^r(z_s) [c_{bs} * h_{bs}](r). \tag{3.25}$$

Equations (3.20a) and (3.20b) are solved numerically by means of a simple iterative scheme [94], and convolutions are computed in Fourier space using a FFT algorithm.

To validate the method, we compare in Figure 3.6 the pair term of the effective potential as obtained from simulations in Ref. [84] with the results of HNC calculations: the agreement is good, especially when both small-small and big-small interactions are repulsive (as in the case of interest).

3.2.4   Thermodynamic properties and phase behavior of the dispersion

Once the term $w^{(2)}$ is known, the effective pair potential V^{eff} – which depends parametrically on the small-sphere reservoir density n_s^r through the fugacity z_s – can be

computed by means of Equation (3.19). Then, the thermodynamic properties of the equivalent fluid comprising the big particles alone can be obtained. When dealing with short-ranged interactions in colloidal systems, the Noro-Frenkel extended law of corresponding states is usually invoked: the compressibility factor is a universal function of the reduced temperature, density and of the reduced second virial coefficient $\bar{B}_2^{\mathrm{b}}$, but is largely independent of the specific shape of the potential [95]. Thus, the properties of the system of interest can be mapped onto those of an adhesive hard sphere fluid with a stickiness parameter τ corresponding to the given $\bar{B}_2^{\mathrm{b}}$ [14]. As may be recalled from Chapter 2, values of τ close to zero signal strong adhesion between the big particles, whereas large values point out a behavior akin to hard spheres. The reduced second virial coefficient of the big particles and the stickiness parameter are defined by (see also Equation (2.2)):

$$\bar{B}_2^{\mathrm{b}} = 12\,\sigma_{\mathrm{b}}^{-3} \int_0^{+\infty} dr\, r^2 \left\{ 1 - \exp\left[-\beta V^{\mathrm{eff}}(r; n_{\mathrm{s}}^r) \right] \right\} ; \tag{3.26}$$

$$\tau = \frac{1}{4 - \bar{B}_2^{\mathrm{b}}} . \tag{3.27}$$

The adhesive hard sphere model has been extensively investigated in the past and its phase diagram is by now well known leading, via the Noro-Frenkel scaling, to a simple way to investigate the thermodynamic properties of this class of systems.

If the experimentally observed aggregation of the colloidal particles is interpreted as a thermodynamic instability driven by the divergence of the isothermal compressibility, then the experimental transition points shown in Figures 3.1 and 3.2 should correspond to the spinodal boundary at the given colloid volume fraction ($\Phi_{\mathrm{b}} = 0.01$ in the former case, $\Phi_{\mathrm{b}} = 0.02$ in the latter). As may be recalled by looking at Figure 2.1, in the adhesive hard sphere model points of the spinodal line at such a low density have not been directly investigated by numerical methods, while analytical approximations, like the Percus-Yevick solution, are not reliable. However, by extrapolating the Monte Carlo simulation data in Ref. [91] we can approximately locate the transition points at a stickiness parameter in the range $(0.04 - 0.08)$.

3.2.5   Comparison with experimental data

We now turn to the evaluation of the effective colloid-colloid interaction which originates within the model discussed in Section 3.2.1, and make connection with the experiments. Since depletion effects in interacting mixtures have been already considered in other systems, as described in the introduction of the chapter, let us start by pointing out a number of differences between the present case and the works previously cited: (i) in Refs. [84, 82, 69] the big particles behave as pure hard spheres, whereas here an additional electrostatic repulsion is considered; (ii) the big-small interaction in the present model is repulsive, while in Ref. [82] is taken as attractive; (iii) in contrast with Refs. [84, 69], the amplitudes of the bare interactions cannot be varied independently in our model, since they exhibit a mutual dependence on the set of parameters.

We first consider the case of vanishing charge of the depletant, appropriate for describing charged MFA colloids in non-ionic surfactant, for which the experimental results depicted in Figure 3.1 apply. Due to the uncertainties in the modeling of the interactions between Triton micelles, we limit our investigation to the simplest case of ideal depletant, by neglecting excluded-volume and dispersion forces among the small particles. Thus, the effective interaction equals the sum of an attractive, salt-independent Asakura-Oosawa term and the repulsive screened potential (3.9); the
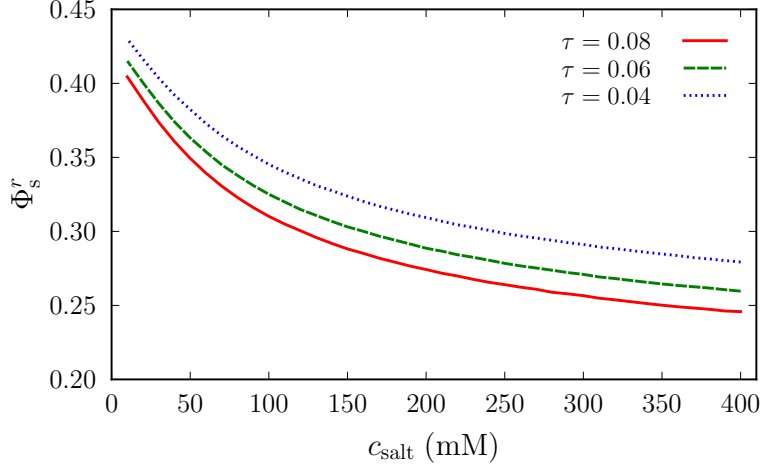
Figure 3.7: Reservoir density of an ideal depletant required to induce an effective colloid-colloid interaction with a prescribed stickiness parameter τ (see Eq. (3.27)) as a function of salt concentration. The parameters are fixed as follows: $\sigma_{\mathrm{b}} = 180\,\mathrm{nm}$, $a_{\mathrm{s}} = 4.2\,\mathrm{nm}$, $y_{\mathrm{b}} = 0.4$ in order to mimic the MFA-Triton system whose phase behavior is depicted in Figure 3.1, although we do not attempt a quantitative interpretation of experimental data.

amount of surfactant required to drive phase separation is expected to rise as the salt concentration is lowered, as clearly seen in the experiments. This behavior is indeed consistently reproduced in the simple AO/Coulomb system, as shown in Figure 3.7. We stress that this minimal model is intended merely as an exemplification of the simple and intuitive features of the effective potential in the presence of the uncharged depletant: we do not attempt any quantitative interpretation of the experimental data. The remainder of the discussion will instead focus on a more thorough analysis of the unexpected features brought about by the *charged* depletant.

We thus turn to the model relevant for MFA colloids in the presence of SDS ionic depletant. In Figure 3.8 we show how the effective interaction is affected by the surface potential y_{s} of the small particles, for a fixed choice of the other parameters. When y_{s} is small, the interaction has a weak attractive well, while at small distances the direct Coulomb repulsion between the colloids prevails.[‡] As y_{s} is increased, several features appear: (i) the effective potential becomes more and more attractive, witnessing strong adhesion of the colloids; (ii) a repulsive barrier, whose height increases with the charge, develops in correspondence to higher values of the separation between the particles; (iii) secondary maxima and minima appear for even larger distances. The deepening of the attractive well can be understood in a naive mechanical picture of the depletion mechanism: once two big particles are close enough, the pressure exerted by the sea of small particles, increasing with the charge, has to be overcome for them to be pulled apart. The growth of the barrier is due to an increase in correlations between the two species, as can be appreciated by looking at the mixed pair distribution function in the inset of the figure: if the charge of the small particles is raised, they accumulate more and more in the proximity of the big ones; since the overlapping of such charged clouds costs energy, the approach of two big particles is disfavored. This behavior

---

[‡]Even if the particles have a hard core, we do not see the oscillatory behavior typical of hard-sphere mixtures since the packing fraction of the depletant is low.
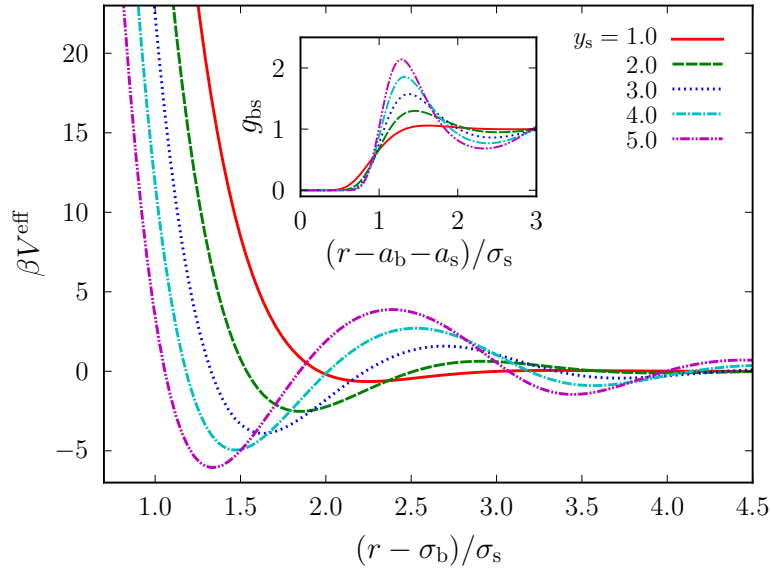
Figure 3.8: Effective colloid-colloid interaction for different surface potential of the small particles, the other parameters being fixed at $a_s = 2.5$ nm, $c_{\text{salt}} = 20$ mM, $y_b = 4$, $\Phi_s^r = 0.05$. Distances are expressed in units of the diameter of the small particles. In the inset, the big-small pair distribution function is shown.

has already been described in the literature: it is termed "accumulation repulsion" in Ref. [84] and "nanoparticle haloing" in Refs. [137, 82, 69]. Our results confirm the previous observations and provide an independent evidence for the phenomenon. In the present case the accumulation takes place at a certain distance from the surface of the big particles and not right at contact: this is due to the unbound character of the potential (3.11), which prevents the touching of a big particle with a small one. We performed analogous calculations replacing the potential with a simple hard-core Yukawa having finite value at contact: in that case, accumulation happened right on the surface of the big particles and the repulsive barrier shifted towards contact as well, in agreement with Ref. [84].

In Figure 3.9 the dependence of the stickiness parameter of the effective potential on the ionic strength of the solution and on the density of the small particles is shown. To correctly evaluate the ionic strength, according to Equation (3.1), we included the contribution due to the counterions released by the micelles by use of Equation (3.5) to estimate the number of counterion per micelle. Lowering the salt concentration, the bare electrostatic interactions become longer-ranged and the effective potential becomes more attractive, leading to a smaller τ: this trend is consistently seen in the investigated range of parameter space. The plot in Figure 3.9 also shows that, at fixed ionic strength, raising the volume fraction of the small particles always causes the effective potential to become more attractive[§]: as before, this agrees with the experimental evidence. By using the previously discussed value $\bar{v} = 1.5$ cm^3/g for the

---

[§]This remains true until a high-concentration regime is entered, not depicted in the figure nor sampled in the experiments, where the trend reverses due to correlation and packing effects of the small particles.
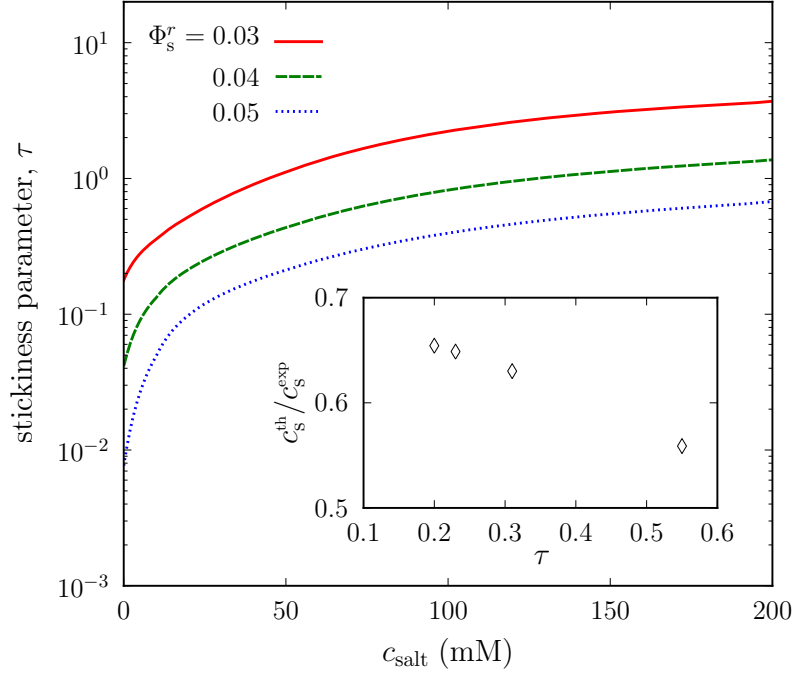
Figure 3.9: Stickiness parameter τ of the effective colloidal one-component fluid as a function of the ionic strength of the solution at several volume fractions of the small particles. The inset shows the ratio between the theoretical estimate c_s^{th} and the experimental c_s^{exp} surfactant concentration corresponding to a given τ. Details in the text.

specific volume of SDS micelles, we can directly compare these results with the experimentally determined equations of state of Figure 3.3. The curves shown in Figure 3.9 provide the "theoretical" micelle concentration c_s^{th} corresponding to a given value of the stickiness parameter τ. In the inset we plot the ratio between this estimate, which follows from the analytical representation of the effective interaction between colloids mediated by the micelles, and the experimental concentration c_s^{exp} appearing in Figure 3.3. It is apparent that the theoretical estimates consistently underestimate the experimental results. The discrepancy may be partly attributed to the approximate representation of the experimental equations of state by the Baxter form: as already pointed out, the data shown in Figure 3.3 suggest that the equation of state cannot be accurately represented in terms of an adhesive hard sphere model. However, to obtain a fully satisfactory agreement, we should also improve our modeling of electrostatic effects, particularly when strong asymmetries both in size and charge are present in the system.

The dependence of τ on the physically accessible quantities (c_{salt}, c_s) has been evaluated from our effective colloid potential via Equation (3.27) at different ionic strengths and surfactant concentrations. The results of the predicted transition line, evaluated for $\tau = 0.02$ and $\tau = 0.04$, are shown in Figure 3.10 together with the experimental data of Figure 3.2. While the behavior at low ionic strengths is well reproduced, the theoretical curve seems to saturate before the experimental data at
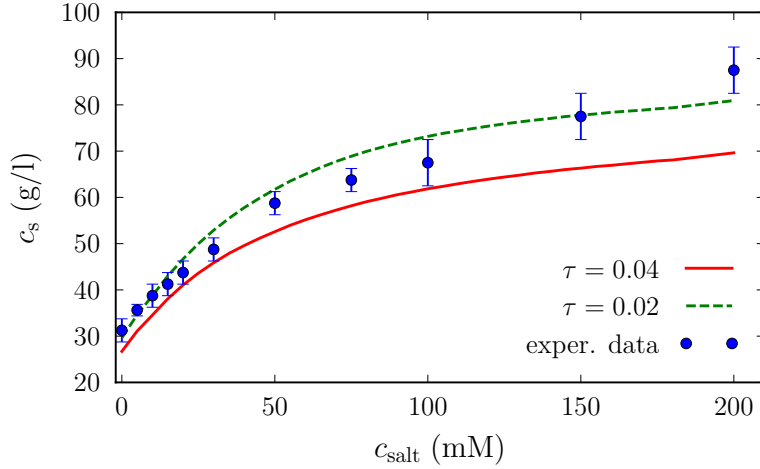
Figure 3.10: Comparison between the experimental transition line and the loci of diverging compressibility from the mapping onto the Baxter model. The SDS concentration beyond which the colloids aggregate is shown as a function of the amount of salt added to the dispersion. The two curves correspond to to different values of the critical τ in the Baxter model.

high salt concentration[¶] and, consistently with the previous analysis of the equation of state, our model overestimates the attraction between colloids. Due to the uncertainties in the parameters and the gross simplifications of the adopted model only a semi-quantitative agreement can be obtained. However, the experimentally observed trend is clearly present also in our model which in fact displays an enhanced tendency towards colloid aggregation when the electrostatic repulsion is poorly screened, that is at low ionic strength. This behavior is indeed robust and does not depend on the fine tuning of the model parameters.

3.3 CONCLUSIONS

The experiments performed by Piazza and Buzzaccaro and their theoretical interpretation presented in this chapter display new and unexpected features in the phase diagrams of colloidal suspensions in the presence of an interacting depletant. In charged surfactants, the repulsive potential can be modified by the addition of salt whose role is to screen the structural charge of the surfactant. The Coulomb interaction gives rise to a larger pressure in the micellar solution but, at the same time, favors the accumulation of micelles near the colloids, leading to increasing correlations and then to more structured effective colloid-colloid interactions. In the region of parameter space experimentally investigated, the net result is an enhanced depletion force, whereby a small amount of surfactant is able to trigger instability among colloids leading to particle phase separation. An accurate modeling of the colloidal suspension should include many physico-chemical details which affect both micelle-micelle and micelle-colloid interactions. However, an extremely simple model including only electrostatic effects allows to reproduce the experimentally observed trends. A consistent

---

[¶]Dispersion forces between SDS micelles, which have been neglected, may play a role in this regime.

semi-quantitative interpretation of the virial coefficients, the equations of state and of the transition points as a function on the ionic strength can be achieved, with no fitting parameters, by requiring a large structural charge on the colloids. The competition between screened Coulomb repulsion and depletion attraction leads to smooth effective colloid-colloid interactions depending quite sensitively on variations in the electrolyte properties. By tuning the ionic strength, it is then possible to enhance or inhibit colloidal aggregation, leading to a direct way to tailor phase diagrams of colloidal suspensions.

4

On the Continuity between the Depletion Interaction and the Critical Casimir Effect

ABSTRACT

We develop a theoretical framework that aims to describe on a common basis the depletion interaction and the critical Casimir effect. Using the methods of density functional theory we derive a formally exact expression for the energy of interaction of two parallel walls immersed in a fluid with arbitrary interparticle interactions. Our result holds even in the neighbourhood of a critical point of the fluid, where the latter is strongly correlated. The density functional approach is already known to give accurate results when applied to the class of the depletion interactions. By performing a long-wavelength analysis of the density fluctuations and using a scaling form of the free energy of the fluid in the critical region, we show that it also accounts quantitatively for the scaling behavior of the critical Casimir force that is usually derived along the critical isochore by means of field-theoretical methods; as a bonus, we are able to compute the scaling behavior off the critical isochore as well. We argue that depletion-induced and critical-Casimir forces have a common origin and merge continuously as the thermodynamic state of the host fluid is varied. Experimental evidence supports our findings.

T HE main characters in this chapter are the depletion interaction and the critical Casimir force. The former is surely familiar, since it formed the subject of most of the previous discussion. The latter, on the contrary, was barely mentioned in the prologue and thus deserves a brief introduction.

The critical Casimir force belongs to the class of fluctuation-induced phenomena, the most famous of which is arguably the quantum-electrodynamical Casimir-Polder force [29] first predicted in 1948. In this well-known example two parallel, uncharged, conducting plates are pushed together by an attractive force arising from the confinement of the quantum vacuum fluctuations of the electromagnetic field. But fluctuations are not a prerogative of quantum field theory: according to statistical physics any condensed-matter system, for instance a fluid, is perpetually affected by the thermal agitation brought about by the atomic and molecular motion. As a consequence, the properties of the fluid – let us think about the density just to clarify things – fluctuate in space and time. The length scale of the spatial fluctuations, namely the correlation length ξ, is usually in the order of the molecular diameter σ, hence extremely small if compared to the extent of a macroscopic sample. Any fluctuation-induced effect is bound to the same scale and disappears at larger ones; in addition, as long as $\xi \sim \sigma$, one expects the effect to depend heavily on the details of the intermolecular interaction.

However, there are cases in which the fluctuations become relevant and detectable even at scales much larger then the molecular one. For instance, if the fluid has a critical point associated with a second-order phase transition, then as the latter is approached a collective behavior emerges which causes the system to become correlated over a macroscopic length scale. Moreover, as the correlation length grows much larger than the molecular diameter, the thermodynamic properties of the system free themselves from the details of the microscopic interaction. This leads to the concept of *universality*, which is undoubtedly the cornerstone of the theory of critical phenomena [131]. For example, in all systems belonging to the three-dimensional Ising universality class, including most classical fluids, the correlation length diverges as the critical temperature T_{c} is approached (along the critical isochore) according to the very same power law

$$\xi \sim \xi_0 \left| 1 - T/T_{\mathrm{c}} \right|^{-\nu} , \tag{4.1}$$

where $\nu \approx 0.63$ is a so-called critical exponent characterizing the scaling behavior of the class and ξ_0 a non-universal amplitude. The physical quantity whose fluctuations are magnified upon approaching the critical point might differ from system to system and is properly called the *order parameter*. We will later base our discussion on a fluid undergoing a liquid-vapor phase transition, for which the order parameter is the particle density.

The previous remarks suggest that any force arising from the confinement of thermal fluctuations in a fluid – a phenomenon also named after Casimir due to its connection with the electrodynamical effect – despite being usually negligible in non-critical conditions, may become not only relevant, but also universal as the critical regime is entered. Indeed, a pair of plates placed a distance h apart inside a fluid are subject to a fluctuation-induced force per unit area F that, provided $\xi, h \gg \sigma$, adheres to the general law

$$F(h) = \frac{k_{\mathrm{B}} T}{h^3} \, \Theta(h/\xi) , \tag{4.2}$$

where k_{B} is Boltzmann's constant, T is the temperature and $\Theta(\cdot)$ is the so-called scaling function for the critical Casimir effect in planar geometry [59]. This function

is universal in the sense that it depends only on certain gross features of the boundary conditions imposed by the plates.

Depletion interactions and fluctuation-induced forces are generally believed to bear little relation to one another and, as such, they are approached with quite different methods. In the former case microscopic models and liquid state theories, either based on distribution functions or density functionals, are employed. In the latter case the approach is often more abstract. Indeed, the general form (4.2) was first derived in 1978 by Michael Fisher and Pierre Gilles de Gennes using finite-size scaling arguments [47]. Moreover, the calculation of the scaling function is usually done, by virtue of the universality property, with reference to a fictitious three-dimensional Ising model using either field-theoretical methods [75] or Monte Carlo simulations [139, 140]. This situation is sort of odd, since both interactions are in the end solvent-mediated effects issuing from the confining of a fluid between two surfaces. Therefore, we believe that the critical Casimir effect can be fruitfully described using the same microscopic approach usually employed when dealing with the depletion interaction. What is more, we believe that the Casimir effect is just a kind of depletion "gone critical". We now embark in the search for a common description of the two effects.

4.1 MECHANICAL PRELUDE

We consider a pair of parallel, infinite plates (or walls, we will use the two terms interchangeably) placed a distance h apart inside a generic fluid made up of particles with diameter σ. Due to symmetry reasons, the situation is effectively one-dimensional: the only relevant direction is the one orthogonal to the plates, that will be taken as the z axis. The origin is fixed at the midpoint between the two plates, so that they are positioned at $z = \pm h/2$. For the plates to have any detectable effect on the fluid (and *viceversa*) an interaction between each plate and a generic particle in the fluid, depending on the distance d of the particle from the plate, must exist. We denote by $w_{\mathrm{L}}(d)$ and $w_{\mathrm{R}}(d)$ the interaction with the left and right wall respectively, and we assume for convenience that they are both even, continuous and differentiable; apart from that, they can be rather different, so that we do not impose any left-right symmetry to the problem. The total external potential acting on a generic fluid particle is then

$$\phi_h(z) = w_{\mathrm{L}}\left(z + \frac{h}{2}\right) + w_{\mathrm{R}}\left(z - \frac{h}{2}\right), \tag{4.3}$$

where the subscript emphasizes that it depends parametrically on the position of the plates. The wall-particle interaction will be taken as short-ranged:

$$w_{\mathrm{L,R}}(d) = 0, \quad |d| > d_0, \tag{4.4}$$

with a range d_0 in the order of the particle diameter σ; this is indeed reasonable if the two plates do not bear a net electric charge. Moreover, we assume that the distance between the plates is such that no particle feels the presence of both at the same time:

$$h > 2d_0 \sim \sigma. \tag{4.5}$$

This requirement, on the contrary, has no particular physical significance: it is merely a matter of convenience, since it simplifies considerably the expressions later to be derived. Note, however, that as a consequence our results, even before any approximation is made, will not formally hold for distances between the plates comparable

with or smaller than the size of a fluid particle. This might seem a serious drawback, since depletion forces are especially relevant at such length scales. However, the flaw is readily amended: it is well known that the methods we are going to use, based on microscopic density functionals, are apt to describe accurately the plate-plate effective interaction even in the regime $h \lesssim \sigma$ [121]. Since we focus instead on showing that by the same methods the scaling form of the long-range, critical Casimir force is also recovered, we willingly trade the validity of the theory in the aforementioned interval in favor of an overall-gained simplicity. If this is done, the external potential (4.3) acting on the particles separates as

$$\phi_h(z) = \begin{cases} w_{\mathrm{L}}\left(z + \frac{h}{2}\right) & z < 0\,, \\ w_{\mathrm{R}}\left(z - \frac{h}{2}\right) & z > 0\,. \end{cases} \tag{4.6}$$

The force experienced by the two walls is readily found by a simple mechanical argument. A generic fluid particle i, with a plate-orthogonal position z_i, exerts on either wall an instantaneous force

$$\mathfrak{f}_i^{\mathrm{L}} = w_{\mathrm{L}}'\left(z_i + \frac{h}{2}\right)\,, \qquad \mathfrak{f}_i^{\mathrm{R}} = w_{\mathrm{R}}'\left(z_i - \frac{h}{2}\right)\,, \tag{4.7}$$

where the prime denotes differentiation with respect to the spatial coordinate. Hence, the total average forces per unit surface F_{L} and F_{R} acting on the left and right wall respectively are

$$F_{\mathrm{L}}(h) = \int_{-\infty}^{0} dz\, \rho_h(z)\, w_{\mathrm{L}}'\left(z + \frac{h}{2}\right)\,, \tag{4.8a}$$

$$F_{\mathrm{R}}(h) = \int_{0}^{+\infty} dz\, \rho_h(z)\, w_{\mathrm{R}}'\left(z - \frac{h}{2}\right)\,, \tag{4.8b}$$

where $\rho_h(z)$ is the equilibrium, statistically-averaged number density of the fluid particles. The condition of macroscopic, mechanical equilibrium in the fluid can be stated in terms of the normal component $p_\perp$ of the pressure tensor* as [122]

$$\frac{dp_\perp(z)}{dz} = -\rho_h(z)\, \phi_h'(z) = \begin{cases} -\rho_h(z)\, w_{\mathrm{L}}'\left(z + \frac{h}{2}\right) & z < 0\,, \\ -\rho_h(z)\, w_{\mathrm{R}}'\left(z - \frac{h}{2}\right) & z > 0\,. \end{cases} \tag{4.9}$$

Equations (4.8) and (4.9) together lead to the simple and intuitive result

$$\begin{aligned} F_{\mathrm{L}}(h) &= p_\perp(-\infty) - p_\perp(0)\,, \\ F_{\mathrm{R}}(h) &= p_\perp(0) - p_\perp(+\infty)\,; \end{aligned} \tag{4.10}$$

in other words, the force per unit area exerted on a wall just depends on the difference between the normal pressure evaluated at the midpoint between the walls and the same quantity evaluated at infinity. We stress that the previous result holds irrespective of the thermodynamic state of the fluid and, if extrapolated beyond the lower bound (4.5), it gives the correct Asakura-Oosawa limit. Moreover, since far from the walls the normal pressure must approach the bulk value p_0:

$$p_\perp(-\infty) = p_\perp(+\infty) = p_0\,, \tag{4.11}$$

---

*In the slab geometry considered here, the pressure tensor has the diagonal form $(p_\parallel, p_\parallel, p_\perp)$, the component $p_\perp$ corresponding to the direction perpendicular to the walls.

we see that the two forces are equal in magnitude and opposite in direction:

$$F_{\mathrm{R}}(h) = -F_{\mathrm{L}}(h) \doteq F(h)\,, \tag{4.12}$$

where we elected the force acting on the right wall as the representative fluctuation-induced force $F(h)$. According to the chosen convention a negative force means attraction between the walls, whereas a positive force indicates repulsion. Finally, although $F(h)$ is given exactly by Equation (4.8b), it may as well be written in the more symmetric form

$$F(h) = \frac{1}{2} \int_{-\infty}^{+\infty} dz\, \rho_h(z) \left[w_{\mathrm{R}}'\left(z - \frac{h}{2}\right) - w_{\mathrm{L}}'\left(z + \frac{h}{2}\right) \right]\,. \tag{4.13}$$

4.2 DENSITY FUNCTIONAL METHODS

In order for the previous equation to be of any avail the equilibrium density profile $\rho_h(z)$ of the fluid must be computed. This is most easily done within the density functional formulation of the statistical mechanics of inhomogeneous fluids [57]. We work in a grand-canonical ensemble at fixed chemical potential μ, so that a one-to-one correspondence exists between the external potential due to the presence of the walls and the equilibrium density profile of the fluid. This property, together with the form of Equation (4.13), implies that the force per unit surface $F(h)$ may be expressed solely in terms of $\rho_h(z)$, without explicit reference to the particle-wall potential.

The fundamental link between the external potential and the equilibrium density profile is provided by the grand potential functional $\omega_h[n(z)]$, which depends on a trial density profile $n(z)$. Owing to the particular geometry of the problem, we define all thermodynamic potentials per unit cross-sectional area along the z direction. The grand potential functional may then be written in terms of the intrinsic Helmholtz free energy functional $a[n(z)]$ as

$$\omega_h[n(z)] = a[n(z)] + \int_{-\infty}^{+\infty} dz\, n(z) \left[w_{\mathrm{L}}\left(z + \frac{h}{2}\right) + w_{\mathrm{R}}\left(z - \frac{h}{2}\right) - \mu \right]\,. \tag{4.14}$$

The basic result of density functional theory states that the grand potential functional is minimized by the equilibrium density profile, and the minimum coincides with the actual grand potential Ω_h of the system:

$$\omega_h[n(z)] \geq \omega_h[\rho_h(z)] = \Omega_h \qquad \text{for all } n(z)\,; \tag{4.15}$$

The minimization of the functional translates into the equation

$$\left. \frac{\delta a[n(z)]}{\delta n(z)} \right|_{n(z)=\rho_h(z)} + w_{\mathrm{L}}\left(z + \frac{h}{2}\right) + w_{\mathrm{R}}\left(z - \frac{h}{2}\right) = \mu\,, \tag{4.16}$$

that has to be solved for $\rho_h(z)$ with the two asymptotic boundary conditions

$$\lim_{z \to -\infty} \rho_h(z) = \lim_{z \to +\infty} \rho_h(z) = n_0\,, \tag{4.17}$$

n_0 being the bulk, unperturbed density of the fluid far from the walls. Note that the bulk density and the chemical potential are not independent, since they are related by the thermodynamic identity

$$\mu = \left. \frac{\delta a[n(z)]}{\delta n(z)} \right|_{n(z)=n_0} = \left. \frac{\partial f(n)}{\partial n} \right|_{n=n_0}\,, \tag{4.18}$$

where we denote by $f(n)$ the Helmholtz free energy per unit volume of the homogeneous fluid as a function of its density.[†]

Equation (4.16) allows, as we predicted, to eliminate any explicit reference to the wall-particle interaction from the expression (4.13) of the force, leading to

$$F(h) = \frac{1}{2} \int_{-\infty}^{+\infty} dz \, \text{sgn}(z) \, \rho_h'(z) \left[\left. \frac{\delta a[n(z)]}{\delta n(z)} \right|_{n(z)=\rho_h(z)} - \mu \right] , \qquad (4.19)$$

where $\text{sgn}(z) = |z|/z$ is the sign function. Although the latter is discontinuous, the integrand in Equation (4.19) is a continuous function since the quantity within square brackets vanishes upon approaching $z = 0$.

As a further remark, note that owing to the minimum condition (4.16) the derivative of the grand potential Ω_h with respect to the interplate distance h is

$$\frac{d\Omega_h}{dh} = -\frac{1}{2} \int_{-\infty}^{+\infty} dz \, \rho_h(z) \left[w_{\text{R}}' \left(z - \frac{h}{2} \right) - w_{\text{L}}' \left(z + \frac{h}{2} \right) \right] = -F(h) . \qquad (4.20)$$

In other words, the contribution to the grand potential of the system ascribable to the concurrent presence of the two walls simply equals the minimum, quasi-static work that one has to perform to bring the walls from infinite distance to their actual position.

4.3   LONG-WAVELENGTH ANALYSIS

The key ingredient missing to put all the machinery devised in the previous sections to work is an expression for the intrinsic Helmholtz free energy functional $a[n(z)]$, which embodies the properties of the fluid. Since we aim to describe a force $F(h)$ due to fluctuations happening on a length scale much larger than the individual particle size σ, we adopt a functional apt to represent long-wavelength density modulations. In particular, we choose a local density approximation plus a square gradient correction:

$$a[n(z)] = \int_{-\infty}^{+\infty} dz \left[\frac{b}{2} |n'(z)|^2 + f(n(z)) \right] , \qquad (4.21)$$

where the prime denotes as usual differentiation with respect to the spatial coordinate and $f(n)$ is the Helmholtz free energy per unit volume of the homogeneous fluid already introduced. The parameter b measures the stiffness of the fluid with respect to variations in the density. Clearly this functional is inadequate to describe the strong oscillations taking place close to a wall, nevertheless it correctly takes into account the overall monotonic decay of the density profile over distances much larger than σ. In order to get further physical insight on the structure of the functional we may switch to the language of correlation functions: the form (4.21) then corresponds to a small-wavevector truncation of the direct correlation function $c(r)$ of the homogeneous fluid

$$\hat{c}(q) = \hat{c}(0) - \frac{b}{k_B T} q^2 , \qquad (4.22)$$

where the hat denotes the three-dimensional Fourier transform.[‡] As a consequence, the stiffness parameter b is proportional to the second moment of the correlation

---

[†]We drop the temperature dependence of the free energy for notational convenience.

[‡]This can be checked by recalling that the direct correlation function is the second functional derivative of the excess Helmholtz free energy (divided by $-k_{\text{B}}T$) with respect to the density profile.

function:

$$b = \frac{k_B T}{6} \int d\boldsymbol{r} \, r^2 \, c(r) \,. \tag{4.23}$$

Note for later reference that b is dimensionally an energy times a length raised to the fifth power. We finally observe that the structure of Equation (4.21) is consistent with the long-wavelength limit of accurate density functionals commonly used in the literature [32].

If the intrinsic Helmholtz free energy functional is inserted into Equation (4.19) and the boundary conditions (4.17) are taken into account, the expression of the force acting on the walls may be written as

$$F(h) = [f(n_0) - f(\rho_h(0))] - \mu \, [n_0 - \rho_h(0)] + \frac{b}{2} \, [\rho_h'(0)]^2 \,. \tag{4.24}$$

Thus, the force can be expressed solely in terms of the Helmholtz free energy of the homogeneous fluid, the bulk fluid density, and the equilibrium density profile evaluated, together with its first spatial derivative, at the midpoint between the two plates. Note the connection with Equation (4.10). In the previous expression the spatial derivative of the density profile appears squared, which implies that the force is correctly invariant under a reflection about the $z = 0$ plane. If the density profile itself is invariant under the same operation, that is if the two walls are alike, the last term in Equation (4.24) vanishes.

The minimum condition (4.16) characterizing the equilibrium density profile, once the particular form of the Helmholtz free energy functional is taken into account, becomes

$$-b\rho_h''(z) + \left.\frac{\partial f(n)}{\partial n}\right|_{n=\rho_h(z)} + w_{\mathrm{L}} \left(z + \frac{h}{2} \right) + w_{\mathrm{R}} \left(z - \frac{h}{2} \right) = \mu \,. \tag{4.25}$$

Where the wall-particle potential vanishes, that is to say in each of the three spatial intervals I_i

$$\begin{aligned}
I_0 &= \left(-\infty, \, -\frac{h}{2} - d_0 \right) \,, \\
I_1 &= \left(-\frac{h}{2} + d_0, \, \frac{h}{2} - d_0 \right) \,, \\
I_2 &= \left(\frac{h}{2} + d_0, \, +\infty \right) \,,
\end{aligned} \tag{4.26}$$

the previous equation has a first integral $\mathscr{C}_i$:

$$\frac{b}{2} \, [\rho_h'(z)]^2 + \Gamma(\rho_h(z)) = \mathscr{C}_i \,, \qquad \Gamma(n) \doteq \mu n - f(n) \,. \tag{4.27}$$

In particular, we see from Equation (4.24) that in the central interval the constant is closely related to the force acting on the walls, so that the first integral may there be rewritten as

$$\frac{b}{2} \, [\rho_h'(z)]^2 + \Pi(\rho_h(z)) = F(h) \,, \qquad z \in I_1 \,, \qquad \Pi(n) \doteq \Gamma(n) - \Gamma(n_0) \,. \tag{4.28}$$

Interestingly, this statement is formally equivalent to the conservation of mechanical energy in the one-dimensional motion of a fictitious particle with mass b in an external

potential Π. Since the latter is a linear function of a free energy density and hence is likely to be smooth and regular, the equilibrium density profile is expected to be smooth and regular as well in the interval I_1 – the same of course holds for $z \in I_0, I_2$. Conversely, for $|z \pm h/2| < d_0$ the density profile may vary wildly as a consequence of the interaction with the walls. We may *define* in the enlarged interval $\bar{I}_1 = [-h/2, h/2]$ a smoothed equilibrium density profile $\varrho_h(z)$ as the unique solution to Equation (4.25) in the absence of any wall-particle potential that coincides with the wall-dependent equilibrium density profile $\rho_h(z)$ in the interval I_1. We may then define the two wall contact densities $n_{\mathrm{L}}^{\mathrm{c}}, n_{\mathrm{R}}^{\mathrm{c}}$ as

$$n_{\mathrm{L}}^{\mathrm{c}} = \varrho_h\left(-\frac{h}{2}\right), \qquad n_{\mathrm{R}}^{\mathrm{c}} = \varrho_h\left(+\frac{h}{2}\right), \tag{4.29}$$

so that they are a kind of smooth extrapolation (in the sense defined above) to the surface of the walls of the equilibrium density profile. Note that as such they are functions of the bulk density n_0 and of the distance between the walls h.

Owing to the previous definitions the calculation of the fluctuation-induced force acting on the walls can be restated as a boundary value problem. For later convenience, we re-express any density variable n in terms of the deviation $\delta n = n - n_0$ from the bulk value n_0, so that the the pseudo-potential Π takes the alternative form

$$\tilde{\Pi}(\delta n) = \Pi(n_0 + \delta n) = \delta n \left.\frac{\partial f(n)}{\partial n}\right|_{n=n_0} - f(n_0 + \delta n) + f(n_0). \tag{4.30}$$

Accordingly, an implicit relation between F and h is provided in terms of the wall contact densities $n_{\mathrm{L}}^{\mathrm{c}}, n_{\mathrm{R}}^{\mathrm{c}}$ by the boundary value problem

$$\begin{cases} \dfrac{b}{2}\left[\delta n'(z)\right]^2 + \tilde{\Pi}(\delta n(z)) = F, \qquad z \in \left[-\dfrac{h}{2}, \dfrac{h}{2}\right], \\[2ex] \delta n\left(-\dfrac{h}{2}\right) = \delta n_{\mathrm{L}}^{\mathrm{c}}, \\[2ex] \delta n\left(+\dfrac{h}{2}\right) = \delta n_{\mathrm{R}}^{\mathrm{c}}, \end{cases} \tag{4.31}$$

whose solution is the deviation from the bulk of the smoothed equilibrium density profile, that is $\varrho_h(z) - n_0$.

4.4   DEPLETION AT CRITICALITY

In the critical region the free energy of a homogeneous, simple fluid, when expressed in terms of two suitably-chosen scaling fields related to the density n and the temperature T, may be written in a universal form [131]. The first scaling field ε can be chosen as the reduced temperature

$$\varepsilon = \frac{T - T_c}{T_c}, \tag{4.32}$$

where T_c is the critical temperature of the fluid. The choice of the second field u can be, on the contrary, rather subtle. In a lattice fluid model, where particle-hole symmetry holds, it simply measures the distance of the density from the critical one: $u = n - n_c$. This indeed makes sense, since in this simple case the coexistence curve is symmetric about the critical isochore; the latter also coincides, above T_c, with the

locus $\bar{n}(T)$ of the maxima of the isothermal susceptibility χ_T:

$$\chi_T \doteq \left(\frac{\partial^2 f(T,n)}{\partial n^2} \right)^{-1} , \qquad \left. \frac{\partial^3 f(T,n)}{\partial n^3} \right|_{n=\bar{n}(T)} = 0 \,. \qquad (4.33)$$

In a real fluid the coexistence curve can be noticeably skewed, so that the critical isochore and the locus $\bar{n}(T)$ do not coincide, although they both end at the critical point [142]. The vanishing of the scaling field u, whatever its definition, identify precisely the line $\bar{n}(T)$, which is the most natural direction of approach to the critical point, namely the one dictated by the shape of the coexistence curve and the symmetry of the free energy itself. In the following we will consider a scaling field linear in the density of the fluid, so that necessarily

$$u(T,n) = n - \bar{n}(T) \,. \qquad (4.34)$$

That this is a sensible choice, besides being the simplest, can be checked at the mean-field level, in which case a power expansion of the free energy about the locus of the maxima of the susceptibility naturally leads to a scaling form depending on a field u defined in accordance to Equation (4.34).

With the two scaling fields just defined and adopting the notation of Pelissetto and Vicari [102], the free energy density $f(T,n)$ may be written in the critical region as

$$f(T,n) = f(T,\bar{n}(T)) + k_{\mathrm{B}}T \, a_{11} \, \varepsilon^{2-\alpha} \, \Psi \left(b_1 \, u(T,n) \, \varepsilon^{-\beta} \right) \,, \qquad (4.35)$$

where α, β are the critical exponents governing the divergence of the specific heat and the shape of the coexistence curve, respectively; $\Psi(\cdot)$ is a universal scaling function; a_{11}, b_1 are non-universal metric factors with the dimensions of the inverse of a volume and of a volume, respectively.

In order for the long-wavelength analysis developed in Section 4.3 to hold in the critical region, the stiffness constant b must stay finite and approximately constant upon approaching the critical point. Strictly speaking this is not the case, since the Fisher exponent η is positive and not null in three dimensions, so that the direct correlation function $c(r)$ has at criticality the asymptotic behavior [46]

$$c(r) \sim r^{-5+\eta} \,, \qquad r \to +\infty \,, \qquad (4.36)$$

causing the second moment (4.23) to be infinite. However, a reliable estimate for the exponent is $\eta \approx 0.04$ and we can safely disregard such a weak singularity if we are not exceedingly close to the critical point. Therefore, in the following we explicitly set $\eta = 0$.

The scaling behavior of the free energy suggests that in the critical region it is advantageous to express the various physical variables in terms of rescaled, adimensional quantities. For this purpose we build using the stiffness constant b, the metric factors b_1 and a_{11}, the reduced temperature ε and the thermal energy $k_{\mathrm{B}}T$

- ❖ a scaling particle density $\mathscr{D}_s \doteq (b_1)^{-1} \, \varepsilon^{\beta}$;

- ❖ a scaling energy density $\mathscr{E}_s \doteq \mathscr{E}_0 \, \varepsilon^{2-\alpha}$, $\mathscr{E}_0 = k_{\mathrm{B}}T \, a_{11}$;

- ❖ a scaling length $\mathscr{L}_s \doteq \mathscr{L}_0 \, \varepsilon^{-\nu}$, $\mathscr{L}_0 = \sqrt{\frac{b}{b_1^2 \, a_{11} \, k_{\mathrm{B}}T}}$, where $\nu = 2\beta = (2-\alpha)/3$ is the critical exponent governing the divergence of the correlation length ξ of the fluid along the line $u = 0$.

The first two definitions are a natural consequence of the scaling form of the free energy. It is also perfectly sensible to define the scaling length $\mathscr{L}_s$ so that it scales as the correlation length of the fluid, and the factor $\mathscr{L}_0$ is just the simplest constant with the right dimensions that can be obtained by combining all the aforementioned dimensional factors. Note, however, that using the relation (4.22) it can be shown that b coincides with the ratio $(f^+)^2/C^+$, where f^+ and C^+ are the amplitudes governing the divergence of the correlation length and of the isothermal susceptibility, respectively, as the critical point is approached along the path defined by $u = 0$. Moreover, from the definition (4.35) of the free energy readily follows that $(C^+)^{-1} = b_1^2 \, a_{11} \, k_{\mathrm{B}} T$, hence $\mathscr{L}_0 = f^+$ and the scaling length $\mathscr{L}_s$ corresponds exactly to the temperature-dependent correlation length of the fluid on the reference line $\bar{n}(T)$:

$$\mathscr{L}_s(T) = \xi(T, \bar{n}(T)) \,, \qquad u(T, \bar{n}(T)) = 0 \,. \tag{4.37}$$

Using the scaling constants just defined, we substitute the old, dimensional quantities with adimensional scaling variables in accordance with the following scheme:

$$
\begin{aligned}
n_0 &\longmapsto x \doteq u(T, n_0)/\mathscr{D}_s \,, \\
\delta n &\longmapsto \varphi \doteq \delta n/\mathscr{D}_s \,, \\
\tilde{\Pi} &\longmapsto \mathbb{P} \doteq \tilde{\Pi}/\mathscr{E}_s \,, \\
F &\longmapsto \sigma \doteq F/\mathscr{E}_s \,, \\
z &\longmapsto s \doteq z/\mathscr{L}_s \,, \\
h &\longmapsto \kappa \doteq h/\mathscr{L}_s \,.
\end{aligned}
\tag{4.38}
$$

The rescaled pseudo-potential $\mathbb{P}$ can be expressed in terms of the scaling function $\Psi(\cdot)$ of the free energy as

$$\mathbb{P}(\varphi; x) = \varphi \, \Psi'(x) - \Psi(x + \varphi) + \Psi(x) \,. \tag{4.39}$$

Owing to the previous definitions, the boundary value problem (4.31) acquires in the critical region the form

$$
\begin{cases}
\dfrac{1}{2} \left(\dfrac{d\varphi(s)}{ds} \right)^2 + \mathbb{P}(\varphi(s); x) = \sigma \,, & s \in \left[-\dfrac{\kappa}{2}, \dfrac{\kappa}{2} \right] \,, \\[2ex]
\varphi \left(-\dfrac{\kappa}{2} \right) = \delta n_{\mathrm{L}}^{\mathrm{c}}/\mathscr{D}_s = b_1 (n_{\mathrm{L}}^{\mathrm{c}} - n_0) \, \varepsilon^{-\nu} \,, \\[2ex]
\varphi \left(+\dfrac{\kappa}{2} \right) = \delta n_{\mathrm{R}}^{\mathrm{c}}/\mathscr{D}_s = b_1 (n_{\mathrm{R}}^{\mathrm{c}} - n_0) \, \varepsilon^{-\nu} \,.
\end{cases}
\tag{4.40}
$$

Note that thanks to the rescaling the differential equation is now free from any fluid-specific parameter.

To get an intuitive grasp on the behavior of the solutions to this equation it is convenient to revert again to the mechanical analogy already introduced in Section 4.3: if time is substituted for the variable s and a spatial coordinate is substituted for the rescaled density φ, the differential problem (4.40) may be thought to describe the one-dimensional motion of a point particle with unit mass under the effect of the pseudo-potential $\mathbb{P}$ and with total, conserved mechanical energy σ. From the definition (4.39) the following properties of the pseudo-potential may be derived, irrespective of the value of the scaling variable x:

$$
\begin{aligned}
&\mathbb{P}(0; x) = 0 \,, \\
&\mathbb{P}_\varphi(0; x) = 0 \,, \\
&\mathbb{P}_{\varphi\varphi}(\varphi; x) = -\Psi''(x + \varphi) < 0 \quad \text{for all } \varphi \,,
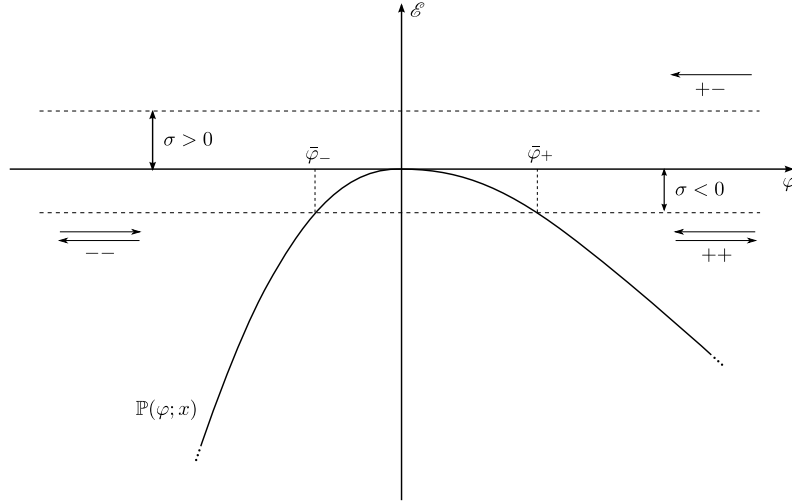\end{aligned}
\tag{4.41}
$$

Figure 4.1: Schematic depiction of the mechanical analogy presented in the text. $\mathbb{P}$ is the potential energy determining the one-dimensional motion of a point particle with unit mass; σ is the total, conserved mechanical energy; $\bar{\varphi}_\pm$ are turning points in the case of negative total energy; the motion both starts and ends at infinity.

where the subscript indicates differentiation and the third property ensures thermodynamic stability of the fluid. The shape of the function $\mathbb{P}(\varphi; x)$ is therefore as depicted pictorially in Figure 4.1. Moreover, the two boundary conditions in (4.40) are pushed to infinity as the critical temperature is approached, the sign depending on the relative magnitude of the density at contact and the bulk density. Therefore, asymptotically close to the critical point and owing to the left-right symmetry of the force only three distinct types of boundary conditions are possible, which we indicate schematically by "$++$", "$--$" and "$+-$". In the mechanical analogy, they correspond to the following scenarios:

- ❧ $++$, $--$: the particle comes from $\pm\infty$, bounces off the potential at $\varphi = \bar{\varphi}_\pm$ and then returns back to infinity;

- ❧ $+-$: the particle travels from $-\infty$ to $+\infty$ (or the other way round) without any reflection from the potential.

Looking at Figure 4.1 we see that the former case is compatible with a negative "total mechanical energy" σ, whereas the latter requires σ to be positive. Without performing any calculation we thus deduce the very general property that symmetric boundary conditions correspond to an attractive force, while asymmetric boundary conditions imply repulsion. The two reflection points $\bar{\varphi}_\pm$ in the case $\sigma < 0$ are defined by

$$\mathbb{P}(\bar{\varphi}_\pm; x) = \sigma, \qquad \sigma < 0. \tag{4.42}$$

Reversing the definitions (4.38) we get an expression for the actual force per unit surface acting on the walls:

$$F = \mathscr{E}_s\, \sigma = \mathscr{E}_0\, \varepsilon^{2-\alpha} \sigma = \mathscr{E}_0\, \varepsilon^{3\nu} \sigma = \mathscr{E}_0\, \mathscr{L}_0^3\, \frac{\kappa^3 \sigma}{h^3}\,. \tag{4.43}$$

Surprisingly, the system-dependent factors concealed in the constants $\mathscr{E}_0$ and $\mathscr{L}_0$ combine to give a universal amplitude ratio g_4^+ [102]:

$$\mathscr{E}_0 \, \mathscr{L}_0^3 = k_{\mathrm{B}} T \, a_{11} \, (f^+)^3 = \frac{k_{\mathrm{B}} T}{g_4^+} \, ; \tag{4.44}$$

in three dimensions $g_4^+ \approx 23.6$. Consequently, the force may be expressed in the form

$$F(h) = \frac{k_{\mathrm{B}} T}{h^3} \, \Theta_{\mathcal{B}} \left(h/\mathscr{L}_s ; x \right) , \qquad \Theta_{\mathcal{B}}(\kappa; x) \doteq \frac{\kappa^3 \sigma_{\mathcal{B}}(\kappa; x)}{g_4^+} , \tag{4.45}$$

where $\Theta_{\mathcal{B}}$ denotes a universal scaling function that does not involve any system-specific dimensional constant, but depends solely on the type $\mathcal{B}$ of the boundary conditions, with $\mathcal{B} \in \{++,--,+-\}$. This is precisely the form expected for the critical Casimir force on the basis of finite-size scaling arguments as first predicted by Fisher and de Gennes [47]. We then conclude that the same mechanism which gives rise to standard depletion effects in non critical fluids, very well described by the density functional approach we have been using, is responsible for the critical Casimir force when critical fluctuations set in.

If a more quantitative analysis is desired, the differential problem (4.40) can be reduced to quadratures, with three distinct forms corresponding to the possible boundary conditions:

$$\boxed{++} \qquad \sigma < 0 \, , \qquad \kappa = \sqrt{2} \int_{\bar{\varphi}_+}^{+\infty} d\varphi \, (\sigma - \mathbb{P}(\varphi, x))^{-1/2} \, ; \tag{4.46a}$$

$$\boxed{--} \qquad \sigma < 0 \, , \qquad \kappa = \sqrt{2} \int_{-\infty}^{\bar{\varphi}_-} d\varphi \, (\sigma - \mathbb{P}(\varphi, x))^{-1/2} \, ; \tag{4.46b}$$

$$\boxed{+-} \qquad \sigma > 0 \, , \qquad \kappa = \frac{1}{\sqrt{2}} \int_{-\infty}^{+\infty} d\varphi \, (\sigma - \mathbb{P}(\varphi, x))^{-1/2} \, . \tag{4.46c}$$

The previous relations allow to express the rescaled force as a function of the rescaled interplate distance and the rescaled bulk density: $\sigma = \sigma(\kappa; x)$, so that the scaling function $\Theta_{\mathcal{B}}$ may be computed by means of Equation (4.45). Before performing a numerical calculation, a number of general properties concerning symmetries and asymptotic behaviors are readily obtained. As a starting point, note that the scaling function $\Psi(\cdot)$ of the free energy is even [102], therefore owing to the definition (4.39) the pseudo-potential $\mathbb{P}$ is unaffected by a simultaneous change of sign of both of its arguments:

$$\mathbb{P}(-\varphi; -x) = \mathbb{P}(\varphi; x) \, ; \tag{4.47}$$

this also means that the turning points $\bar{\varphi}_+$ and $\bar{\varphi}_-$ are related by

$$\bar{\varphi}_+(\sigma; x) = -\bar{\varphi}_-(\sigma; -x) \, , \qquad \sigma < 0 \, . \tag{4.48}$$

As a consequence the scaling function $\Theta_{\mathcal{B}}$, hence the Casimir force, has the following symmetries:

$$\begin{aligned} \Theta_{++}(\kappa; -x) &= \Theta_{--}(\kappa; x) \, , \\ \Theta_{+-}(\kappa; -x) &= \Theta_{+-}(\kappa; x) \, . \end{aligned} \tag{4.49}$$

Moreover, using the formulae (4.46) the asymptotic regime $|\sigma| \to 0, \kappa \to +\infty$ can be evaluated, leading to the relation

$$|\sigma(\kappa; x)| \sim \exp\left[-\kappa \sqrt{\Psi''(x)} \right] , \tag{4.50}$$
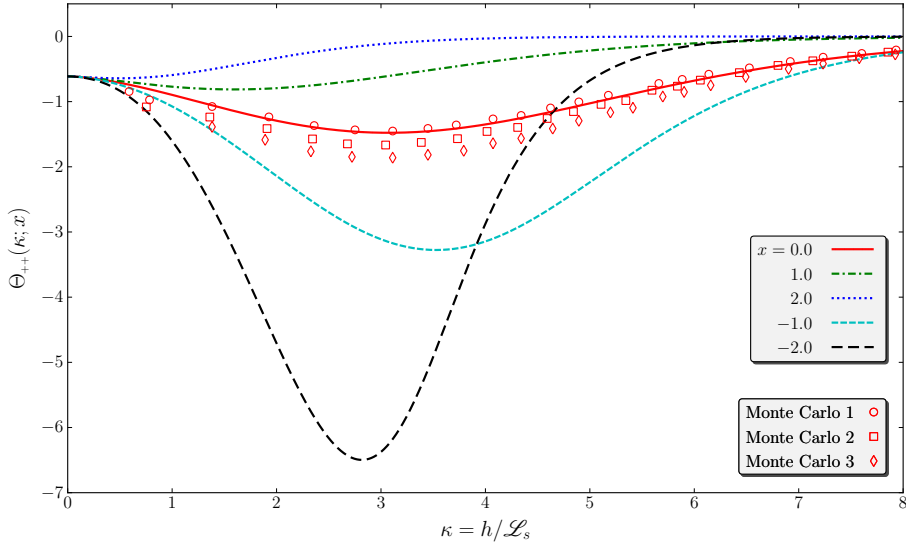
Figure 4.2: Scaling function of the fluctuation-induced force F corresponding to ++ boundary conditions computed by means of Equation (4.46a) for a number of choices of the rescaled bulk density x. The same lines apply for −− boundary conditions, provided the sign of the scaling variable x is reversed. The symbols denote Monte Carlo simulation data for the case $x = 0$ as appearing in Fig. 9 of Ref. [140]; the three sets differ in the kind of finite-size correction applied.

which holds irrespective of the boundary conditions; the radicand is always non-negative for reasons of thermodynamic stability. The result in turn implies that the force F has for large h the asymptotic behavior

$$|F(h)| \sim \frac{k_{\mathrm{B}}T}{\mathscr{L}_s^3} \exp\left(-\frac{h}{h_\infty}\right), \qquad h_\infty \doteq \mathscr{L}_s/\sqrt{\Psi''(x)}; \qquad (4.51)$$

the range h_∞ of the force thus scales as $\mathscr{L}_s$, that is as the correlation length of the fluid on the line defined by $u = 0$. In the limit of small h, on the contrary, the force is formally divergent. This is clearly an artifact due to the extrapolation of the correct, long range behavior to a regime where small-wavelength density fluctuations play a major role that cannot be accounted for by the approximated functional (4.21). As a consequence, the universal form (4.45) holds only beyond a certain cut-off distance h_c that, in the light of the hypothesis (4.5) underlying the derivation of all the previous expressions, is at the least equal to the fluid-wall interaction range d_0 (but could also be greater). In the interval $0 < h < h_c$ a non-universal, finite force depending on the details of the fluid-wall interaction is expected.

Using a suitable representation of the free energy scaling function $\Psi(\cdot)$, for instance the parametric representation given in [102], the scaling function $\Theta_\mathcal{B}$ of the force can be evaluated numerically. Figure 4.2 presents the results for ++ boundary conditions and a number of different values of the rescaled bulk density x. The case $x = 0$, corresponding to a bulk density lying on the path $\bar{n}(T)$, is surely the most studied in the literature: a comparison of our result with recent Monte Carlo simulation data computed with reference to a three-dimensional Ising model [140] shows a satisfactory
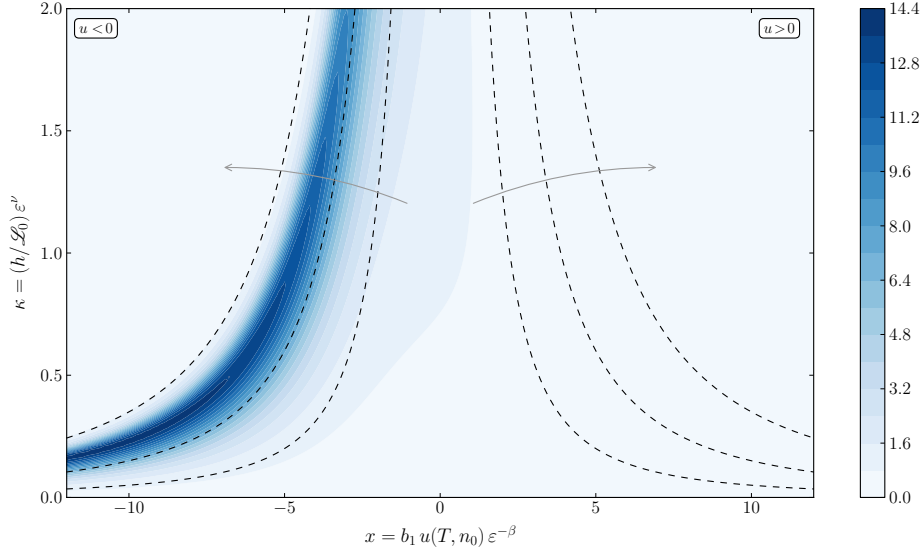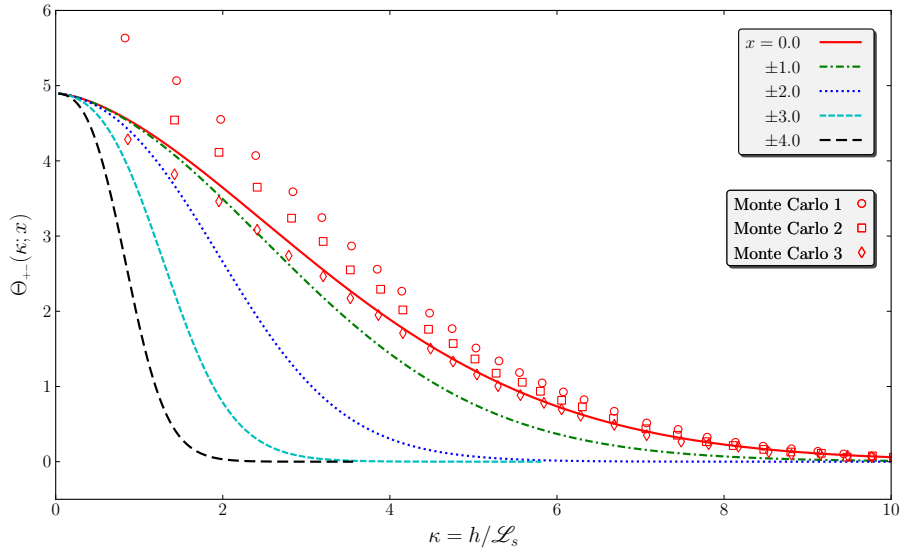
Figure 4.3: Absolute value of the scaling function $\Theta_{++}(\kappa; x)$ plotted in the x, κ plane as a pseudo-color map. The function is negative in the whole plane. The dashed lines define thermodynamic paths at constant u and h (the arrows indicate the direction of increasing $|u|$ or h). The same plot applies to $\Theta_{--}(\kappa; -x)$.

Figure 4.4: Scaling function of the fluctuation-induced force F corresponding to $+-$ boundary conditions computed by means of Equation (4.46c) for a number of choices of the rescaled bulk density x. The symbols denote Monte Carlo simulation data for the case $x = 0$ as appearing in Fig. 10 of Ref. [140]; the three sets differ in the kind of finite-size correction applied.

agreement. Note that the curve is not monotonic but instead has a minimum in $\kappa \approx 3$: this entails that at fixed wall-to-wall distance the attractive, fluctuation-induced force attains a maximum *not* at the critical temperature, that would correspond to $\kappa = 0$, but at a certain distance from it. The off-critical case $x \neq 0$ is far less represented in the literature, to the point that we could not find any independent quantitative data to compare our results with. Our method suggests that all the curves start with a common value $\theta_0 \approx -0.6$ in $\kappa = 0$, but then they soon depart in a manner that markedly depends on the sign of the rescaled bulk density. If x is increased from zero in the positive direction the amplitude of the scaling function rapidly decays; contextually, the minimum flattens until the function eventually becomes monotonic. If, on the contrary, x is pushed in the negative direction the minimum of the scaling function grows and gradually shifts towards the origin. Therefore, it appears that the scaling function is particularly enhanced in the region where the rescaled bulk density has a sign *opposite* to the one that would be suggested by the boundary conditions. The phenomenon is better illustrated in Figure 4.3, where the absolute value of the scaling function Θ_{++} is plotted as a pseudo-color map in the x, κ plane. If one fixes the temperature and the bulk density, which amounts to keeping x constant, the corresponding vertical slice of the plot describes Θ_{++} as a function of the distance between the walls, just as in Figure 4.2. Another family of significant paths, shown in the plot with dashed lines, is obtained by fixing the distance h and the value of the scaling field u: in this way one can follow the amplitude of the scaling function at fixed interplate distance along a set of lines that in a density-temperature diagram are parallel to the locus $\bar{n}(T)$ of the maxima of the susceptibility. In either case, it is apparent that the scaling function is quite small along all the paths corresponding to $u > 0$, whereas for $u < 0$ it can attain significant values. Therefore, on general grounds we expect that $u \approx 0$ should mark the transition between a region where attractive Casimir forces are negligible ($u > 0$) and a regime where they become relevant ($u < 0$). The situation is of course reversed if $--$ boundary conditions apply.

Figure 4.4 shows the behavior of the scaling function in the case of asymmetric (that is $+-$) boundary conditions. The curve corresponding to $x = 0$ is again consistent with the results of Monte Carlo simulations but, contrary to the previous case, the scaling function is always monotonic and its amplitude constantly decays as x departs from zero in either direction. Therefore, we expect the effects of the repulsion between the walls (if any) to be particularly evident in the region defined by $u \approx 0$.

4.5   FLUCTUATION-INDUCED COLLOIDAL AGGREGATION

Thus far we have been dealing with the fluctuation-induced force acting on a pair of parallel, infinite plates lying inside a correlated fluid. This is clearly a highly idealized geometry that is rarely found in practice: the experimental measurement and also the potential technological application of the critical Casimir force require the effect to be studied in more realistic geometries.

With regard to measurements, several experiments have been conducted to date bearing both direct and indirect evidence of the critical Casimir force. Only a few years after the conjecture of Fisher and de Gennes, Beysen and Estève reported that silica colloidal particles dispersed in a fluid undergo a reversible aggregation process when the latter is close to its critical point, a fact that can be ascribed to the development of an attractive interaction among the particles [20]. This seminal work was followed by a number of similar experiments involving the reversible flocculation of silica or polystyrene spheres dispersed in a critical solvent [49, 50, 92, 68, 54]. Be warned, however, that in all these papers no explicit mention to the critical Casimir

force is to be found, since the experimental findings were explained in terms of capillary condensation, preferential adsorption, bridging and still other closely-related wetting phenomena. A direct measurement of the fluctuation-induced force acting between a single colloidal sphere and a flat silica surface was achieved only recently by Bechinger and collaborators using the technique of total internal reflection microscopy [59]. In most of the aforementioned experiments a binary mixture of water and an organic solvent (2,6-lutidine or 3-methylpyrydine) in a thermodynamic state close to the demixing phase transition was exploited as the underlying critical system. This choice was ideal to highlight the phenomena taking place in the critical region, but unfortunately could not offer any glimpse on a possible connection with the non-critical, well-understood depletion interaction, that requires macromolecular compounds such as polymers or amphiphiles to be induced. An experiment that potentially offers such a connection was conducted in 1996 by Degiorgio and collaborators, who noticed that in aqueous suspensions containing polymer colloids and a nonionic amphiphile, the minimum amphiphile concentration required to induce a reversible flocculation of the colloidal particles decreases as the temperature of the suspension approaches the cloud point temperature of the water-amphiphile system [34]. Again, no conscious mention to fluctuation-induced forces is to be found in the paper, since the interest of the authors was focused on depletion phenomena.

The work described in this chapter was prompted by a re-edition of this latter experiment recently performed by Piazza and Buzzaccaro with the precise intent of finally bridging the gap between the two worlds [25]. Before presenting the experiment in more detail and comparing their findings with some sensible theoretical prediction, we had better adapt our theoretical framework to the spherical geometry suited for colloidal particles.

4.5.1   Quasi-planar approximation

We seek an expression for the fluctuation-induced interaction between two equal-sized spherical particles embedded in a correlated fluid. If we were to follow the same line of reasoning that led us to the force acting on the pair of plates, we would be faced with a rather complex task. Indeed, while in the planar case the invariance of the system with respect to any translation in a direction parallel to the walls renders the problem effectively one-dimensional, in the case of two spheres we would be left with an extra dimension due to the more limited cylindrical symmetry.

Thankfully, as long as the distance of closest approach between the two spheres – that we still denote by h with little abuse of notation – and the range of their interaction are both small if compared to the sphere radius R, a simple approximation due to the Soviet chemist Boris Derjaguin can be invoked. Accordingly, the energy of interaction v of the two spheres can be written in terms of the force per unit area F in planar geometry as [35, 97]

$$v(h) \approx \pi R \int_{h}^{+\infty} dh' \, (h' - h) F(h') \,, \qquad h, \mathscr{L}_s \ll R \,; \tag{4.52}$$

where we recalled that the range of the force F is proportional to the correlation length $\mathscr{L}_s$. This quasi-planar approximation is commonly applied when dealing with short-range interactions [100].

According to our long-wavelength analysis the energy of interaction acquires in the critical regime a universal form that readily follows from the scaling behavior (4.45) of the planar force F:

$$v(h) = k_{\mathrm{B}} T \, \frac{R}{h} \, \Theta_{\mathscr{B}}^{\circ}(h/\mathscr{L}_s; x) \,, \tag{4.53}$$
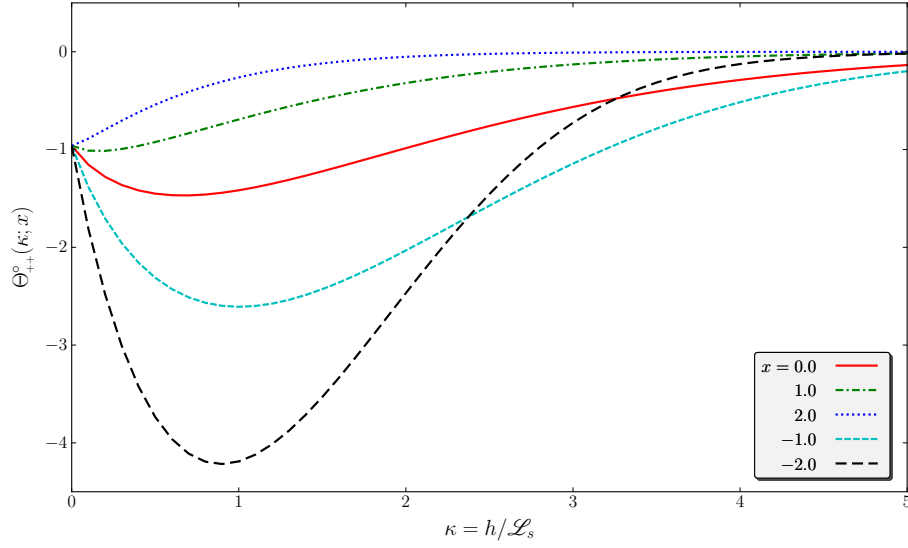
Figure 4.5: Scaling function for the energy of interaction of two spheres with $++$ boundary conditions computed by means of Equation (4.53) for a number of choices of the rescaled bulk density x. The same plot applies to $--$ boundary conditions, provided the sign of the variable x is reversed.
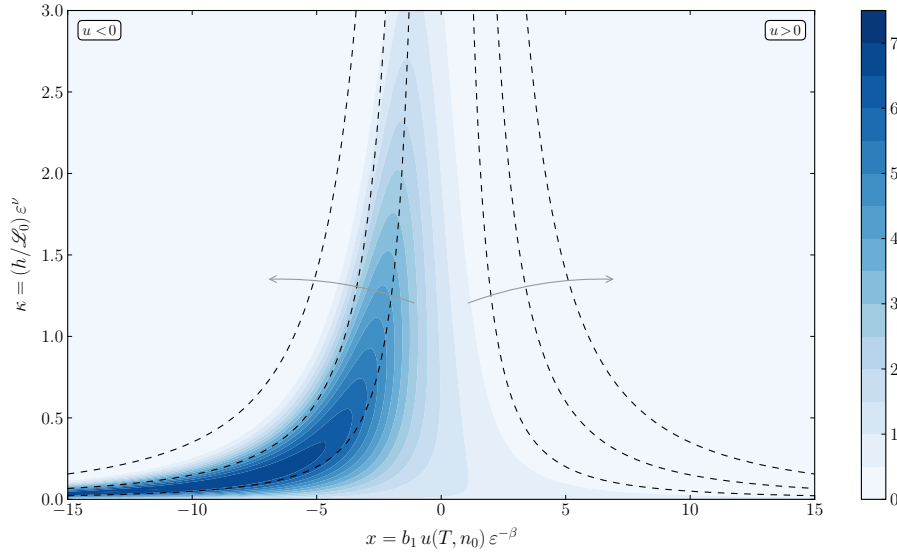

Figure 4.6: Absolute value of the scaling function $\Theta^{\circ}_{++}(\kappa; x)$ plotted in the x, κ plane as a pseudo-color map. The function is negative in the whole plane. The dashed lines define thermodynamic paths at constant u and h (the arrows indicate the direction of increasing $|u|$ or h). The same plot applies to $\Theta^{\circ}_{--}(\kappa; -x)$.

where $\Theta^\circ_{\mathcal{B}}$ is a universal scaling function governing the critical Casimir interaction of two equal-sized spheres, given explicitly by

$$\Theta^\circ_{\mathcal{B}}(\kappa; x) \doteq \pi \int_1^{+\infty} dy \left(\frac{y-1}{y^3} \right) \Theta_{\mathcal{B}}(\kappa y; x) . \tag{4.54}$$

We expect the range of the interaction to be comparable with the range h_∞ of the force F; in fact, the two are equal: by inserting the asymptotic behavior (4.51) into Equation (4.52) we obtain for large h

$$|v(h)| \sim k_{\text{B}}T \, \frac{R}{\mathscr{L}_s} \, \exp\left(-\frac{h}{h_\infty} \right) , \tag{4.55}$$

independently of the boundary conditions. It is also evident that the scaling function $\Theta^\circ_{\mathcal{B}}$, hence the interaction $v(h)$, inherit from $\Theta_{\mathcal{B}}$ the symmetry properties (4.49).

A numerical evaluation of the scaling function corresponding to symmetric boundary conditions is presented in Figure 4.5, while Figure 4.6 depicts the function as a pseudo-color map in the x, κ plane. Both plots are entirely similar to the ones holding in the planar case, hence the same considerations apply.

4.5.2 A tentative phase diagram

We now attempt, on the basis of our analysis, to make an educated guess about the stability and the phase behavior of a dispersion of colloidal spheres in a possibly critical fluid. As a starting point, we recognize that outside the critical and pre-critical regions, where density fluctuations happen on the scale of the fluid particle diameter σ, the general results we have obtained are not of much avail. This, however, is entirely due to the long-wavelength approximation (4.21) and is *not* a inherent flaw of the methods adopted. Indeed, if a free energy functional capable of handling fluctuations on the scale σ were used, a faithful description of the sphere-sphere effective interaction would be obtained even in noncritical conditions. In that regime the emerging interaction would be unambiguously ascribed to the depletion mechanism and, as such, we expect it to be attractive, with a range of the order of σ and a strength more or less proportional to the fluid bulk density n_0. If a certain bulk density $\bar{n}_0$ is exceeded, the attraction might become strong enough to drive a reversible flocculation or even a liquid-vapor phase separation of the colloidal spheres. Due to the features of the depletion interaction, we also expect the quantity $\bar{n}_0$ to be only mildly dependent on the temperature.

As the critical region is entered, density fluctuations spanning larger and larger length scales appear. From a certain point on, the spatial scale of the fluctuations becomes large enough for the long-wavelength analysis to be fully justified: accordingly, the effective interaction acquires an exponentially-damped tail complying with the universal asymptotic form (4.55). At small sphere-to-sphere separation the interaction remains non-universal and retains the character of a depletion attraction due to the ever-present correlations on the scale of the diameter σ. Since symmetric boundary conditions apply, the tail of the interaction induced by critical fluctuations is attractive as well; moreover, we see from Figure 4.6 that it is particularly enhanced on one side of the line $\bar{n}(T)$ ending at the critical point. The exact side on which this happens depends on the sign of the boundary conditions: with a minimum of foresight for the comparison to be made with the experiment, we assume the boundaries to be of the $--$ kind.[§] Accordingly, we expect that the region in which the attraction is

---

[§]Note that from the definition (4.29) the choice of the boundary conditions is not entirely obvious,

most effective, possibly leading to a reversible aggregation of the colloids, lies to the right of the curve $n = \bar{n}(T)$ in a density-temperature diagram. Let us stress that this region merely identifies the portion of the phase diagram of the host fluid in which the scaling function of the critical Casimir force may attain significant values, and as such does not bear a definite relation to the region in which the colloids dispersed in the fluid possibly aggregate. In other words, the locus of the points marking the onset of the reversible aggregation of the colloids does not necessarily coincide with the line $\bar{n}(T)$. In fact the actual energy of interaction of the colloids, given by Equation (4.53), is also proportional to the radius R of the particles, therefore we expect that the boundary of reversible aggregation shifts in the direction of increasing fluid density as the the radius gets smaller. The expectation is indeed borne out by the experiment of Degiorgio and collaborators already cited [34].

To summarize, our analysis suggests a scenario in which a system dependent, depletion-like regime merges continuously with a universal, Casimir-like behavior as the temperature of the suspension is varied. The crossover between the two regimes should be particularly evident if the critical density of the host fluid is significantly smaller than the bulk density $\bar{n}_0$ characterizing the onset of reversible aggregation due to pure depletion.

4.5.3 Comparison with the experiment

That is enough with the theoretical maybes and mights: we now turn to the description of the essential features of the experiment performed by Piazza and Buzzaccaro [25]. The experimental system consists in a aqueous suspension of spherical, nearly monodisperse colloidal particles with an average radius $R \approx 90$ nm made of the Hyflon® MFA fluoropolymer. The surface of the particles bears a negative charge, mostly acquired during the process of synthesis: to screen any spurious electrostatic effect, a sufficient amount of salt was added to the suspension after the particles had been sterically stabilized. The nonionic surfactant $C_{12}E_8$ (octaethylene glycol monododecyl ether) was used as a depletion agent. Beyond its critical micellar concentration, $C_{12}E_8$ forms globular micelles with a diameter $\sigma \approx 7$ nm, nearly independent of temperature in a broad temperature range including, of course, the one experimentally investigated; the colloid-micelle size ratio is therefore $2R/\sigma \approx 25$. Most interestingly, aqueous solutions of $C_{12}E_8$ display a critical behavior, since they possess an inverted miscibility gap bounded below by a critical demixing point corresponding to a temperature $T_c \approx 64.5°C$. Liquid-liquid phase separation by increasing temperature is not a uncommon feature, for it is shared by many simple mixtures as lutidine or isobutyric acid in water. Compared to the latter, however, two aspects of the phase behavior of $C_{12}E_8$ are rather peculiar: first, the temperature region where critical effects can be detected is very wide, ranging in the tens of degrees, which is more than an order of magnitude larger than for simple binary mixtures; second, the critical concentration is very small, of the order of 2% in weight fraction, so that the demixing region is very asymmetrical. Both features are particularly suited to check the predictions of our theoretical analysis.

All experiments were performed in sterically-stabilized MFA suspensions at a particle volume fraction $\Phi = 0.03$, in water + 250 mM NaCl, to which a variable amount of $C_{12}E_8$ was added. The samples were sealed in glass ampoules with a volume of

---

since they are not directly related to a physical feature of the wall-particle interaction, but instead represent an extrapolation to the surface of the walls of the equilibrium density profile. Nonetheless, we expect that $--$ boundary conditions would correspond to colloidal spheres that in some sense repel the particles of the fluid.
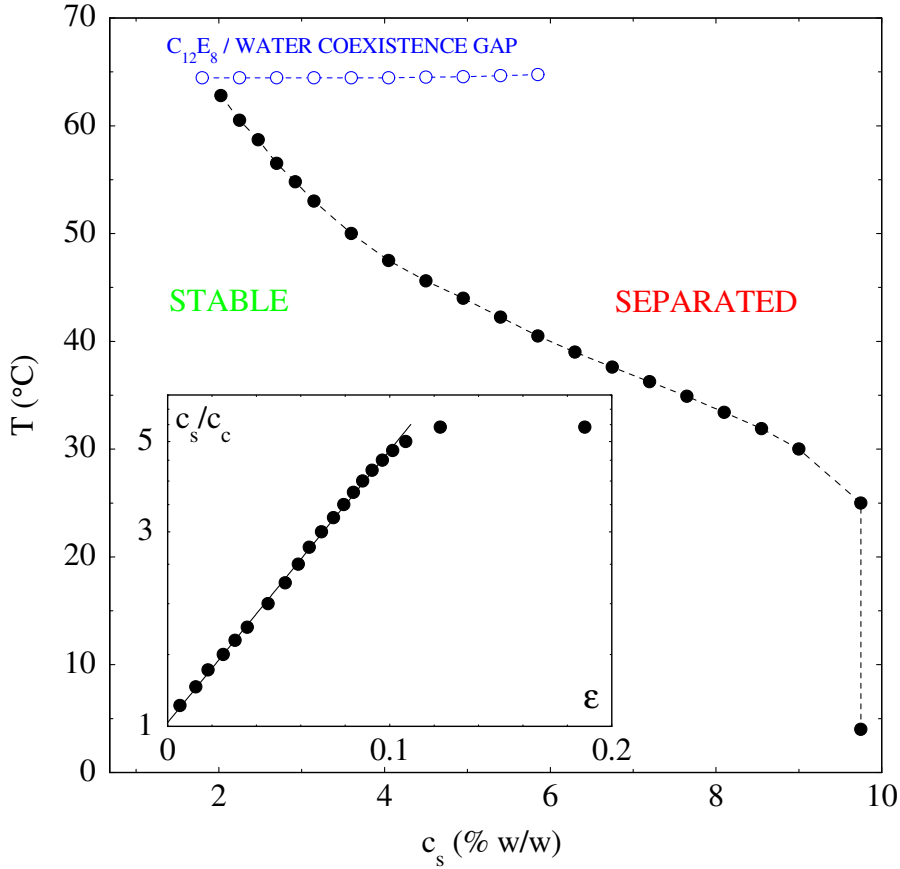
Figure 4.7: Minimum amount of surfactant c_s required to induce phase separation for aqueous MFA suspensions at particle volume fraction $\Phi = 0.03$ (full dots), in the presence of 250 mM NaCl. The consolution curve of the surfactant solution is shown by open dots. The inset shows c_s/c_c versus the reduced temperature ϵ on a semi-log scale, with a fit to the data. Reproduced from Ref. [25].

1 cc, mounted in parallel on a frame, and immersed in a water thermostat with a temperature setting accuracy $\pm 0.02°C$, with a window allowing for optical inspection. The temperature was increased in small steps (in practice as small as $0.1°C$), and the system was let thermalize for at least ten minutes between each temperature step. For each sample a well-defined temperature $\bar{T}$, thus dependent on the amount of surfactant added, could be identified above which a noticeable increase of turbidity of the suspension took place, followed on the time scale of a few minutes by the appearance of a settling meniscus. The process was entirely reversible: each sample returned to a homogeneous state as soon as the temperature was lowered again beyond the particular value $\bar{T}$. The phenomenon can be interpreted as a liquid-vapor phase separation process driven by a spinodal instability due to emerging attractive interactions among the colloidal particles. The same turbidimetric method was also used to find the demixing line (or, more precisely, the cloud-point curve) of the $C_{12}E_8$/brine system in the absence of particles; care was taken to check that the latter is not shifted by the presence of the colloids, at least up to a particle volume fraction of $\Phi = 0.05$.

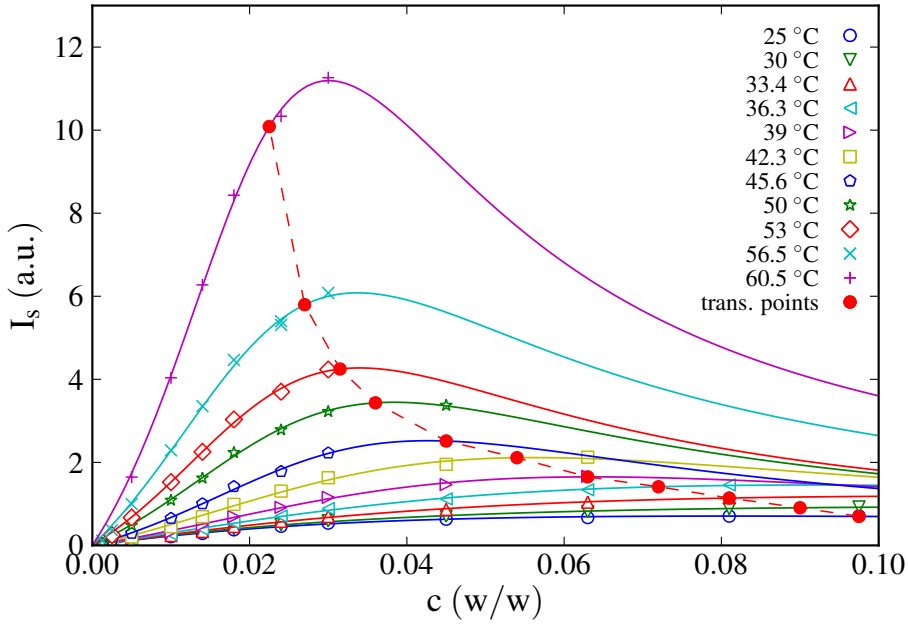The locus of the experimentally measured transition points, shown in Figure 4.7,

Figure 4.8: Intensity scattered by $C_{12}E_8$ solutions at various temperatures, shown in the legend, compared to the locus of the colloid transition points. The intensity is proportional to the isothermal susceptibility χ_T of the solution. Full lines are quadratic fits of c/I_s. Reproduced from Ref. [25].

is indeed consistent with the hypothetical scenario we prefigured. In noncritical conditions the minimum surfactant concentration beyond which reversible aggregation of the colloidal particles takes place is nearly independent of temperature. As the critical region is entered, the threshold concentration diminishes, signalling an enhancement in the sphere-sphere attractive interaction; at the same time, the locus of transition points bends, following a path that ends close to the $C_{12}E_8$/water critical point. The light scattering measurements depicted in Figure 4.8 also show that this path bears a relation to the locus of maxima of the isothermal susceptibility. From the pattern of the scattered intensity, the correlation length of the surfactant solution could also be determined: in the whole range of temperatures investigated, it does not exceed a 15% fraction of the colloid radius, therefore the Derjaguin approximation (4.52) underlying the derivation of our theoretical scenario is fully justified.

4.6 CONCLUSIONS

We hope to have provided in this chapter solid arguments in favor of a unitary view of the depletion interaction and the critical Casimir effect. Indeed, the two have the same physical origin, that is the confinement of a fluid between a pair of surfaces, and can also be described using a common formalism, namely density functional theory. In particular, we have shown that if the adopted free energy functional correctly incorporates the critical behavior of the host fluid, then the fluid-mediated interaction between the two surfaces, which has a range proportional to the fluid correlation length, naturally acquires in the critical region the universal scaling form typical of

the critical Casimir effect. The density functional formalism is also apt to describe correlations on the scale of the fluid particle diameter, leading in noncritical regime to the well-known and much studied depletion interaction. Our analysis suggests that depletion and critical Casimir phenomena are two ends of a continuum: the former potentially transforms into the latter as the thermodynamic state of the host fluid is varied. This view is supported by indirect experimental evidence involving the reversible aggregation of colloidal spheres.

What is lacking at the moment is a truly microscopic approach capable of a quantitative description of both regimes. Indeed, in this preliminary proof-of-concept study with the adoption of the long-wavelength approximation we gave up any chance of a faithful description at short wall-to-wall distance in favor of a simple expression holding in the critical regime. The use of a more realistic free energy functional that would eventually lead to a quantitative phase diagram to be compared with the experimental results is highly desirable. An extension to the fully critical regime that goes beyond the Derjaguin approximation, thus allowing the correlation length to become comparable with or even larger than the colloid radius, would also be extremely interesting, as well as challenging.

5

Effect of quenched size polydispersity on the fluid-solid transition in charged colloidal dispersions

ABSTRACT

We perform Monte Carlo simulations to study the effect of quenched size polydispersity on the freezing transition in charged colloidal dispersions, modeled as repulsive hard-core Yukawa fluids. The goal is to ascertain whether, and how, a sufficient amount of polydispersity suppresses the crystalline phase in favor of an amorphous solid. Two main assumptions are made: (i) the particle surface potential is taken as a constant, so that size polydispersity entails charge polydispersity; (ii) the particle size distribution is shared by the fluid and the crystal, that is no particle fractionation takes place. We perform several free energy calculations, investigating different combinations of screening length and surface potential. A consistent pattern emerges: upon increasing the polydispersity, the freezing transition shifts towards higher packing fractions and the density gap between the fluid and the solid diminishes. Our results support the existence of a terminal polydispersity above which the freezing transition disappears, and also confirm the phenomenon of reentrant melting.

T HE discovery that a system of hard spheres undergoes a first-order freezing transition is undoubtedly one of the milestones of computer simulation applied to statistical mechanics. In the mid-1950s the existence of such a transition was an important open question, and no convincing answer could be given starting from first principles. Therefore, it was no surprise that at a symposium held in 1957 at the Stevens Institute of Technology in Hoboken, New Jersey, during a discussion led by G. E. Ulhenbeck a vote on this question taken among prominent scientists, including several Nobel laureates, ended in a draw [103]. The hesitation of half of the audience is understandable, because the fact that purely repulsive particles can form a stable crystal is far from obvious. The question was finally settled in favor of the existence of a fluid-crystal transition thanks to the seminal molecular dynamics simulations by Alder and Wainwright [2] and Monte Carlo simulations by Wood and Jacobson [146], as well as the later and conclusive Monte Carlo study by Hoover and Ree [62]. In more recent years, owing to notable advances in the synthesis of colloidal particles, the existence of the phase transition has also been confirmed by extensive experimental evidence: starting with the classic investigation of Pusey and van Megen [111], beautiful hard-sphere crystals have been produced and imaged countless times.

It is now widely accepted that excluded-volume interactions and repulsive short-range forces play a major role in determining the existence of a freezing transition: indeed, the latter is found in the high-density end of the phase diagram of most systems containing particles with a core. This is the case, for example, of hard-core repulsive Yukawa fluids – a widely-adopted model for charge-stabilized colloidal dispersions – whose phase behavior has been extensively investigated by means of Monte Carlo simulation by Hynninen and Dijkstra [65]. They considered several combinations of the amplitude and range of the Yukawa tail, and found that a crystalline solid phase always exists beyond a certain density. The parameters of the potential affect not only the location of the phase transition, which generally takes place at a density lower than the one typical of hard spheres, but also the lattice structure of the crystal, which can be either face-centered cubic (FCC) or body-centered cubic (BCC). Their results provide a useful guide to experimentalists trying to achieve the tunable self-assembly of charged particles into colloidal crystals.

A feature of colloidal dispersions that is not considered in the aforementioned models is *polydispersity*, namely the fact that in real systems the particles are not identical but instead show a degree of stochastic variation in one or more properties (for instance size, shape or charge). That polydispersity might have a deep impact on the freezing transition is intuitive, since the very idea of a periodic, regular lattice is somewhat at odds with a random variation in any property of the particles. Indeed, polydisperse system usually have different – and richer – phase diagrams if compared to their monodisperse counterparts [127]. While a small degree of polydispersity is expected to introduce a mere distortion in the phase boundaries, leaving the topology of the phase diagram largely unaffected, higher degrees of polydispersity might significantly change the phase behavior of the system, giving birth to new phases or suppressing existing phase transitions. In this regard, a clear distinction should be made between the general case and the case we will address, namely the one of *quenched polydispersity*.

In order to elucidate this point, let us focus on the freezing transition of a fluid whose particles are polydisperse in size. The composition of the system is quantified by a size distribution function, which determines the probability that any given particle has a certain diameter. The latter is also known as the *parent* size distribution, since it characterizes the composition of the whole system regardless of its phase behavior. If

the system undergoes a freezing transition, so that it separates into a fluid and a solid, a *daughter* size distribution can be associated with each phase. In a general scenario, there is no reason for the two daughters to be the same, nor they have to match the parent distribution. For instance, on general grounds one expects the size distribution of the solid to be narrower than the one of the fluid. However, for this to happen a possibly substantial redistribution of the particles – called particle fractionation in this context – must take place within the system during the phase transition. If this is not possible, be it because particle diffusion is too low or because the dynamics of the system slow down with the ongoing phase transition, then fractionation cannot reach completion on experimentally-accessible timescales. The limiting case is the one corresponding to a sudden quench of the system, that completely inhibits particle fractionation: accordingly, the two daughter distributions are necessarily equal and perfectly match the parent. We refer to this scenario with the expression *quenched polydispersity.*

The phase behavior of polydisperse hard spheres, the cleanest polydisperse system in which to study the freezing transition, has been the subject of extensive investigation in the literature. One of the main questions addressed concerns the existence of a terminal polydispersity above which no stable crystal can exist. Experimentally, the freezing transition is indeed suppressed in sufficiently polydisperse systems [112, 110]; however, the situation is somewhat ambiguous, since the observed behavior might also be a nonequilibrium effect due to a kinetic glass transition. This prompted a substantial amount of theoretical [90, 10, 13, 11, 12, 125, 44] and computational [113, 144, 145, 104, 23, 71] work devoted to the determination of an accurate equilibrium phase diagram for polydisperse hard spheres.

Conversely, to the best of our knowledge no similar effort has been devoted to polydisperse hard-core Yukawa fluids, a fact that motivates the present work. Therefore, in this chapter we plan to: (i) elucidate the effect of polydispersity on the liquid-solid phase boundary, and its dependence on the parameters of the Yukawa tail; (ii) ascertain the existence of a terminal polydispersity above which the crystal phase is suppressed in favor of a glassy-like state; (iii) check whether the phenomenon of reentrant melting predicted for hard spheres [13] takes place. We tackle the problem by performing free energy calculations via Monte Carlo simulation, which allows us to map out the phase boundaries. We will consider only the case of quenched polydispersity, since it is far easier to deal with but still retains a fair degree of practical relevance. This crucial assumption must be stressed from the outset, since allowing particle fractionation would surely invalidate our results.

5.1   MODEL SYSTEM

We consider a system of N spherical particles, polydisperse in size, enclosed in a cubic box of volume V. Let $\boldsymbol{r}_i$ denote the spatial coordinate of particle i, and let σ_i and $a_i = \sigma_i/2$ be its diameter and radius, respectively. The energy of the system is taken as pairwise additive, with a pair potential $v_{ij}(r)$ comprising a hard core plus a repulsive Yukawa tail:

$$
v_{ij}(r) \;=\; \begin{cases} +\infty & \text{when } r \le a_i + a_j\,, \\[2mm] \epsilon_{ij}\,\dfrac{\exp\left[-\kappa(r - a_i - a_j)\right]}{r/(a_i + a_j)} & \text{otherwise}\,, \end{cases} \tag{5.1}
$$

where $r = |\boldsymbol{r}_i - \boldsymbol{r}_j|$ is the distance between the centers of particles i and j, and κ is the inverse screening length setting the decay rate of the Yukawa tail. The contact value ϵ_{ij} of the pair potential is given in the context of the standard Derjaguin, Landau,

Verwey and Overbeek (DLVO) theory by [96]

$$\beta \epsilon_{ij} = \frac{Z_i Z_j}{(1 + \kappa a_i)(1 + \kappa a_j)} \frac{l_{\mathrm{B}}}{a_i + a_j} \,, \tag{5.2}$$

where $\beta = 1/(k_{\mathrm{B}}T)$, with k_{B} Boltzmann's constant and T the temperature, is the inverse thermal energy; Z_i and Z_j are the number charges of the two particles, expressed in units of the elementary charge; $l_{\mathrm{B}} = \beta e^2 / \varepsilon$, with ε the dielectric constant of the solvent and e the elementary charge, is the Bjerrum length.

Due both to the process of particle synthesis and to the attainment of local chemical equilibrium in the suspension, the amount of charge attached to the surface of a particle depends in general on the particle size: in other words, size polydispersity entails charge polydispersity. The simplest hypothesis is to assume a constant surface charge density, so that the charge is proportional to the surface area of the particle. Another important condition, which is often met in real colloidal dispersions and therefore will be adopted in the following, is the one of *constant surface potential*, which amounts to assume that the electrostatic potential on the surface of a particle is independent of its size and a constant throughout the system. In the context of linear Poisson-Boltzmann theory, which underlies the derivation of the screened Coulomb part in the standard DLVO potential (5.1), the electrostatic potential Ψ_i on the surface of a single, isolated particle embedded in the electrolyte satisfies the relation [96]

$$\frac{\Psi_i}{\beta e} = \frac{Z_i}{1 + \kappa a_i} \frac{l_{\mathrm{B}}}{a_i} \,. \tag{5.3}$$

If the electrostatic potential is taken as a constant, that is $\Psi_i \equiv \Psi$ independent of particle number i, Equations (5.2) and (5.3) imply

$$\epsilon_{ij} \ \propto \ \frac{a_i a_j}{a_i + a_j} \,, \tag{5.4}$$

the constant of proportionality being the same for all pairs. If, moreover, we choose a reference particle diameter $\bar{\sigma}$ and call $\bar{\epsilon}$ the contact value for the pair interaction of two particles with reference size $\bar{\sigma}$, we can express the pair interaction of any two particles in the system in the following way:

$$v_{ij}(r) \ = \ \begin{cases} +\infty & \text{when } r \leq a_i + a_j \,, \\ \bar{\epsilon} \left(\dfrac{\sigma_i \sigma_j}{\bar{\sigma}} \right) \dfrac{\exp\left[-\kappa(r - a_i - a_j)\right]}{r} & \text{otherwise} \,. \end{cases} \tag{5.5}$$

This will be taken as the final expression defining the energy of the system, being conveniently characterized by the two parameters $\bar{\epsilon}$ and κ, as well as the reference particle diameter $\bar{\sigma}$.

In order to make contact with the experiments, one can also show from Equations (5.2) and (5.3) that

$$\beta \bar{\epsilon} = (\beta e \Psi)^2 \frac{\bar{\sigma}}{4 l_{\mathrm{B}}} \,; \tag{5.6}$$

typical values for a colloid in a low dielectric solvent at room temperature are [118] $\Psi = 25\mathrm{mV}$, $l_{\mathrm{B}}/\bar{\sigma} = 0.01$, which corresponds to $\beta \bar{\epsilon} \approx 20$.

Size polydispersity

We denote the parent size distribution function by $\mathbb{P}(\cdot)$, and normalize it to unity, so that the number of particles in the whole system with a diameter lying between σ and $\sigma + d\sigma$ is $N\mathbb{P}(\sigma)d\sigma$.* As is customary, we also define an index of polydispersity p as the ratio between the standard deviation and the mean of the distribution:

$$p \doteq \frac{\sqrt{\mathrm{E}(\sigma^2) - (\mathrm{E}(\sigma))^2}}{\mathrm{E}(\sigma)}\,, \qquad \text{with} \quad \mathrm{E}(\bullet) = \int_0^{+\infty} d\sigma \bullet \mathbb{P}(\sigma)\,. \tag{5.7}$$

In the following, we assume that the parent distribution has a log-normal form, with a mean equal to the reference particle diameter $\bar{\sigma}$:

$$\mathbb{P}(\sigma) = \frac{1}{z\sqrt{2\pi}\,\sigma}\,\exp\left[-\frac{(\log(\sigma/\bar{\sigma}) + z^2/2)^2}{2z^2}\right]\,, \qquad z = \sqrt{\log(1 + p^2)}\,. \tag{5.8}$$

No particular reason supports this choice; viable alternatives, also found in the literature, include top-hat, triangular and gamma distributions. However, once the polydispersity index p is fixed we expect the results to depend not too markedly on the shape of the parent distribution, although we did *not* test this hypothesis.

If phase separation into a fluid (F) and a solid (S) occurs, then to each phase $\phi \in \{\mathrm{F}, \mathrm{S}\}$ a daughter size distribution $d_\phi(\cdot)$ is associated, also normalized to unity, such that $N_\phi d_\phi(\sigma)d\sigma$ is the number of particles with a diameter lying between σ and $\sigma + d\sigma$ belonging to that phase, the total number of particles in the phase being N_ϕ. The daughter and parent distributions are not independent: conservation of the number of particles requires that

$$N_\mathrm{F} d_\mathrm{F}(\cdot) + N_\mathrm{S} d_\mathrm{S}(\cdot) = N\mathbb{P}(\cdot)\,. \tag{5.9}$$

The constraint of quenched polydispersity imposes a much stronger condition, forcing both daughters to match the parent:

$$d_\mathrm{F}(\cdot) = d_\mathrm{S}(\cdot) = \mathbb{P}(\cdot)\,; \tag{5.10}$$

in this particular case, Equation (5.9) is trivially satisfied.

5.2 REMINDER ON POLYDISPERSE PHASE EQUILIBRIA

In a polydisperse system, the definition of the various thermodynamic potentials and the conditions for two-phase equilibrium are far more complex than the ones valid in a monodisperse system. However, the constraint of quenched polydispersity introduces a substantial simplification, that enables the problem to be approached with the same methods usually applied to one-component fluids. We first review the general case, loosely following Ref. [120], then we specialize the results to the case of quenched polydispersity.

A polydisperse system can be considered a generalization of a multicomponent mixture; when going from a finite number of components to an infinite one, however, several subtleties arise and care must be taken to properly define thermodynamic quantities. The Helmholtz free energy of a homogeneous mixture with m components is a function of the temperature T, the volume V, and the number of particles of the various species $N_1, N_2, \ldots, N_m$. In the limit of an infinite number of species the set of

---

*Here and in the following, we adopt the convention whereby $f(\cdot)$ denotes a function as a whole, while $f(x)$ is the value of the function corresponding to an argument x.

particle numbers is replaced by the product $N\zeta(\sigma)$, where N is the total number of particles and $\zeta(\cdot)$ the size distribution function.[†] Therefore, the Helmholtz free energy of a polydisperse homogeneous system is a functional of the term $N\zeta(\cdot)$ and has the form

$$\mathscr{F}\left(T, V ; N\zeta(\cdot)\right). \tag{5.11}$$

The pressure is related to the free energy by the usual thermodynamic identity

$$\mathscr{P}\left(T, \rho ; \zeta(\cdot)\right) = -\frac{\partial \mathscr{F}}{\partial V}, \tag{5.12}$$

where $\rho = N/V$ is the particle number density, while the chemical potential is defined by means of a functional derivative:

$$\mathscr{M}\left(T, \rho, \sigma ; \zeta(\cdot)\right) = \frac{\delta \mathscr{F}}{\delta[N\zeta(\sigma)]}. \tag{5.13}$$

Note that the chemical potential is a function of the particle diameter: in the case of a finite mixture, this corresponds to associating a chemical potential to each species.

If the system, at fixed temperature T, departs from homogeneity separating into a liquid and a solid, the conditions for mechanical and chemical equilibrium between the two phases read as follows [120]:

$$\mathscr{P}\left(T, \rho_{\mathrm{F}} ; d_{\mathrm{F}}(\cdot)\right) = \mathscr{P}\left(T, \rho_{\mathrm{S}} ; d_{\mathrm{S}}(\cdot)\right), \tag{5.14a}$$

$$\mathscr{M}\left(T, \rho_{\mathrm{F}}, \sigma ; d_{\mathrm{F}}(\cdot)\right) = \mathscr{M}\left(T, \rho_{\mathrm{S}}, \sigma ; d_{\mathrm{S}}(\cdot)\right) \quad \text{for all } \sigma. \tag{5.14b}$$

The previous equations, when supplemented with the conservation of particle numbers (5.9), form the thermodynamic basis for studying two-phase equilibrium in a polydisperse system.

A substantial simplification arises if the constraint of quenched polydispersity (5.10) is imposed: since the size distribution function is fixed, the Helmholtz free energy reverts to a function of temperature, volume and number of particles:

$$F(T, V, N) \doteq \mathscr{F}\left(T, V ; N\mathbb{P}(\cdot)\right). \tag{5.15}$$

Similarly, the dependence on $\zeta(\sigma)$ drops out for the pressure

$$P(T, \rho) \doteq -\frac{\partial F}{\partial V} = \mathscr{P}\left(T, \rho ; \mathbb{P}(\cdot)\right) \tag{5.16}$$

and the definition of the chemical potential for a monodisperse system is recovered:

$$\mu(T, \rho) \doteq \frac{\partial F}{\partial N} = \int d\sigma\, \mathbb{P}(\sigma)\, \mathscr{M}\left(T, \rho, \sigma ; \mathbb{P}(\cdot)\right). \tag{5.17}$$

Finally, the conditions for two-phase equilibrium (5.14) acquire the simple form

$$P(T, \rho_{\mathrm{F}}) = P(T, \rho_{\mathrm{S}}), \tag{5.18a}$$

$$\mu(T, \rho_{\mathrm{F}}) = \mu(T, \rho_{\mathrm{S}}). \tag{5.18b}$$

Owing to these simplifications, in the quenched case a standard common tangent construction [28] applied to the Helmholtz free energy (5.15) suffices to locate the liquid-solid phase boundary.

[†]The symbol $\zeta(\cdot)$ denotes a generic size distribution function, not to be identified with the already introduced parent and daughter distributions.

5.3 METHODS

We now devise a strategy to compute the quenched free energy (5.15) using Monte Carlo simulation. Before describing the details of the method, we briefly consider the question concerning the sampling of size polydispersity during a computer simulation. Indeed, the free energy of a polydisperse system with size distribution $\zeta(\cdot)$ is a well-defined quantity only in the thermodynamic limit: in any finite system the free energy depends on the particular set of particle diameters considered, especially so if the size of the system in not very large. We call every finite set of particle diameters drawn in accordance to the probability measure $\mathbb{P}(\cdot)$ a *realization* of the polydisperse system. In order to deal with the finite extent of the system inherent to any Monte Carlo simulation, at least two strategies are viable: either we explore different realizations in the course of a single simulation – for instance devising moves that modify the size of the particles – or we perform a number of different simulations corresponding to independent realizations and then average the results a posteriori. In this chapter we pursue the second approach: for it to be effective, the size of the system and the number of different realizations considered must be balanced in order to ensure a good sampling of the size distribution $\mathbb{P}(\cdot)$.

5.3.1 A number of thermodynamic relations

Since free energy calculations are notoriously a time-demanding task, the number of direct evaluations should be kept to a minimum. Ideally, at fixed temperature only one such evaluation is needed, since the density dependence of the free energy is entirely determined given (i) the value of the free energy at a freely-selected reference density, and (ii) the equation of state of the system, in the form of pressure as a function of density. Indeed, upon defining the dimensionless free energy per particle

$$a(T, \rho) \doteq \frac{\beta F(T, V, N)}{N} \,, \tag{5.19}$$

it readily follows from Equation (5.16) that

$$a(T, \rho) = a(T, \bar{\rho}) + \int_{\bar{\rho}}^{\rho} d\varrho \, \frac{\beta P(T, \varrho)}{\varrho^2} \tag{5.20}$$

for any given temperature T and reference density $\bar{\rho}$. The previous expression contains, in the low-density limit, a logarithmic singularity arising from the ideal gas contribution. For numerical convenience, we split the free energy density in the sum of an ideal term and an excess term:

$$a(T, \rho) = a^{\text{id}}(T, \rho) + a^{\text{ex}}(T, \rho) \,, \tag{5.21}$$

and consider the excess version of Equation (5.20):

$$a^{\text{ex}}(T, \rho) = a^{\text{ex}}(T, \bar{\rho}) + \int_{\bar{\rho}}^{\rho} d\varrho \, \frac{\beta P(T, \varrho) - \varrho}{\varrho^2} \,, \tag{5.22}$$

which is now free from singularities.

The ideal gas term, required to compute the full free energy, is known analytically: for a generic polydisperse system with size distribution function $\zeta(\cdot)$ it equals [120]

$$\frac{\beta \mathscr{F}^{\text{id}}\left(T, V; N\zeta(\cdot)\right)}{N} = \int d\sigma \, \zeta(\sigma) \left\{ \log \left[\rho \, \zeta(\sigma) \left(\Lambda(\sigma) \right)^3 \right] - 1 \right\} \,, \tag{5.23}$$

where $\Lambda(\sigma)$ is the thermal de Broglie wavelength for particles with diameter σ. Defining an effective thermal wavelength $\bar{\Lambda}$ – or, which is the same, an effective particle mass $\bar{m}$ – according to

$$\log \bar{\Lambda} \doteq \int d\sigma\, \zeta(\sigma)\, \log\left[\Lambda(\sigma)\right] , \tag{5.24}$$

Equation (5.23) can be cast in the suggestive form

$$\frac{\beta\mathscr{F}^{\mathrm{id}}}{N} = \log(\rho\bar{\Lambda}^3) - 1 + \int d\sigma\, \zeta(\sigma)\, \log\left[\zeta(\sigma)\right] . \tag{5.25}$$

In other words, the free energy density of a polydisperse ideal gas is equal to the free energy density of a monodisperse ideal gas comprising particles with an effective mass $\bar{m}$, plus a mixing term involving the distribution function $\zeta(\cdot)$. Specializing the previous expression for the parent distribution $\mathbb{P}(\cdot)$, we get the ideal gas free energy appearing in Equation (5.21):

$$a^{\mathrm{id}}(T,\rho) = \log(\rho\bar{\Lambda}^3) - 1 + \int d\sigma\, \mathbb{P}(\sigma)\, \log\left[\mathbb{P}(\sigma)\right] . \tag{5.26}$$

Note that in the case of quenched polydispersity the mixing term, being a constant independent of density, plays no role in a two-phase equilibrium.[‡] Since the thermal wavelength $\bar{\Lambda}$ also contributes a simple additive constant, phase equilibrium is not even affected by the mass of the particles.

5.3.2 Fluid and solid free energy

Unless very special methods are adopted to overcome free energy barriers, fluid-like and solid-like configurations cannot both be visited in the course of a single Monte Carlo run. As a consequence, the equation of state cannot be computed as a whole: depending on the initial configuration, either the fluid branch P_{F} or the solid branch P_{S} is sampled. The two branches are in fact disjoint and extend in metastable regions of the phase diagram. Each branch of the equation of state determines a corresponding branch of the free energy – $a_{\mathrm{F}}(T,\rho)$ or $a_{\mathrm{S}}(T,\rho)$.

In the fluid phase the dilute limit, where the excess contribution to the free energy vanishes, can be reached from any density without incurring phase transitions; according to Equation (5.22) the entire branch of the free energy is then determined by the equation of state alone:

$$a_{\mathrm{F}}^{\mathrm{ex}}(T,\rho) = \int_0^\rho d\varrho\, \frac{\beta P_{\mathrm{F}}(T,\varrho) - \varrho}{\varrho^2} . \tag{5.27}$$

Conversely, in the solid phase the equation of state must be supplemented with a reference free energy density $a_{\mathrm{S}}^{\mathrm{ex}}(T,\bar{\rho}_{\mathrm{S}})$:

$$a_{\mathrm{S}}^{\mathrm{ex}}(T,\rho) = a_{\mathrm{S}}^{\mathrm{ex}}(T,\bar{\rho}_{\mathrm{S}}) + \int_{\bar{\rho}_{\mathrm{S}}}^\rho d\varrho\, \frac{\beta P_{\mathrm{S}}(T,\varrho) - \varrho}{\varrho^2} . \tag{5.28}$$

In order to compute the reference term a number of approaches exist. Here we adopt the method of Frenkel and Ladd [48], also termed *Einstein integration*, which is to date the most reliable technique to compute the free energy of a solid.

[‡]If fractionation were allowed the entropy of mixing, being different in the two phases, would require explicit consideration.

The method relies on thermodynamic integration along a reversible path linking the solid of interest to the Einstein crystal – a system of non-interacting particles attached to a set of lattice sites by harmonic springs – whose free energy can be computed exactly. For particles interacting through a hard-core plus a tail, this path is constructed by introducing an auxiliary energy function U_λ, depending on a coupling parameter $\lambda \in [0, 1]$, according to the definition

$$U_\lambda(\{\boldsymbol{r}_i\}) \doteq U_{\mathrm{HS}}(\{\boldsymbol{r}_i\}) + (1 - \lambda)U_{\mathrm{tail}}(\{\boldsymbol{r}_i\}) + \lambda \frac{\alpha}{2} \sum_{i=0}^{N-1} |\boldsymbol{r}_i - \boldsymbol{R}_i|^2 . \qquad (5.29)$$

In the previous expression the terms U_{HS} and U_{tail} contain the cores and the tails, respectively, of the interparticle interactions; α is a spring constant common to all particles; $\{\boldsymbol{r}_i\}$ is the set of position vectors of the particles, and $\{\boldsymbol{R}_i\}$ the crystal lattice. When $\lambda = 0$ the system reduces to the solid of interest, while in the limit $\lambda \to 1$, provided the spring constant α is chosen high enough to render the presence of the cores immaterial, the Einstein crystal is recovered. Thermodynamic integration gives for the free energy of the solid [108]:

$$a_{\mathrm{S}}^{\mathrm{ex}}(T, \bar{\rho}_{\mathrm{S}}) = -\frac{\beta}{N} \int_0^1 d\lambda \left\langle \frac{\alpha}{2} \sum_{i=0}^{N-1} |\boldsymbol{r}_i - \boldsymbol{R}_i|^2 - U(\{\boldsymbol{r}_i\}) \right\rangle_\lambda^{\mathrm{CM}} +$$
$$- \frac{3}{2} \log \left(\frac{2\pi}{\beta\alpha} \right) - \frac{3}{2N} \log \left(\frac{\beta\alpha}{2\pi} \right) + \frac{\log \bar{\rho}_{\mathrm{S}}}{N} - \frac{2 \log N}{N} - \log \bar{\rho}_{\mathrm{S}} + 1 - \frac{\log 2\pi}{2N} ,$$
$$(5.30)$$

where the notation $\langle \cdot \rangle_\lambda^{\mathrm{CM}}$ stands for the average value of a quantity in the NVT ensemble with interaction energy U_λ and the constraint of fixed center of mass.[§] The free energy computed according to Equation (5.30) is subject to finite-size effects decaying as N^{-1}: to properly deal with this issue, one usually repeats the calculation varying the number of particles and then extrapolates the result to the thermodynamic limit [48, 108]. In this work we instead stick with a single calculation, relying on a large system size, already required to properly account for particle polydispersity, to reduce the spurious effects.

5.3.3   Algorithm

We now state the procedure used to map out the phase boundaries. First, we set the parameters of the pair potential (5.5), choosing the dimensionless contact value $\beta\epsilon$ and the inverse screening length $\kappa\bar{\sigma}$, and the total number of particles N. Moreover, we choose a lattice structure for the polydisperse crystal – typically, we select the structure of the solid coexisting with the fluid in the monodisperse case, the interparticle potential being equal – and a density $\bar{\rho}_{\mathrm{S}}$ for the reference free energy evaluation. Then, for each value of the polydispersity index p we consider, n_r realizations of the system are constructed by drawing random diameters from the log-normal distribution (5.8). The particles are initially arranged with a density $\bar{\rho}_{\mathrm{S}}$ on a regular lattice having the pre-selected structure: this is achieved by trial and error, positioning the particles one after another at the sites of the lattice as the random diameters are

---

[§]The constraint prevents a global translational motion of the crystal, so that the particles do not drift away from the crystal lattice. To implement the constraint in a polydisperse system no information on the mass of the particles is required, since as Equation (5.25) shows a common effective mass $\bar{m}$, which eventually cancels out, can be assigned to each particle.

being drawn; as soon as an overlap occurs, the whole procedure is restarted from the very beginning, so that the distribution $\mathbb{P}(\cdot)$ is not biased. The procedure becomes inefficient as p and $\bar{\rho}_{\mathrm{s}}$ grow, to the point that beyond a certain limit the polydisperse crystal cannot be constructed in reasonable time. Nevertheless, we could not devise a better algorithm.

Einstein integration is performed on the initial configuration to get the solid free energy at the reference density. We use the same configuration to start to computation of the solid branch of the equation of state, and, after melting the crystal, of the fluid branch. Once all realizations of the polydisperse system have been processed, we take averages over the different outcomes.[¶] Finally, we evaluate the fluid and solid excess free energy by means of Equation (5.27) and (5.22), respectively, and determine the density of the coexisting phases by imposing the conditions of two-phase equilibrium (5.18). The conversion between density and packing fraction is performed at the end of the whole procedure by using the actual mean volume of the particles computed over the different realizations.

5.3.4   Technical details

All the simulations are carried out in a cubic box with periodic boundary conditions and the minimum image convention; the number of particles is chosen so that in the solid phase an integer number of primitive lattice cells fits into the box. A spherical cutoff is applied to the the pair potential (5.5); the cutoff radius r_c is set beforehand and kept constant during the course of a simulation: care is taken to ensure that it never exceeds half of the box length. No tail correction is applied to compensate for the cutoff: on the one hand, the exponential decay of the potential makes the correction negligible if r_c is chosen high enough;[‖] on the other hand, polydispersity renders the actual evaluation of the correction difficult.

Equations of state are computed by means of simulations in the *NPT* ensemble. For a single branch several tens of points are sampled, and later interpolated by the virial expansion

$$\frac{\beta P(T,\rho) - \rho}{\rho^2} = \sum_{j=0}^{M} b_j \rho^j \,, \tag{5.31}$$

with fitting coefficients $\{b_j\}$ and a degree $M \lesssim 10$.

To compute the reference solid free energy within the Frenkel-Ladd method, the integral figuring in Equation (5.30) is evaluated by a numerical quadrature rule using a total of thirty nodes. We divide the interval spanned by λ in the two sub-intervals $[0 - 0.2)$ and $[0.2, 1.0]$, and apply to each one the 15-7 Gauss-Kronrod rule [101, 106], which has the advantage over the commonly used Legendre rule of providing an estimate of the error in the result. The rationale behind the splitting is that the integrand is steeper near the left end of the interval, where the springs are less effective in confining the particles close to the lattice sites, therefore it is convenient to concentrate the quadrature nodes in that region. No definite recipe exists to select the value of the spring constant α: we set it just high enough to allow the non-interacting regime to be reached when $\lambda = 1$, a fact that we judge by comparing the average value of the internal energy with the value expected for the harmonic potential of the springs on

---

[¶]More precisely: to compute the equations of state we perform simulations at fixed pressure and average the resulting volumes; in the case of the Einstein integration we average the excess solid free energies.

[‖]Typically, we set r_c so that the pair potential is less than $10^{-5}k_{\mathrm{B}}T$ at the cutoff.

Id	$\beta\epsilon$	$\kappa\bar{\sigma}$	$r_c/\bar{\sigma}$	Lattice	η_s^0	N	n_r	$\beta\alpha\bar{\sigma}^2$	$p_{\max}$
A	20	10	3.0	FCC	0.29	5324	5	4000	0.095
B	81	10/3	5.0	BCC	0.108	4394	5	4000	0.125
C	20	10/3	4.0	BCC	0.28	4394	5	4000	0.100
D	1200	0.7	20.0	BCC	0.0029	4394	5	100	0.220

Table 5.1: Summary of the parameters characterizing the four different model systems that have been simulated. From left to right: identifier of the model; dimensionless contact value, inverse screening length and cutoff radius of the pair potential; lattice structure and packing fraction of the crystalline solid coexisting with the fluid in the monodisperse case (for systems A-C the estimate is based on the phase diagrams found in [65]; for system D the mapping of the hard-core Yukawa model onto the point Yukawa model devised in the same article has been applied); number of particles; number of realizations per polydispersity value over which averages were taken; dimensionless spring constant of the Einstein crystal; maximum value of the polydispersity for which fluid-solid coexistence could be determined.

the basis of the equipartition theorem.[**]

The conditions of two-phase equilibrium (5.18) are handled by standard solvers of nonlinear equations: the chemical potential μ is computed without performing derivatives by means of the thermodynamic identity

$$\beta\mu(T,\rho) = a(T,\rho) + \frac{\beta P(T,\rho)}{\rho} \ . \tag{5.32}$$

Simulations are accelerated by a combination of high and low level optimizations. A cell-list method is used to track the position of the particles: a regular grid of cells, able to expand and shrink along with the box, is set up so that on the average a cell contains only a few particles. The distance between each pair of cells – expressed in units of the box length, in order to be unaffected by scaling operations – is precomputed at the beginning of the simulation, and a list is associated to each cell with pointers to the other cells sorted in order of increasing distance: in this way, the set of cells that are within the cutoff distance from any given cell can be identified at constant computational cost without performing any additional distance calculation. Moreover, the single-instruction, multiple-data (SIMD) extensions of Intel and AMD processors are exploited to achieve a limited amount of low-level parallelism in the computation of particle interactions.

5.4 RESULTS AND DISCUSSION

We now apply the procedure outlined in the previous section to a number of hard-core Yukawa systems. Four different systems, which we label with letters from A to D, are considered: a detailed list of the parameters defining each system can be found in Table 5.1. We always choose as the lattice structure of the solid the one stable in the absence of polydispersity, all other parameters being equal. It is indeed possible that beyond a certain degree of polydispersity another structure could be favoured, but this issue has not been addressed.

Systems A,B,C are models of micrometer-sized colloids with a surface potential in the range 25-50 mV dispersed in a low dielectric solvent at room temperature; the parameters were chosen to allow in the monodisperse limit a comparison with data available in the literature [65].

[**]If the cores do not feel each other, $N^{-1}\langle\beta U_\lambda\rangle_\lambda^{\mathrm{CM}}$ should approach 3/2 as $\lambda \to 1$.
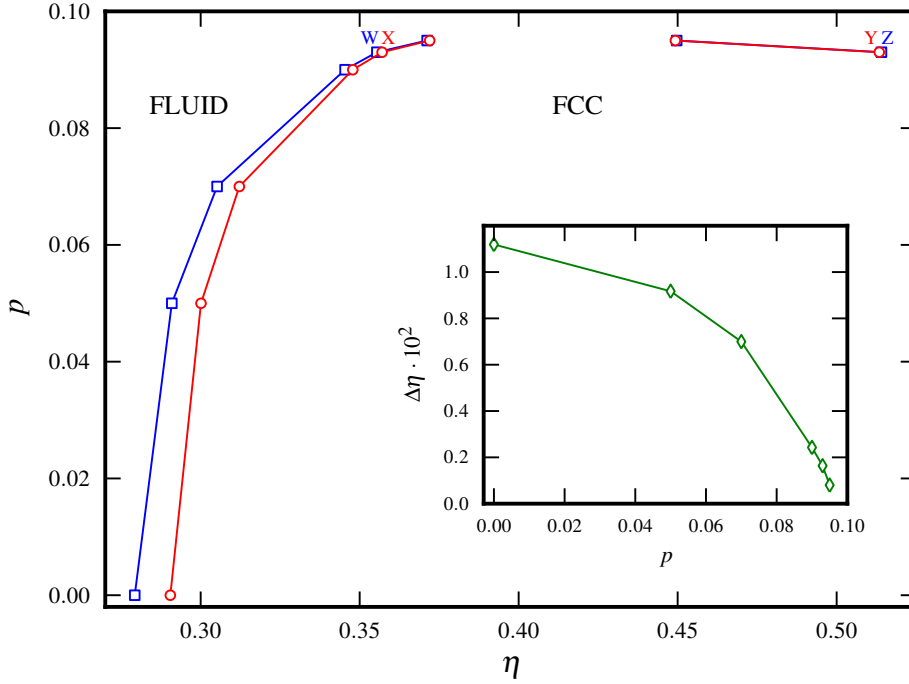
Figure 5.1: Phase diagram of hard-core Yukawa particles with $\beta\epsilon = 20$, $\kappa\bar{\sigma} = 10$ (system A) presented in the packing fraction (η), polydispersity (p) plane. Symbols denote the results from Monte Carlo simulations, whereas lines serve as guides to the eye. Reentrant melting can be seen in the upper right part of the diagram, corresponding to the two degrees of polydispersity $p = 0.093$ and $p = 0.095$. The four state points denoted by W-Z are object of structural analysis later in the text. In the inset, the difference between the packing fraction of the solid and the one of the fluid across the main (that is, non-reentrant) freezing transition is plotted as a function of the polydispersity.

System D is devised to mimic the experiments involving highly charged water-in-oil droplets reported by Leunissen at al. [80], in which a stable crystalline solid at extremely low packing fraction and high polydispersity was seen. No details are to be found in the original article, but a rough analysis of the pictures therein reveals a packing fraction in the order of 10^{-3} and a polydispersity as high as 20%. The parameters of the potential are set according to the mapping of the hard-core Yukawa model onto the point Yukawa model devised in Ref. [65] in such a way that in the absence of polydispersity the fluid-solid transition occurs at a packing fraction of the same order of the aforementioned estimate.

5.4.1 Phase diagrams

The phase behavior of system A is presented in the packing fraction, polydispersity (η, p) plane in Figure 5.1. In the absence of polydispersity the phase boundaries are fully consistent with the results of Hynninen and Dijkstra [65] (see also the column η_s^0 of Table 5.1). As the polydispersity increases, two phenomena occur: (i) the freezing
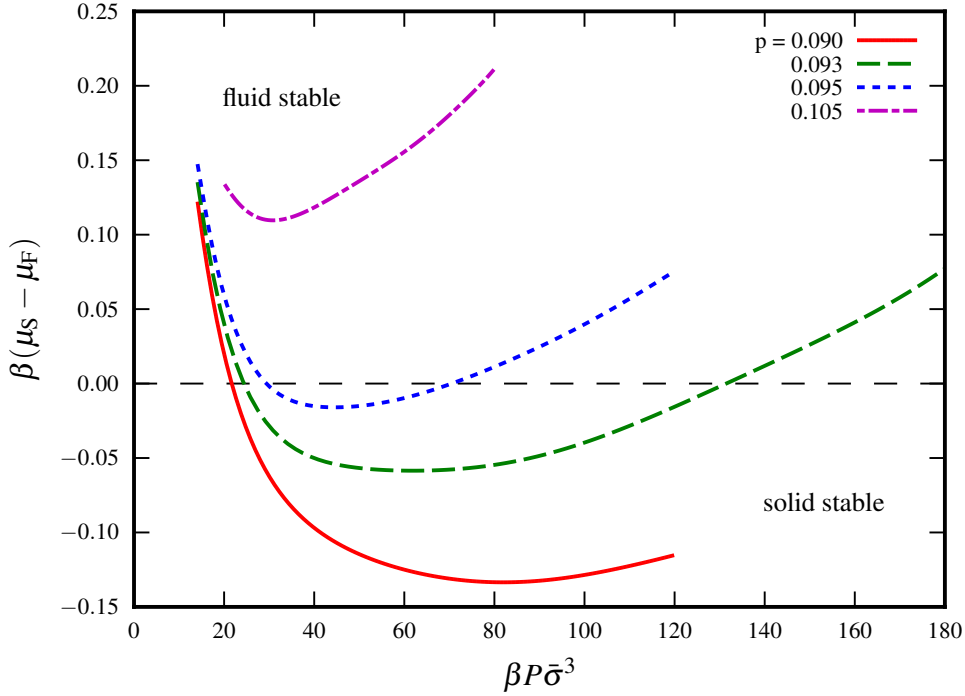
Figure 5.2: System A: difference between the chemical potential of the solid μ_S and the chemical potential of the fluid μ_F plotted as a function of the pressure for a choice of indices of polydispersity.

transition shifts towards higher packing fractions; (ii) the difference $\Delta\eta$ between the packing fraction of the solid and the packing fraction of the fluid decreases. This trend, made explicit in the inset of the figure, suggests the existence of a *terminal polydispersity* p_t corresponding to which the density gap closes ($\Delta\eta = 0$). The main diagram also shows that just below p_t reentrant melting takes place, that is the solid melts upon compression.

To gain a better understanding of these features, in Figure 5.2 the difference $\Delta\mu$ between the chemical potential of the solid and the chemical potential of the fluid is plotted as a function of the pressure for several values of the polydispersity: in such a diagram, phase coexistence corresponds to $\Delta\mu = 0$, whereas $\Delta\mu \lessgtr 0$ marks the stability of one or the other phase. For most values of the polydispersity the curve shows only one intersection with the $\Delta\mu = 0$ axis, which marks the fluid-to-ordered solid transition. From a certain degree of polydispersity on, however, a second intersection appears, and a disordered, fluid-like configuration becomes favoured again when the pressure is raised above a prescribed value. The terminal polydispersity p_t may be defined as the one corresponding to a curve tangent to the horizontal axis. Finally, when $p > p_t$ the curve lies entirely in the region of stability of the fluid and both the freezing transition and the reentrant melting transition disappear.[††]

[††]For polydispersities just below p_t, whether a second intersection is found or not is of course sensitive to the extent to which pressures are explored in the computation of the equation of state

This scenario closely matches the one first predicted by Bartlett and Warren for a hard-sphere system [13]. Although the absolute position along the vertical axis of the curves shown in Figure 5.2 depends on the exact value of the solid free energy at the reference density $\bar{\rho}_\mathrm{s}$, and is thus prone to the numerical uncertainties inherent to any thermodynamic integration, their shape is dictated by the equations of state alone, that are known with a higher degree of precision. Thus, although close to the terminal polydispersity the results might be affected by conspicuous uncertainties, we believe that the topology of the phase diagram as depicted in Figure 5.1 is sound. The precise identification of the terminal polydispersity p_t, besides being prone to errors for the aforementioned reasons, would cost a great computational effort. Nonetheless, a rough estimate is readily provided: by extrapolating the curve depicted in the inset of Figure 5.1 the terminal polydispersity can be bracketed as $0.095 < p_t < 0.100$.‡‡

We now discuss model system B, characterized by stronger and more long-ranged interparticle interactions. The phase behavior is shown in Figure 5.3 as a packing fraction-polydispersity diagram. Due to the stronger repulsion, freezing takes place at packing fractions significantly lower then the ones typical of the previous system; apart from that, the phase behavior is entirely similar. We stress two minor differences: (i) within the computational effort allocated to the project, reentrant melting could be determined only for the highest value of the polydispersity considered before the disappearance of the freezing transition (see the caption of the figure); (ii) the solid supports a higher degree of polydispersity than what seems possible in system A: indeed, the terminal polydispersity can be estimated as $0.125 < p_t < 0.130$.

Figure 5.4 reports the phase behavior of model system C, whose parameters are intermediate between those of A and B. Although the shape of the phase diagram is in line with the previous two, this time the phase boundaries could not be delineated to their full extent, nor the terminal polydispersity could be located. Indeed, beyond $p = 0.1$, that is the highest value of polydispersity reported in the plot, we could not evaluate the free energy of the solid because the procedure outlined in Section 5.3.3 failed to produce an initial crystal configuration with a density $\bar{\rho}_\mathrm{s}$ high enough for the crystal to be stable against melting. We do not know whether this failure has some relation with the approaching of the terminal polydispersity – which, judging by the curve in the inset of Figure 5.4, seems to lie not so close – or is rather a shortcoming of the employed algorithm. We lean towards the latter hypothesis, since as already noticed within the current try-and-repeat strategy the time needed to build the initial configuration grows very quickly with the size and the density of the system at high polydispersity.

Finally, Figure 5.5 shows the phase diagram of model system D, characterized by a highly repulsive long-ranged interparticle potential. The general trend uncovered in the previous systems is fully confirmed even in this extreme case. Moreover, our results confirm that an extremely dilute crystal ($\eta \approx 10^{-3}$) can sustain a polydispersity as high as 20% without melting, a fact that substantiates the findings of Leunissen et al. [80]. The terminal polydispersity is indeed quite large and can be bracketed as $0.22 < p_t < 0.23$. In the range of pressures we investigated (rather limited) no evidence was found of reentrant melting.

A comparative plot of the effects of polydispersity on the location of the fluid-solid

---

(for example, the curve corresponding to $p = 0.090$ in Figure 5.2 might cross the zero axis a second time if extended to high enough pressures). Due to constraints on simulation time, we were able to determine a reentrant behaviour only for $p = 0.093$ and $p = 0.095$; in any case, we expect the phenomenon of reentrant melting to be limited to a narrow interval below p_t.

‡‡Since no simulation was performed for $p = 0.100$, a safer upper limit, as deduced from Figure 5.2, is $p_t < 0.105$.
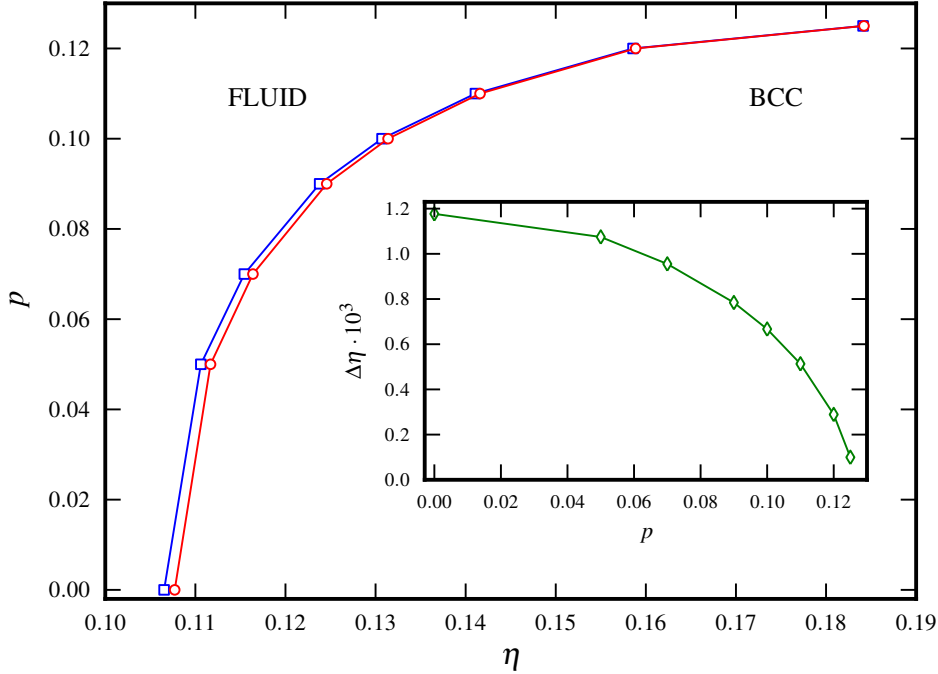
Figure 5.3: Phase diagram of hard-core Yukawa particles with $\beta\epsilon = 81$, $\kappa\bar{\sigma} = 10/3$ (system B) presented in the η, p plane. Symbols and labels are the same as in Figure 5.1. Reentrant melting at a packing fraction $\eta \approx 0.285$ (not reported in the plot for graphical convenience) was found corresponding to the highest degree of polydispersity reported ($p = 0.125$). Simulations with $p = 0.130$ were performed and showed that in that case a fluid-like, disordered state is always stable with respect to the ordered solid.

transition and on the width of the coexistence region in the four model systems is presented in Figure 5.6.

5.4.2 Microscopic structure of the polydisperse solid

A further question that can be addressed concerns the degree of microscopic order in the polydisperse solid. The solid is initially built as a perfect crystal, with FCC or BCC structure, but in the course of a simulation the particles are free to rearrange themselves. Thus, despite the fact that we always see a clear thermodynamic difference between a set of particles initially arranged as a crystalline solid and the same set initially arranged as a disordered fluid – indeed, their equations of state are clearly distinguishable, unless the solid melts – it is not guaranteed, especially at high polydispersity, that the solid retains the full initial crystalline order as the simulation proceeds. To shed some light on this issue, we consider in the phase diagram of model system A the four state points W,X,Y,Z (see Figure 5.1) and analyze the microscopic structure of the system at each point. The selected points correspond to a value of polydispersity ($p = 0.093$) close to p_t: W and X identify the fluid and the solid, respectively, coexisting across the main freezing transition, whereas Y and
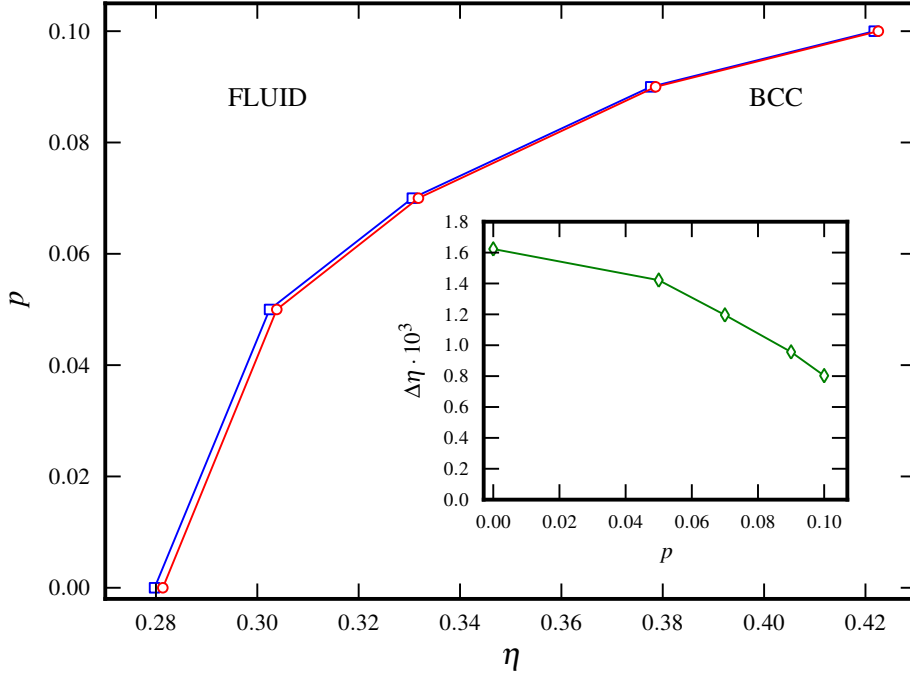
Figure 5.4: Phase diagram of hard-core Yukawa particles with $\beta\epsilon = 20$, $\kappa\bar{\sigma} = 10/3$ (system C) presented in the η, p plane. Symbols and labels are the same as in Figure 5.1. See the text for remarks on this figure.

Z correspond to the solid and the fluid, respectively, coexisting across the reentrant melting transition.

The radial distribution function corresponding to state point W, computed considering all pairs of particles irrespective of their size, is depicted in the upper panel of Figure 5.7 and shows a low degree of coordination as one expects in a fluid state. On the contrary, the radial distribution function of the solid across the phase boundary (state point X), reported in the lower panel, shows a much higher degree of coordination and the features typical of a crystalline arrangement. As a comparison, in the same plot the distribution function of a monodisperse system with the same density, whose structure is thus the one of a perfect FCC crystal, is superimposed: apart from a certain amount of smearing due to polydispersity in the former case, the two have the same structure. The radial distribution functions corresponding to state points Y and Z exhibit the same features and are not shown.

As a further inquiry on the microscopic structure of the system, we perform an analysis of the local degree of crystalline order employing the Q_6 bond order parameter [132, 6, 77]. This is one of a series of order parameters that can be used to distinguish fluid and solid domains in a system of particles, exploiting the fact that in a solid the local environments of neighboring particles are strongly correlated, whereas the same correlation is much less pronounced in a fluid sample. More precisely, we associate to each particle a set of vectors – hereafter called *bonds* – by simply draw-
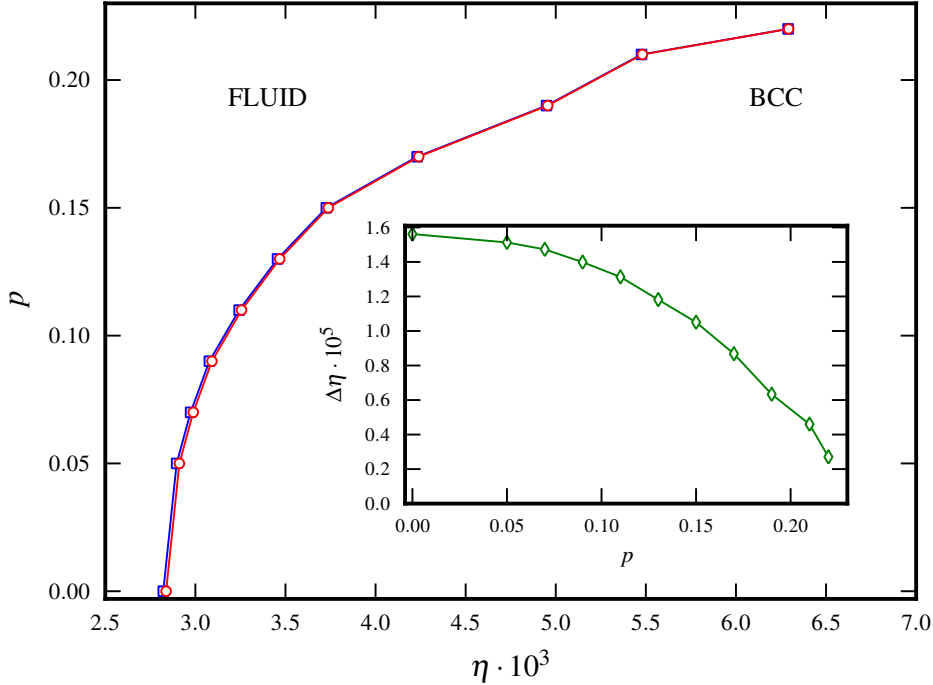
Figure 5.5: Phase diagram of hard-core Yukawa particles with $\beta\epsilon = 1200$, $\kappa\bar\sigma = 0.7$ (system D) presented in the η, p plane. Symbols and labels are the same as in Figure 5.1. Note the difference in the packing fraction scale between this figure and the previous three. The highest degree of polydispersity investigated for which fluid-solid coexistence was found is $p = 0.22$; simulations with $p = 0.23$ were performed but in that case a fluid-like, disordered state is always stable over the ordered solid.

ing lines between the particle and each of its neighbors, and look for the degree of correlation between the sets of bonds belonging to neighboring particles.

To this end, we project the local particle density around each particle in the sample onto the set of spherical harmonics $\{Y_l^m\}$: although an exact expansion would require harmonics of all orders, we make the hypothesis, to be confirmed later on, that the set of harmonics corresponding to a single, suitably chosen order l suffices for our needs. Accordingly, we associate to each particle i a set of complex numbers $\{q_{l,m}(i)\}$, with $m \in [-l, l]$, conforming to the prescription

$$q_{l,m}(i) \doteq \frac{1}{N_{\mathrm{nb}}(i)} \sum_{j=1}^{N_{\mathrm{nb}}(i)} Y_l^m(\hat{\boldsymbol{r}}_{ij}),\qquad(5.33)$$

where the sum runs over all the $N_{\mathrm{nb}}(i)$ neighbors of the particle – defined for instance as the particles lying within the first minimum in the radial distribution function – and $\hat{\boldsymbol{r}}_{ij}$ are the orientations of the bonds linking the particle with its neighbors.

The degree of correlation between the environments of two neighboring particles i and j may be quantified by the following normalized scalar product, hereafter called
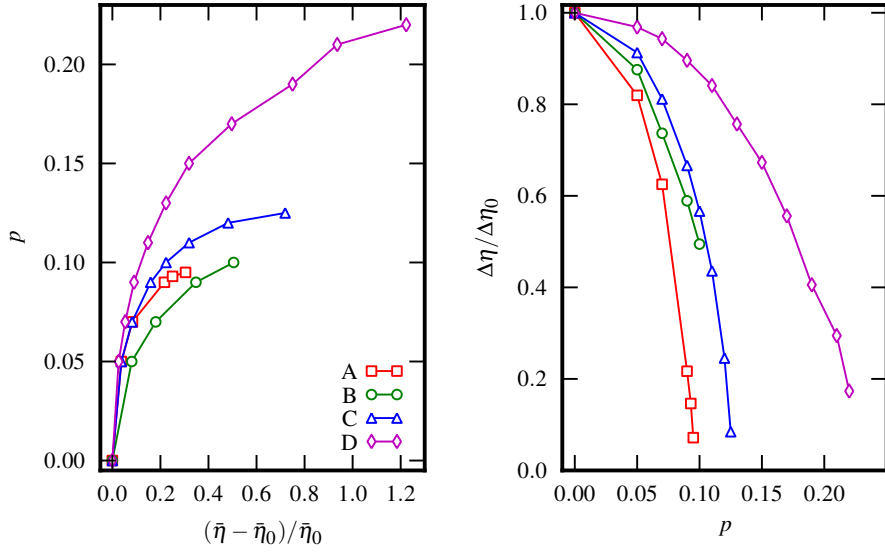
Figure 5.6: Comparative plot of the effect of polydispersity in systems A-D. Symbols are the results of Monte Carlo simulations, lines are guides to the eye. (*Left panel*) Relative shift of the fluid-solid transition as a function of the polydispersity: $\bar{\eta} = (\eta_F + \eta_S)/2$ is the mean packing fraction of the separated system, $\bar{\eta}_0$ is the value of the same quantity in the absence of polydispersity. (*Right panel*) Difference between the packing fraction of the solid and the packing fraction of the fluid ($\Delta\eta$), normalized by the value corresponding to $p = 0$ ($\Delta\eta_0$), plotted as a function of the polydispersity.

bond correlation index:

$$S_{ij} \doteq \frac{\displaystyle\sum_{m=-l}^{l} q_{l,m}(i)\, q_{l,m}^*(j)}{\left(\displaystyle\sum_{m=-l}^{l} |q_{l,m}(i)|^2\right)^{1/2} \left(\displaystyle\sum_{m=-l}^{l} |q_{l,m}(j)|^2\right)^{1/2}}, \tag{5.34}$$

where $*$ denotes complex conjugation. Note that, owing to the property $q_{l,m}^* = (-1)^m q_{l,-m}$, the latter is a real quantity.

In the upper panel of Figure 5.8 we show the histogram of the bond correlation index S_{ij} in two prototypical systems – a monodisperse fluid and a monodisperse FCC crystal – for two different choices of the order l of the harmonic base ($l \in \{4, 6\}$).[*] We notice that in either case the distribution in the fluid is much broader than the one pertaining to the crystal, which is peaked towards the upper end of the horizontal axis; moreover, the distinction is sharper when $l = 6$. One may also think to go beyond this value and consider spherical harmonics of even higher order: although this is possible, it is not advantageous, since the order parameter may become very sensitive to fluctuations in the position of the particles, leading to a broadening of the distribution. Therefore, in the following we will use $l = 6$, which enables a clear

---

[*]The histograms have been computed with reference to monodisperse realizations of model system A.
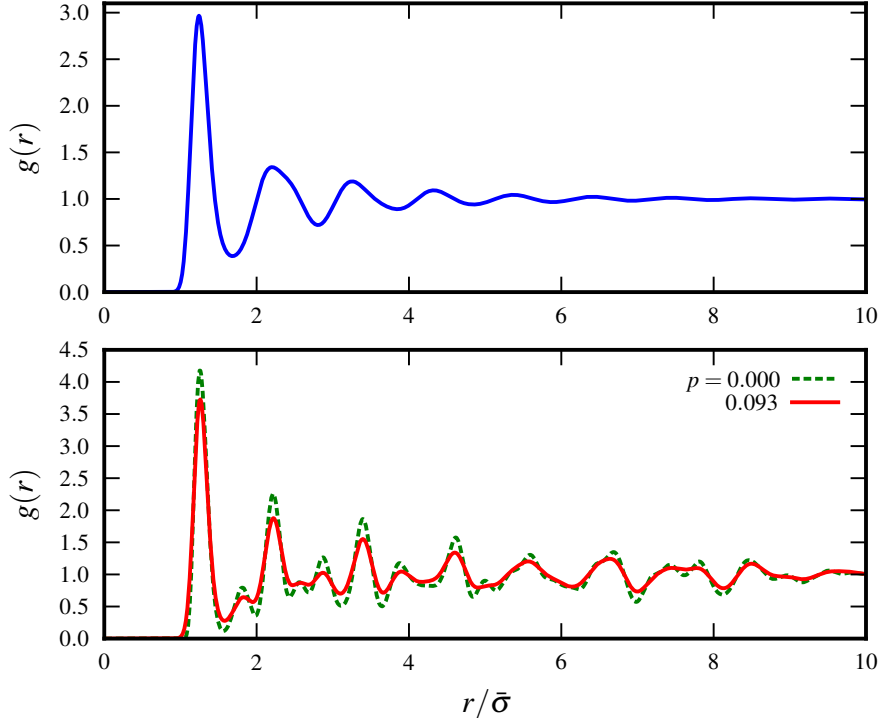
Figure 5.7: Upper panel: radial distribution function of the system at the state point W in Figure 5.1. Lower panel: radial distribution function at the state point X (full line) compared to the radial distribution function of a monodisperse system having the same density (dashed line).

distinction to be drawn between a fluid and a crystal and, at the same time, is low enough to be robust against fluctuations.

In order to identify the fluid and crystal domains in the system, we pick a threshold value $\bar{S}$ for the bond correlation index and associate to each particle i the number n_i of neighboring particles for which the bond correlation index exceeds the threshold. In other words, n_i is defined as the cardinality of the set $\{S_{ij}|S_{ij} > \bar{S}\}$, where the index j runs over the neighbors of particle i; we call this latter quantity the *number of correlated neighbors*. In the lower panel of Figure 5.8, we show the histogram of n_i for the two prototypical systems already considered, having fixed $l = 6$ and $\bar{S} = 0.5$. The distributions shown in the panel suggest that we may use the number of correlated neighbors as a practical means to distinguish fluid-like particles from solid-like particles, employing a threshold value $\bar{n}$ in the range $5 \div 8$; in the following we will take $\bar{n} = 6$.[†]

The bond order parameter just introduced allows us to estimate the crystalline fraction of the system, that is the fraction of solid-like particles over the total, even in the presence of polydispersity: in particular, we apply the procedure to the four state points W-Z in the phase diagram of model system A. The two fluid configura-

---

[†]That is, we consider a particle i solid-like if $n_i > \bar{n}$, otherwise it is classified as fluid-like.
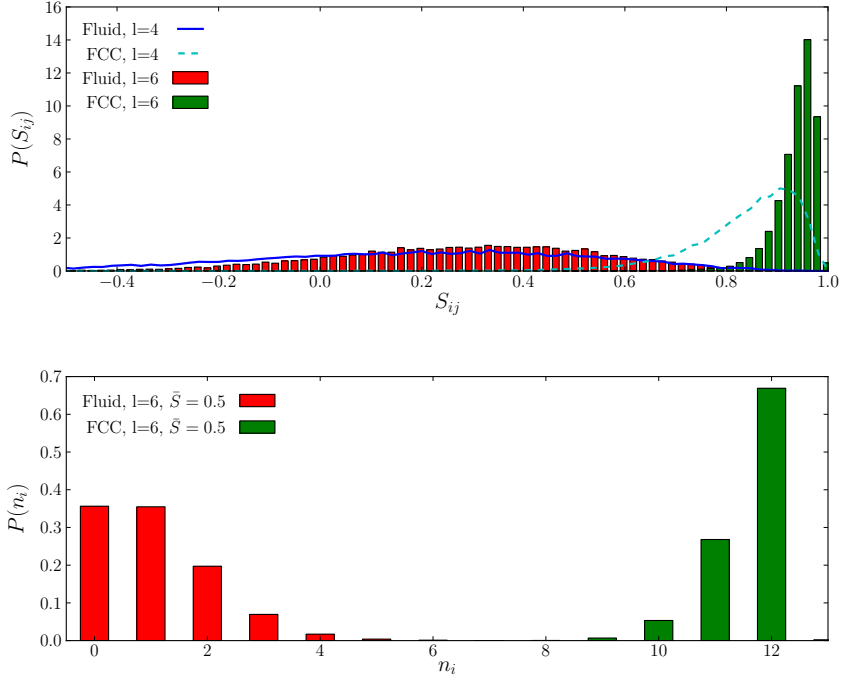
Figure 5.8: Distribution of bond order parameters in prototypical systems. Upper panel: distribution of the bond correlation index S_{ij} in a monodisperse fluid and in a monodisperse FCC crystal corresponding to a couple of different choices of the order l of the (incomplete) harmonic base. Lower panel: distribution of the number of neighbors per particle n_i with bond correlation index exceeding the threshold value $\bar{S} = 0.5$; the order of the spherical harmonics is chosen as $l = 6$.

tions (state points W and Z) are obviously characterized by a low crystalline fraction, namely 3.9% and 4.7%. Conversely, the crystalline fraction corresponding to the solid configurations (state points X and Y) is surprisingly high: 99.4% and 97.7%, respectively. This shows that the solid retains the full degree of crystalline order even close to the terminal polydispersity. Snapshots of the system with the particles coloured according to the bond order parameter are presented for state points W and X in Figures 5.9 and 5.10, respectively.

5.5   CONCLUSIONS

In this chapter we studied the effect of quenched polydispersity on the freezing transition of repulsive hard-core Yukawa fluids. A theoretical analysis showed that the conditions for polydisperse two-phase equilibrium reduce under the constraint of quenched polydispersity to the equivalent conditions for a monodisperse system. Monte Carlo simulations allowed us to map out the the phase diagram of four model systems which span a broad spectrum of interactions, from hard-sphere-like to highly repulsive. In all systems polydispersity shifts the freezing transition towards higher packing fractions and narrows the density gap between the fluid and the solid. Our results confirm
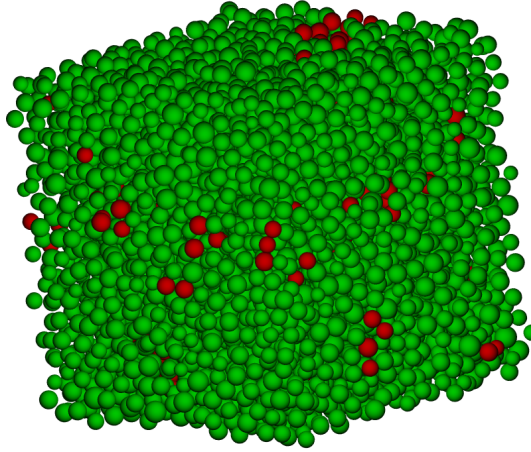
Figure 5.9: Snapshot of the system corresponding to state point W in Figure 5.1; polydispersity is $p = 0.093$. Particles are colored according to their classification based on the Q_6 bond order parameter (see the text for the details): green particles are fluid-like, red particles are solid-like. The crystalline fraction of the system is 3.9%.
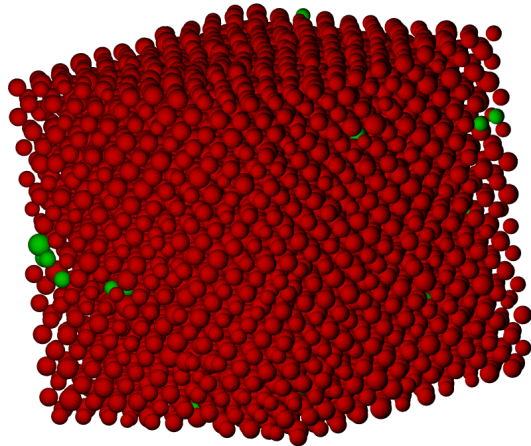

Figure 5.10: Snapshot of the system corresponding to state point X in Figure 5.1; polydispersity is $p = 0.093$. Colors have the same meaning as in Figure 5.9. The crystalline fraction equals 99.4%.

the existence of a terminal polydispersity beyond which the freezing transition disappears, so that a disordered, fluid-like configuration – which eventually may give rise to a glassy state – is stable across the whole density range. Close to the terminal polydispersity the phenomenon of reentrant melting takes place. Finally, an analysis of the microscopic structure of the system showed that across the freezing transition the polydisperse solid is fully crystalline.

We stress again that the assumption of *quenched* polydispersity is fundamental for the previous results to hold. If particle fractionation could take place, the scenario may radically change. Indeed, recent studies suggest that in this more general case no terminal polydispersity exists, since the system can always freeze by splitting off a solid with a narrow size distribution [45, 128].

References

[1] Adams, M., Dogic, Z., Keller, S. L., and Fraden, S. Entropically driven microphase transitions in mixtures of colloidal rods and spheres. *Nature 393*, 6683 (May 1998), 349–352.

[2] Alder, B. J., and Wainwright, T. E. Studies in molecular dynamics. II. behavior of a small number of elastic spheres. *The Journal of Chemical Physics 33*, 5 (1960), 1439.

[3] Archer, A. J., Pini, D., Evans, R., and Reatto, L. Model colloidal fluid with competing interactions: Bulk and interfacial properties. *The Journal of Chemical Physics 126*, 1 (2007), 014104.

[4] Arfken, G. B., and Weber, H. *Mathematical methods for physicists*. Elsevier, June 2005.

[5] Asakura, S., and Oosawa, F. On interaction between two bodies immersed in a solution of macromolecules. *The Journal of Chemical Physics 22*, 7 (1954), 1255.

[6] Auer, S., and Frenkel, D. Numerical simulation of crystal nucleation in colloids. *Advanced Computer Simulation* (2005), 149–208.

[7] Balibar, S. Physics: The force of fluctuations. *Nature 451*, 7175 (Jan. 2008), 136–137.

[8] Bancroft, W. D. *Applied colloid chemistry: general theory*. McGraw-Hill Book Company, inc., 1921.

[9] Barboy, B. On a representation of the equation of state of fluids in terms of the adhesive hard-spheres model. *The Journal of Chemical Physics 61*, 8 (1974), 3194.

[10] Barrat, J., and Hansen, J. On the stability of polydisperse colloidal crystals. *Journal de Physique 47*, 9 (1986), 7.

[11] Bartlett, P. A geometrically-based mean-field theory of polydisperse hard-sphere mixtures. *The Journal of Chemical Physics 107*, 1 (1997), 188.

[12] Bartlett, P. Fractionated crystallization in a polydisperse mixture of hard spheres. *The Journal of Chemical Physics 109*, 24 (1998), 10970.

[13] Bartlett, P., and Warren, P. B. Reentrant melting in polydispersed hard spheres. *Physical Review Letters 82*, 9 (Mar. 1999), 1979.

[14] Baxter, R. J. Percus-Yevick equation for hard spheres with surface adhesion. *The Journal of Chemical Physics 49*, 6 (1968), 2770.

[15] Bechhold, H. *Colloids in Biology and Medicine*. Read Books, Oct. 2007.

[16] Bechinger, C., Rudhardt, D., Leiderer, P., Roth, R., and Dietrich, S. Understanding depletion forces beyond entropy. *Physical Review Letters 83*, 19 (Nov. 1999), 3960.

[17] Belloni, L. Ionic condensation and charge renormalization in colloidal suspensions. *Colloids and Surfaces A: Physicochemical and Engineering Aspects 140*, 1-3 (Sept. 1998), 227–243.

[18] BELLONI, L. Colloidal interactions. *Journal of Physics Condensed Matter 12* (Nov. 2000), 549.

[19] BEVAN, D. Colloid osmotic pressure. *Anaesthesia 35*, 3 (1980), 263–270.

[20] BEYSENS, D., AND ESTEVE, D. Adsorption phenomena at the surface of silica spheres in a binary liquid mixture. *Physical Review Letters 54*, 19 (May 1985), 2123.

[21] BIBEN, T., BLADON, P., AND FRENKEL, D. Depletion effects in binary hard-sphere fluids. *Journal of Physics: Condensed Matter 8* (1996), 10799.

[22] BOLHUIS, P., HAGEN, M., AND FRENKEL, D. Isostructural solid-solid transition in crystalline systems with short-ranged interaction. *Physical Review E 50*, 6 (Dec. 1994), 4880.

[23] BOLHUIS, P. G., AND KOFKE, D. A. Monte carlo study of freezing of polydisperse hard spheres. *Physical Review E 54*, 1 (July 1996), 634.

[24] BUCCI, S., FAGOTTI, C., DEGIORGIO, V., AND PIAZZA, R. Small-angle neutron-scattering study of ionic-nonionic mixed micelles. *Langmuir 7*, 5 (May 1991), 824–826.

[25] BUZZACCARO, S., COLOMBO, J., PAROLA, A., AND PIAZZA, R. Critical depletion. *Physical Review Letters 105*, 19 (Nov. 2010), 198301.

[26] BUZZACCARO, S., PIAZZA, R., COLOMBO, J., AND PAROLA, A. Enhancement of depletion forces by electrostatic depletant repulsion. *The Journal of Chemical Physics 132*, 12 (2010), 124902.

[27] BUZZACCARO, S., RUSCONI, R., AND PIAZZA, R. "Sticky" hard spheres: Equation of state, phase diagram, and metastable gels. *Physical Review Letters 99*, 9 (2007), 098301.

[28] CALLEN, H. B. *Thermodynamics and an introduction to thermostatistics.* Wiley, Aug. 1985.

[29] CASIMIR, H. B. G. On the attraction between two perfectly conducting plates. *Konink. Nederl. Akad. Weten. 51* (1948), 793–795.

[30] CORTI, M., AND DEGIORGIO, V. Quasi-elastic light scattering study of intermicellar interactions in aqueous sodium dodecyl sulfate solutions. *The Journal of Physical Chemistry 85*, 6 (Mar. 1981), 711–717.

[31] CROCKER, J. C., MATTEO, J. A., DINSMORE, A. D., AND YODH, A. G. Entropic attraction and repulsion in binary colloids probed with a line optical tweezer. *Physical Review Letters 82*, 21 (May 1999), 4352.

[32] CURTIN, W. A., AND ASHCROFT, N. W. Weighted-density-functional theory of inhomogeneous liquids and the freezing transition. *Physical Review A 32*, 5 (Nov. 1985), 2909.

[33] DE GENNES, P. Soft matter (Nobel lecture). *Angewandte Chemie International Edition in English 31*, 7 (1992), 842–845.

[34] DEGIORGIO, V., PIAZZA, R., AND PIETRO, G. D. Depletion interaction and phase separation in mixtures of colloidal particles and nonionic micelles. *Trends in Colloid and Interface Science X* (1996), 201–205.

[35] DERJAGUIN, B. V. Friction and adhesion. IV. the theory of adhesion of small particles. *Kolloid Zeits 69* (1934), 155–164.

[36] DICKMAN, R., ATTARD, P., AND SIMONIAN, V. Entropic forces in binary hard sphere mixtures: Theory and simulation. *The Journal of Chemical Physics 107*, 1 (1997), 205.

[37] DIJKSTRA, M., VAN ROIJ, R., AND EVANS, R. Phase behavior and structure of binary Hard-Sphere mixtures. *Physical Review Letters 81*, 11 (1998), 2268.

[38] DIJKSTRA, M., VAN ROIJ, R., AND EVANS, R. Phase diagram of highly asymmetric binary hard-sphere mixtures. *Physical Review E 59*, 5 (May 1999), 5744.

[39] DIJKSTRA, M., VAN ROIJ, R., AND EVANS, R. Effective interactions, structure, and isothermal compressibility of colloidal suspensions. *The Journal of Chemical Physics 113*, 11 (2000), 4799.

[40] DURBIN, S. D., AND FEHER, G. Protein crystallization. *Annual Review of Physical Chemistry 47*, 1 (1996), 171–204.

[41] EGOROV, S. A. Effect of repulsive and attractive interactions on depletion forces in colloidal suspensions: A density functional theory treatment. *Physical Review E 70*, 3 (2004), 031402.

[42] EVANS, D. F., AND WENNERSTROM, H. *The Colloidal Domain: Where Physics, Chemistry, Biology, and Technology Meet*, 2 ed. Wiley-VCH, Feb. 1999.

[43] EVANS, I. D., AND HAISMAN, D. R. Rheology of gelatinised starch suspensions. *Journal of Texture Studies 10*, 4 (1980), 347–370.

[44] FASOLO, M., AND SOLLICH, P. Equilibrium phase behavior of polydisperse hard spheres. *Physical Review Letters 91*, 6 (2003), 068301.

[45] FASOLO, M., AND SOLLICH, P. Fractionation effects in phase equilibria of polydisperse hard-sphere colloids. *Physical Review E 70*, 4 (Oct. 2004), 041410.

[46] FISHER, M. E. Correlation functions and the critical region of simple fluids. *Journal of Mathematical Physics 5*, 7 (1964), 944.

[47] FISHER, M. E., AND GENNES, P. G. D. Wall phenomena in a critical binary mixture. *CR Seances Acad. Sci., Ser. B 287*, 8 (1978), 207–209.

[48] FRENKEL, D., AND LADD, A. J. C. New monte carlo method to compute the free energy of arbitrary solids. application to the fcc and hcp phases of hard spheres. *The Journal of Chemical Physics 81*, 7 (1984), 3188.

[49] GALLAGHER, P. D., KURNAZ, M. L., AND MAHER, J. V. Aggregation in polystyrene-sphere suspensions in near-critical binary liquid mixtures. *Physical Review A 46*, 12 (Dec. 1992), 7750.

[50] GALLAGHER, P. D., AND MAHER, J. V. Partitioning of polystyrene latex spheres in immiscible critical liquid mixtures. *Physical Review A 46*, 4 (1992), 2012.

[51] GAZZILLO, D., AND GIACOMETTI, A. Analytic solutions for baxter's model of sticky hard sphere fluids within closures different from the Percus-Yevick approximation. *The Journal of Chemical Physics 120*, 10 (2004), 4742.

[52] GOTZELMANN, B., ROTH, R., DIETRICH, S., DIJKSTRA, M., AND EVANS, R. Depletion potential in hard-sphere fluids. *EPL (Europhysics Letters) 47* (1999), 398.

[53] GRAHAM, T. Liquid diffusion applied to analysis. *Philosophical Transactions of the Royal Society of London 151* (1861), 183–224.

[54] GRULL, H., AND WOERMANN, D. Stability of colloidal suspensions in a binary liquid mixture in the vicinity of its binodal curve. *Berichte der Bunsen-Gesellschaft 101*, 5 (1997).

[55] HACHISU, S. Phase transition in monodisperse gold sol. microscopic observation of gas, liquid and solid states. *Croatica Chemica Acta 71* (1998), 975.

[56] HAGEN, M. H. J., AND FRENKEL, D. Determination of phase diagrams for the hard-core attractive yukawa system. *The Journal of Chemical Physics 101*, 5 (1994), 4093.

[57] HANSEN, J. P., AND MCDONALD, I. R. *Theory of simple liquids.* Academic Press, 2006.

[58] HAW, M. D. Colloidal suspensions, brownian motion, molecular reality: a short history. *Journal of Physics: Condensed Matter 14*, 33 (2002), 7769–7779.

[59] HERTLEIN, C., HELDEN, L., GAMBASSI, A., DIETRICH, S., AND BECHINGER, C. Direct measurement of critical casimir forces. *Nature 451*, 7175 (Jan. 2008), 172–175.

[60] HILL, T. L. *Statistical mechanics: principles and selected applications.* Courier Dover Publications, 1987.

[61] HOGG, R., HEALY, T. W., AND FUERSTENAU, D. W. Mutual coagulation of colloidal dispersions. *Transactions of the Faraday Society 62* (1966), 1638–1651.

[62] HOOVER, W. G. Melting transition and communal entropy for hard spheres. *The Journal of Chemical Physics 49*, 8 (1968), 3609.

[63] HOYE, J. S., PINI, D., AND STELL, G. SCOZA critical exponents and scaling in three dimensions. *Physica A: Statistical Mechanics and its Applications 279*, 1-4 (May 2000), 213–223.

[64] HUNTER, R. J. *Foundations of colloid science.* Oxford University Press, 2001.

[65] HYNNINEN, A., AND DIJKSTRA, M. Phase diagrams of hard-core repulsive yukawa particles. *Physical Review E 68*, 2 (2003), 021407.

[66] ILETT, S. M., ORROCK, A., POON, W. C. K., AND PUSEY, P. N. Phase behavior of a model colloid-polymer mixture. *Physical Review E 51*, 2 (Feb. 1995), 1344.

[67] JANA, N. R. Shape effect in nanoparticle Self-Assembly. *Angewandte Chemie 116*, 12 (2004), 1562–1566.

[68] JAYALAKSHMI, Y., AND KALER, E. W. Phase behavior of colloids in binary liquid mixtures. *Physical Review Letters 78*, 7 (Feb. 1997), 1379.

[69] KARANIKAS, S., AND LOUIS, A. A. Dynamic colloidal stabilization by nanoparticle halos. *Physical Review Letters 93*, 24 (Dec. 2004), 248303.

[70] KAWAI, T., AND TAKEI, Y. *Algebraic analysis of singular perturbation theory.* AMS Bookstore, 2005.

[71] KOFKE, D. A., AND BOLHUIS, P. G. Freezing of polydisperse hard spheres. *Physical Review E 59*, 1 (Jan. 1999), 618.

[72] KRANENDONK, W. G. T., AND FRENKEL, D. Simulation of the adhesive-hard-sphere model. *Molecular Physics: An International Journal at the Interface Between Chemistry and Physics 64*, 3 (1988), 403.

[73] KRAUSE, P. F., AND FLOOD, K. L. Weather and climate extremes. Tech. rep., Sept. 1997.

[74] KRECH, M. *The Casimir effect in critical systems.* World Scientific, June 1994.

[75] KRECH, M., AND DIETRICH, S. Finite-size scaling for critical films. *Physical Review Letters 66*, 3 (Jan. 1991), 345.

[76] KROGH, A., LANDIS, E. M., AND TURNER, A. H. The movement of fluid through the human capillary wall in relation to venous pressure and to the colloid osmotic pressure of the blood. *Journal of Clinical Investigation 11*, 1 (Jan. 1932), 63–95.

[77] LECHNER, W., AND DELLAGO, C. Accurate determination of crystal structures based on averaged local bond order parameters. *The Journal of Chemical Physics 129*, 11 (2008), 114707.

[78] LEE, C. L., STELL, G., AND HOYE, J. S. A simple SCOZA for simple fluids. *Journal of Molecular Liquids 112*, 1-2 (June 2004), 13–19.

[79] LEKKERKERKER, H. N. W., POON, W. C., PUSEY, P. N., STROOBANTS, A., AND WARREN, P. B. Phase behaviour of colloid + polymer mixtures. *Europhysics Letters (EPL) 20*, 6 (1992), 559–564.

[80] LEUNISSEN, M. E., VAN BLAADEREN, A., HOLLINGSWORTH, A. D., SULLIVAN, M. T., AND CHAIKIN, P. M. Electrostatics at the oil-water interface, stability, and order in emulsions and colloids. *Proceedings of the National Academy of Sciences 104*, 8 (Feb. 2007), 2585 –2590.

[81] LIKOS, C. N. Effective interactions in soft condensed matter physics. *Physics Reports 348* (July 2001), 267–439.

[82] LIU, J., AND LUIJTEN, E. Stabilization of colloidal suspensions by means of highly charged nanoparticles. *Physical Review Letters 93*, 24 (Dec. 2004), 247802.

[83] LOUIS, A. A. Effective potentials for polymers and colloids: beyond the van der waals picture of fluids? *Philosophical Transactions of the Royal Society of London. Series A: Mathematical, Physical and Engineering Sciences 359*, 1782 (May 2001), 939 –960.

[84] LOUIS, A. A., ALLAHYAROV, E., LOWEN, H., AND ROTH, R. Effective forces in colloidal mixtures: From depletion attraction to accumulation repulsion. *Physical Review E 65*, 6 (June 2002), 061407.

[85] Lu, P. J., Conrad, J. C., Wyss, H. M., Schofield, A. B., and Weitz, D. A. Fluids of clusters in attractive colloids. *Physical Review Letters 96*, 2 (Jan. 2006), 028306.

[86] Lu, P. J., Zaccarelli, E., Ciulla, F., Schofield, A. B., Sciortino, F., and Weitz, D. A. Gelation of particles with short-range attraction. *Nature 453*, 7194 (May 2008), 499–503.

[87] Malijevsky, A., Yuste, S. B., and Santos, A. How sticky are short-range square-well fluids? *The Journal of Chemical Physics 125*, 7 (2006), 074507.

[88] Mao, Y., Cates, M. E., and Lekkerkerker, H. N. W. Depletion force in colloidal systems. *Physica A: Statistical and Theoretical Physics 222*, 1-4 (Dec. 1995), 10–24.

[89] Marenduzzo, D., Finan, K., and Cook, P. R. The depletion attraction: an underappreciated force driving cellular organization. *The Journal of cell biology 175*, 5 (2006), 681.

[90] McRae, R., and Haymet, A. D. J. Freezing of polydisperse hard spheres. *The Journal of Chemical Physics 88*, 2 (1988), 1114.

[91] Miller, M. A., and Frenkel, D. Phase diagram of the adhesive hard sphere fluid. *The Journal of Chemical Physics 121*, 1 (2004), 535.

[92] Narayanan, T., Kumar, A., Gopal, E. S. R., Beysens, D., Guenoun, P., and Zalczer, G. Reversible flocculation of silica colloids in liquid mixtures. *Physical Review E 48*, 3 (1993), 1989.

[93] Nelson, E., and Brown, R. Dynamical theories of brownian motion - second edition. *Sinauer Associates Inc* (1998).

[94] Ng, K. *The Journal of Chemical Physics 61*, 7 (1974), 2680.

[95] Noro, M. G., and Frenkel, D. Extended corresponding-states behavior for particles with variable range attractions. *The Journal of Chemical Physics 113*, 8 (2000), 2941.

[96] Ohshima, H. *Theory of colloid and interfacial electric phenomena*. Academic Press, 2006.

[97] Ohshima, H. *Biophysical Chemistry of Biointerfaces*. Wiley-Interscience, 2010.

[98] Orea, P., Tapia-Medina, C., Pini, D., and Reiner, A. Thermodynamic properties of short-range attractive yukawa fluid: Simulation and theory. *The Journal of Chemical Physics 132*, 11 (2010), 114108.

[99] Ornstein, L. S., and Zernike, F. Integral equation in liquid state theory. In *Proc. Sect. Sci. K. Ned. Akad. Wet* (1914), vol. 17, p. 793.

[100] Oversteegen, S. M., and Lekkerkerker, H. N. W. On the accuracy of the derjaguin approximation for depletion potentials. *Physica A: Statistical Mechanics and its Applications 341* (Oct. 2004), 23–39.

[101] Patterson, T. N. L. The optimum addition of points to quadrature formulae. *Mathematics of Computation 22*, 104 (Oct. 1968), 847–856.

[102] PELISSETTO, A., AND VICARI, E. Critical phenomena and renormalization-group theory. *Physics Reports 368* (Oct. 2002), 549–727.

[103] PERCUS, J. Proceedings of the Symposium on the Many-Body Problem, held at Stevens Institute of Technology, Hoboken, New Jersey, January 28-29 1957. New York, Interscience Publishers (1963).

[104] PHAN, S., RUSSEL, W. B., ZHU, J., AND CHAIKIN, P. M. Effects of poly-dispersity on hard sphere crystals. *The Journal of Chemical Physics 108*, 23 (1998), 9789.

[105] PIAZZA, R., STAVANS, J., BELLINI, T., LENTI, D., VISCA, M., AND DEGIOR-GIO, V. Light-scattering experiment on anisotropic spherical particles. *Trends in Colloid and Interface Science IV* (1990), 89–94.

[106] PIESSENS, R. *Quadpack: a subroutine package for automatic integration.* Springer-Verlag, 1983.

[107] PINI, D., STELL, G., AND DICKMAN, R. Thermodynamically self-consistent theory of structure for three-dimensional lattice gases. *Physical Review E 57*, 3 (Mar. 1998), 2862.

[108] POLSON, J. M., TRIZAC, E., PRONK, S., AND FRENKEL, D. Finite-size corrections to the free energies of crystalline solids. *The Journal of Chemical Physics 112*, 12 (2000), 5339.

[109] PRASAD, V., SEMWOGERERE, D., AND WEEKS, E. R. Confocal microscopy of colloids. *Journal of Physics: Condensed Matter 19*, 11 (2007), 113102.

[110] PUSEY, P. N. Liquids, freezing and glass transition. *ed J-P Hansen, D Levesque and J Zinn-Justin (Amsterdam: North-Holland)* (1991).

[111] PUSEY, P. N., AND VAN MEGEN, W. Phase behaviour of concentrated suspensions of nearly hard colloidal spheres. *Nature 320*, 6060 (Mar. 1986), 340–342.

[112] PUSEY, P. N., AND VAN MEGEN, W. Observation of a glass transition in suspensions of spherical colloidal particles. *Physical Review Letters 59*, 18 (Nov. 1987), 2083.

[113] PUSEY, P. N., ZACCARELLI, E., VALERIANI, C., SANZ, E., POON, W. C. K., AND CATES, M. E. Hard spheres: crystallization and glass formation. *Philosophical Transactions of the Royal Society A: Mathematical, Physical and Engineering Sciences 367*, 1909 (Dec. 2009), 4993–5011.

[114] REGNAUT, C., AND RAVEY, J. C. Application of the adhesive sphere model to the structure of colloidal suspensions. *The Journal of Chemical Physics 91*, 2 (1989), 1211.

[115] REINER, A., AND HOYE, J. S. Self-consistent Ornstein-Zernike approximation for the yukawa fluid with improved direct correlation function. *The Journal of Chemical Physics 128*, 11 (2008), 114507.

[116] ROSENBAUM, D., AND ZUKOSKI, C. Protein interactions and crystallization. *Journal of Crystal Growth 169*, 4 (Dec. 1996), 752–758.

[117] ROTH, R., EVANS, R., AND DIETRICH, S. Depletion potential in hard-sphere mixtures: Theory and applications. *Physical Review E 62*, 4 (Oct. 2000), 5360.

[118] ROYALL, C. P., LEUNISSEN, M. E., HYNNINEN, A., DIJKSTRA, M., AND VAN BLAADEREN, A. Re-entrant melting and freezing in a model system of charged colloids. *The Journal of Chemical Physics 124*, 24 (2006), 244706.

[119] RUDHARDT, D., BECHINGER, C., AND LEIDERER, P. Direct measurement of depletion potentials in mixtures of colloids and nonionic polymers. *Physical Review Letters 81*, 6 (1998), 1330.

[120] SALACUSE, J. J. Polydisperse systems: Statistical thermodynamics, with applications to several models including hard and permeable spheres. *The Journal of Chemical Physics 77*, 7 (1982), 3714.

[121] SCHMIDT, M., LWEN, H., BRADER, J. M., AND EVANS, R. Density functional theory for a model colloid polymer mixture: bulk fluid phases. *Journal of Physics: Condensed Matter 14*, 40 (2002), 9353–9382.

[122] SCHOFIELD, P., AND HENDERSON, J. R. Statistical mechanics of inhomogeneous fluids. *Proceedings of the Royal Society of London. Series A, Mathematical and Physical Sciences 379*, 1776 (Jan. 1982), 231–246.

[123] SCHOLL-PASCHINGER, E., BENAVIDES, A. L., AND CASTANEDA-PRIEGO, R. Vapor-liquid equilibrium and critical behavior of the square-well fluid of variable range: A theoretical study. *The Journal of Chemical Physics 123*, 23 (2005), 234513.

[124] SCIORTINO, F., MOSSA, S., ZACCARELLI, E., AND TARTAGLIA, P. Equilibrium cluster phases and Low-Density arrested disordered states: The role of Short-Range attraction and Long-Range repulsion. *Physical Review Letters 93*, 5 (July 2004), 055701.

[125] SEAR, R. P. Phase separation and crystallisation of polydisperse hard spheres. *Europhysics Letters (EPL) 44*, 4 (1998), 531–535.

[126] SEATON, N. A., AND GLANDT, E. D. Monte carlo simulation of adhesive spheres. *The Journal of Chemical Physics 87*, 3 (1987), 1785.

[127] SOLLICH, P. Predicting phase equilibria in polydisperse systems. *Journal of Physics: Condensed Matter 14* (2002), R79.

[128] SOLLICH, P., AND WILDING, N. B. Crystalline phases of polydisperse spheres. *Physical Review Letters 104*, 11 (Mar. 2010), 118302.

[129] SOMASUNDARAN, P. *Encyclopedia of surface and colloid science.* Taylor & Francis, 2006.

[130] SOYKA, F., ZVYAGOLSKAYA, O., HERTLEIN, C., HELDEN, L., AND BECHINGER, C. Critical casimir forces in colloidal suspensions on chemically patterned surfaces. *Physical Review Letters 101*, 20 (Nov. 2008), 208301.

[131] STANLEY, H. E. *Introduction to Phase Transitions and Critical Phenomena.* July 1987.

[132] STEINHARDT, P. J., NELSON, D. R., AND RONCHETTI, M. Bond-orientational order in liquids and glasses. *Physical Review B 28*, 2 (July 1983), 784.

[133] STELL, G. Sticky spheres and related systems. *Journal of Statistical Physics 63*, 5-6 (1991), 1203–1221.

[134] STROOBANTS, A. Columnar versus smectic order in binary mixtures of hard parallel spherocylinders. *Physical Review Letters 69*, 16 (Oct. 1992), 2388.

[135] SUBRAMANIA, G., CONSTANT, K., BISWAS, R., SIGALAS, M. M., AND HO, K. Optical photonic crystals fabricated from colloidal systems. *Applied Physics Letters 74*, 26 (1999), 3933.

[136] THEVENOT, C., GRASSL, B., BASTIAT, G., AND BINANA, W. Aggregation number and critical micellar concentration of surfactant determined by time-dependent static light scattering (TDSLS) and conductivity. *Colloids and Surfaces A: Physicochemical and Engineering Aspects 252*, 2-3 (Jan. 2005), 105–111.

[137] TOHVER, V., CHAN, A., SAKURADA, O., AND LEWIS, J. A. Nanoparticle engineering of complex fluid behavior. *Langmuir 17*, 26 (Dec. 2001), 8414–8421.

[138] TOHVER, V., SMAY, J. E., BRAEM, A., BRAUN, P. V., AND LEWIS, J. A. Nanoparticle halos: A new colloid stabilization mechanism. *Proceedings of the National Academy of Sciences of the United States of America 98*, 16 (July 2001), 8950–8954.

[139] VASILYEV, O., GAMBASSI, A., MACIOLEK, A., AND DIETRICH, S. Monte carlo simulation results for critical casimir forces. *Europhysics Letters (EPL) 80*, 6 (2007), 60009.

[140] VASILYEV, O., GAMBASSI, A., MACIOLEK, A., AND DIETRICH, S. Universal scaling functions of critical casimir forces obtained by monte carlo simulations. *Physical Review E 79*, 4 (Apr. 2009), 041142.

[141] VLASOV, Y. A., BO, X., STURM, J. C., AND NORRIS, D. J. On-chip natural assembly of silicon photonic bandgap crystals. *Nature 414*, 6861 (Nov. 2001), 289–293.

[142] WANG, J., AND ANISIMOV, M. A. Nature of vapor-liquid asymmetry in fluid criticality. *Physical Review E 75*, 5 (May 2007), 051107.

[143] WATTS, R. O., HENDERSON, D., AND BAXTER, R. J. Hard spheres with surface adhesion: the Percus-Yevick approximation and the energy equation. *Adv. Chem. Phys 21* (1971), 421–430.

[144] WILDING, N. B. Solid-liquid coexistence of polydisperse fluids via simulation. *The Journal of Chemical Physics 130*, 10 (2009), 104103.

[145] WILDING, N. B., SOLLICH, P., FASOLO, M., AND BUZZACCHI, M. Phase behavior and particle size cutoff effects in polydisperse fluids. *The Journal of Chemical Physics 125*, 1 (2006), 014908.

[146] WOOD, W. W., AND JACOBSON, J. D. Preliminary results from a recalculation of the monte carlo equation of state of hard spheres. *The Journal of Chemical Physics 27*, 5 (1957), 1207.

Summary

In this thesis I have dealt with a number of selected questions concerning the equilibrium properties and the phase behavior of colloidal suspensions, using both theory – including analytical and numerical methods from the physics of the liquid state – and computer simulation. This is the work of a theoretical physicist, thereby several low-level details have been forgotten in favor of general and (whenever possible) simple models. As a consequence, an emphasis has been placed on the notion of effective interaction, which permeates and underlies most of the work reported herein.

In the introduction I presented the reader with an overview of colloidal suspensions, motivating the broad interest they have attracted in the last few decades both as a valuable test bench for ideas in condensed matter physics and as building blocks for novel materials. The three classes of effective interactions that would form the basis for the subsequent discussion – namely the depletion, screened Coulomb and critical Casimir interaction – were also introduced.

In Chapter 2 I proposed an approximate method to obtain the equilibrium properties of a system of hard spheres with surface adhesion, seeking an improvement upon the well known Percus-Yevick solution. Assuming the direct correlation function to vanish beyond the range of the potential, in the sticky limit the thermodynamics of the system are seen to depend on a single scalar parameter varying with the density and the effective temperature. In order for thermodynamic consistency to be ensured, this parameter must satisfy a certain nonlinear differential equation, that I derived and attempted to solve numerically. A pronounced sensitivity to the boundary conditions suggests that the self-consistent approach is inadequate for sticky interparticle potentials.

In Chapter 3 I studied how the depletion force induced on spherical colloids by a fluid of smaller particles departs from the paradigmatic Asakura-Oosawa model when electric charges are present both on the colloids and the depletant particles. Upon modeling the system as a binary mixture with screened-Coulomb repulsive interparticle interactions, I applied the hypernetted-chain integral equation to derive the effective pair potential characterizing an equivalent one-component system containing the colloids alone. The Coulomb repulsion triggers two distinct effects, namely an increase in the osmotic pressure of the depletant and a condensation of the depletant particles near the surface of the colloids, which contribute in contrasting ways to the effective potential. By postulating a high structural charge on the colloids, an enhancement of the depletion force was predicted. A consistent semi-quantitative interpretation of experimental data corroborates the analysis.

In Chapter 4 I developed a theoretical framework aiming to describe on a common basis the depletion interaction and the critical Casimir effect. Using the methods of density functional theory I derived a formally exact expression for the energy of interaction of two parallel walls immersed in a fluid with arbitrary interparticle interactions. The result holds even in the neighbourhood of a critical point of the fluid, where the latter is strongly correlated. The density functional approach is known to give accurate results when applied to the class depletion interactions: by performing a long-wavelength analysis of the density fluctuations and using a scaling form of the free energy of the fluid in the critical region, I showed that it also accounts quantitatively for the scaling behavior of the critical Casimir force that is usually derived along the critical isochore by means of field-theoretical methods. As a bonus, the scaling behavior off the critical isochore could be computed as well. The main result is that depletion-induced and critical-Casimir forces have a common origin and merge continuously as the thermodynamic state of the host fluid is varied. Experimental

evidence supports this finding.

Finally, in Chapter 5 using Monte Carlo simulations I studied the effect of size polydispersity on the freezing transition of charged colloidal suspensions. The goal was to ascertain whether, and how, a sufficient amount of polydispersity suppresses the crystalline phase in favor of an amorphous solid. The particle surface potential was taken as a constant, so that size polydispersity entailed charge polydispersity; moreover, the particle size distribution was the same in the fluid and the crystal, that is particle fractionation was *not* allowed. I performed several free energy calculations, investigating different combinations of screening length and surface potential. A consistent pattern emerged: upon increasing the polydispersity, the freezing transition shifts towards higher packing fractions and the density gap between the fluid and the solid diminishes. The results support the existence of a terminal polydispersity above which the freezing transition disappears, and also confirm the phenomenon of reentrant melting.

Acknowledgements

My biggest Thank You! goes to Alberto, for his constant and patient guidance in the last three years. You have been not only a good supervisor, but also – and most importantly – the kindest person with whom I could hope to work.

I sincerely acknowledge Roberto and Stefano for their scientific exuberance (!) and for being a constant source of stimulating questions and discussions.

Many thanks to Valeria who shared the office with me and was a real friend. As many thanks go to all my other friends at Insubria, without whom these years would have been far less enjoyable: although in the near future we will probably be scattered all around Europe, I do hope – and firmly believe – that we will reunite every now and then. And of course I thank my dearest friends outside Insubria, simply for being there, always.

I am also sincerely grateful to Marjolein Dijkstra for the period I spent in Utrecht, and to all the good people I met there: you really made me feel like I was home.

In the very end, since they deserve a special mention, I would like to thank my family and Gabriella.

Grazie a tutti!

List of Publications

This thesis is based on the following publications:

1. Stefano Buzzaccaro, Roberto Piazza, Jader Colombo, and Alberto Parola, *Enhancement of depletion forces by electrostatic depletant repulsion*. The Journal of Chemical Physics **132**,124902 (2010).

2. Stefano Buzzaccaro, Roberto Piazza, Jader Colombo, and Alberto Parola, *Critical depletion*. Physical Review Letters **105**, 198301 (2010).

3. Stefano Buzzaccaro, Roberto Piazza, Jader Colombo, and Alberto Parola, *When Depletion Goes Critical*. Accepted for publication in Journal of Physics: Condensed Matter.

4. Davide Pini, Alberto Parola, Jader Colombo, and Luciano Reatto, *An investigation of the SCOZA for narrow and sticky square-well potentials*. Accepted for publication in Molecular Physics.

5. Jader Colombo and Marjolein Dijkstra, *Effect of quenched size polydispersity on the fluid-solid transition in charged colloidal suspensions*. In preparation.